Georgia Tech Research Institute

Final Report
GTRI Report A6221/2001-1

Distributed Exhaust Nozzles for Jet Noise Reduction

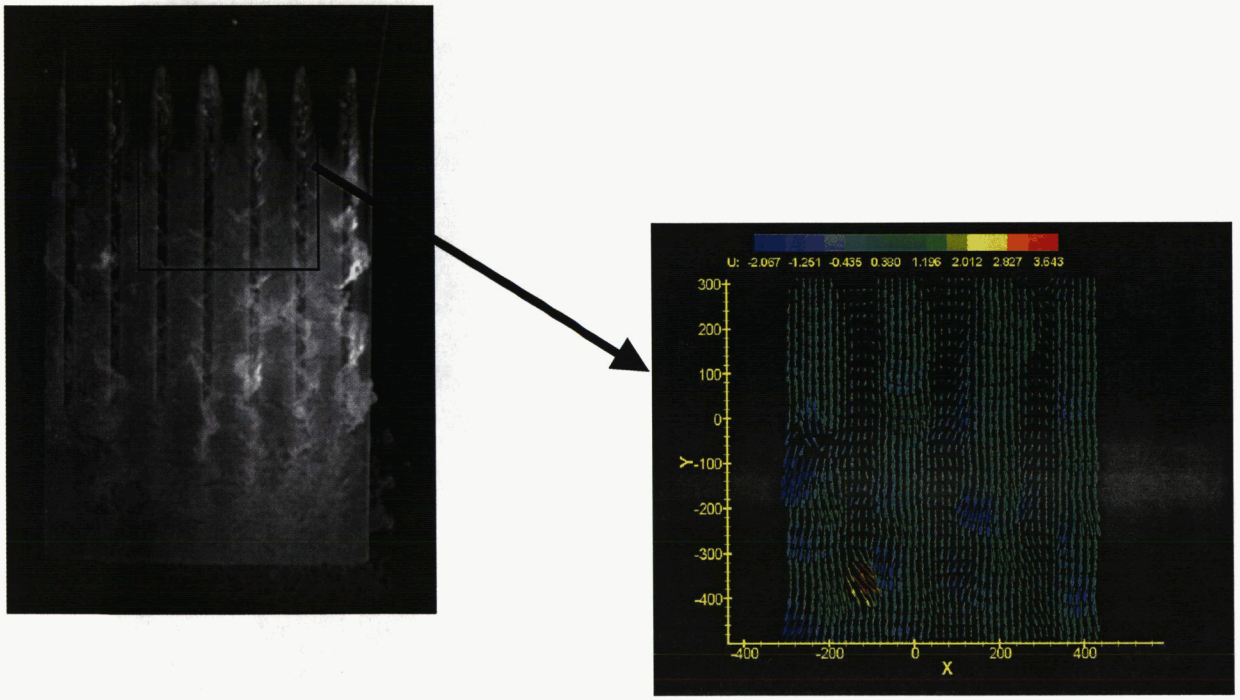

K. K. Ahuja, R. J. Gaeta, and B. Hellman
Georgia Institute of Technology, GTRI/ATASL
Aerospace and Acoustics Technologies Branch
Atlanta, Georgia 30332-0844

D. B. Schein and W. D. Solomon, Jr.
Northrop-Grumman Corporation
Integrated Systems Sector, Air Combat Systems
El Segundo, CA 90245-2904

Prepared for:
NASA Glenn Research Center
Under Grant NAG3-2352

31 DEC 2001

Foreword/Acknowledgements

This work was funded by NASA Glenn Research Center under the Grant number NAG3-2352. The NASA Technical monitor was Dr. Dennis Huff and the Georgia Tech program manager was Dr. Krish Ahuja. This work required a careful design of the distributed exhaust nozzle. The design was carried out by Mr. W. David Solomon, Jr. and Dr. David Schein of Northrop-Grumman under a subcontract. All of the experiments reported here were carried out by Dr. Richard Gaeta of the Georgia Tech Research Institute who was assisted by an undergraduate student, Barry Hellman. The authors are grateful to NASA Glenn Research Center for supporting this investigation.

Executive Summary

This report describes the work performed by the Georgia Tech Research Institute (GTRI) under NASA Glenn Research Center Grant NAG3-2352. The main objective of this study is to validate the jet noise reduction potential of a concept associated with distributed exhaust nozzles. Under this concept the propulsive thrust is generated by a larger number of discrete plumes issuing from an array of small or mini-nozzles. The potential of noise reduction of this concept stems from the fact that a large number of small jets will produce very high frequency noise and also, if spaced suitably, they will coalesce at a smaller velocity to produce low amplitude, low frequency noise. This is accomplished through detailed acoustic and fluid measurements along with a Computational Fluidic Dynamic (CFD) solution of the mean (DE) Distributed Exhaust nozzle flowfield performed by Northrop-Grumman.

The acoustic performance is quantified in an anechoic chamber. Farfield acoustic data is acquired for a DE nozzle as well as a round nozzle of the same area. Both these types of nozzles are assessed numerically using Computational Fluid Dynamic (CFD) techniques. The CFD analysis ensures that both nozzles issued the same amount of airflow for a given nozzle pressure ratio. Data at a variety of nozzle pressure ratios are acquired at a range of polar and azimuthal angles. Flow visualization of the DE nozzle is used to assess the fluid dynamics of the small jet interactions.

Results show that at high subsonic jet velocities, the DE nozzle shifts its frequency of peak amplitude to a higher frequency relative to a round nozzle of equivalent area (from a S_{tD} = 0.24 to 1.3). Furthermore, the DE nozzle shows reduced sound pressure levels (as much as 4 - 8 dB) in the low frequency part of the spectrum (less than S_{tD} = 0.24) compared to the round nozzle. At supersonic jet velocities, the DE nozzle does not exhibit the jet screech and the shock-associated broadband noise is reduced by as much as 12 dB.

Table of Contents

Description	Page
Foreword/Acknowledgements	i
Executive Summary	ii
Table of Contents	iii
List of Figures	iv
Nomenclature	viii
1.0 Introduction	1
2.0 Distributed Exhaust Nozzle Concept and Design	2
3.0 Technical Approach	20
4.0 Test Facilities, Instrumentation, and Data Acquisition	21
5.0 A Note About How Data Will Be Presented in This Report	28
6.0 Farfield Acoustic Results	30
7.0 DE Nozzle Flow Visualization	54
8.0 Fluid Shielding in Distributed Exhaust Nozzle Arrangement	63
9.0 References	70
Appendix A: Results from Reynolds Averaged Numerical Simulation of DE Nozzle	71
Appendix B: Microphone Correction Methodology	86
Appendix C: 1/3-Octave Band Spectra	95

List of Figures

Page

Figure 2.1 Examples of Distributed Exhaust nozzle design configurations. ---------- 3

Figure 2.2 Northrop-Grumman DE nozzle tested in present study. ---------- 4

Figure 2.3 Interior design of DE nozzle used for current work. ---------- 5

Figure 2.4 Mach number contours from CFD solution of SS6 nozzle with comparison to equivalent flow area round nozzle [NPR = 1.52; NTR = 1.00]. ---------- 8

Figure 2.5 Turbulence intensity contours from CFD solution of SS6 nozzle with comparison to equivalent flow area round nozzle [NPR = 1.52; NTR = 1.00]. ---------- 9

Figure 2.6 Turbulence length scale contours from CFD solution of SS6 nozzle with comparison to equivalent flow area round nozzle [NPR = 1.52; NTR = 1.00]. ------10

Figure 2.7 Internal gage pressure contours from CFD solution of SS6 nozzle with comparison to equivalent flow area round nozzle [NPR = 1.52; NTR = 1.00]. ----------11

Figure 2.8 External surface gage pressure contours from CFD solution of SS6 nozzle with comparison to equivalent flow area round nozzle [NPR = 1.52; NTR = 1.00]. -------12

Figure 2.9 Mach number contours from CFD solution of SS6 nozzle with comparison to equivalent flow area round nozzle [NPR = 2.43; NTR = 1.00]. ----------15

Figure 2.10 Turbulence intensity contours from CFD solution of SS6 nozzle with comparison to equivalent flow area round nozzle [NPR = 2.43; NTR = 1.00]. ----------16

Figure 2.11 Turbulence length scale contours from CFD solution of SS6 nozzle with comparison to equivalent flow area round nozzle [NPR = 2.43; NTR = 1.00]. ------17

Figure 2.12 Internal gage pressure contours from CFD solution of SS6 nozzle with comparison to equivalent flow area round nozzle [NPR = 2.43; NTR = 1.00]. ----------18

Figure 2.13 External surface gage pressure contours from CFD solution of SS6 nozzle with comparison to equivalent flow area round nozzle [NPR = 2.43; NTR = 1.00]. ------19

Figure 4.1 Polar microphone angle orientation in GTRI's Static-Jet Anechoic Facility --------22

Figure 4.2 GTRI Static-Jet facility used for DE nozzle flow visualization. ----------23

Figure 4.3 Effect of upstream pitot-probe on acoustic measurements. ----------25

Figure 4.4 Data acquisition paths for flow and acoustic measurements. ----------26

Figure 6.1 a) Baseline round nozzle b) DE nozzle and orientation of azimuthal microphone positions. ----------31

Figure 6.2 Corrected mass flow of DE nozzle and baseline round nozzle at various nozzle operating pressures. ----------32

Figure 6.3 Farfield noise comparison between DE and round nozzle [$\phi = 90^o$; $\theta = 90^o$; 64 avgs.; $\Delta f = 32$ Hz; SPL adjusted fro R = 12 ft, microphone grid and atmospheric absorption]. ----------33

Figure 6.4 Comparison of farfield spectra; $\phi = 90^o$; R = 12 ft; 64 avgs.; 0-102.4 kHz; $\Delta f = 32$ Hz; $T_j/T_{amb} = 0.975$; NPR = 1.52; $U_j = 830$ ft/s; corrected mass flow = 0.881 lb_m/s.----------35

Figure 6.5 Comparison of farfield spectra; $\phi = 90^o$; R = 12 ft; 64 avgs.; 0-102.4 kHz; $\Delta f = 32$ Hz; $T_j/T_{amb} = 0.975$; NPR = 2.40; $U_j = 830$ ft/s; corrected mass flow = 1.457 lb_m/s.----------36

Figure 6.6 Polar angle trends for farfield noise a) Round nozzle; b) DE nozzle [$\phi = 90^o$; 64 avgs.; $\Delta f = 32$ Hz; SPL adjusted fro R = 12 ft, microphone grid and atmospheric absorption].----------37

Figure 6.7 Polar angle trends for farfield noise a) Round nozzle; b) DE nozzle [$\phi = 90^o$; 64 avgs.; $\Delta f = 32$ Hz; SPL adjusted fro R = 12 ft, microphone grid and atmospheric absorption]. ----------38

Figure 6.8 Azimuthal variation in farfield noise spectra $\theta = 90^o$; 64 avgs.; $\Delta f = 32$ Hz; SPL adjusted fro R = 12 ft, microphone grid and atmospheric absorption].----------39

Figure 6.9 Effect of azimuthal angle on DE nozzle at selected polar angles for NPR = 1.52 [$\theta = 90^o$; 64 avgs.; $\Delta f = 32$ Hz]. ----------41

Figure 6.10 Effect of azimuthal angle on DE nozzle at selected polar angles for NPR = 2.40 [$\theta = 90^o$; 64 avgs.; $\Delta f = 32$ Hz]. ----------42

Figure 6.11 Comparison of OASPL directivity; R = 12 ft; 64 avgs; 0-102 kHz; $\Delta f = 32$Hz; $T_j/T_{amb} = 0.975$. ----------43

Figure 6.12 Comparison of OASPL directivity versus jet velocity; R = 12 ft; 64 avgs; 0-102 kHz; Δf= 32Hz; T_j/T_{amb} = 0.975.----44

Figure 6.13 Velocity dependence of corrected OASPL for DE nozzle [θ = 30°; 64 avgs; SPL adjusted for R = 12 ft and atmospheric absorption].----46

Figure 6.14 Velocity dependence of corrected OASPL for DE nozzle [θ = 60°; 64 avgs; SPL adjusted for R = 12 ft and atmospheric absorption].----47

Figure 6.15 Velocity dependence of corrected OASPL for DE nozzle [θ = 90°; 64 avgs; SPL adjusted for R = 12 ft and atmospheric absorption].----48

Figure 6.16 Velocity dependence of corrected OASPL for DE nozzle [θ = 120°; 64 avgs; SPL adjusted for R = 12 ft and atmospheric absorption].----49

Figure 6.17 Comparison of present data with database of jet noise data from laboratory and engine tests; peak noise polar angle [ref. 3 – Ahuja and Bushell]. ----50

Figure 7.1 Viewing planes for PIV diagnostic imagery. ----55

Figure 7.2 Instantaneous velocity at mid-span plane [PIV results]. ----56

Figure 7.3 Instantaneous velocity at mid-span plane comparison with mean Mach number numerical solution.----57

Figure 7.4 Observed flapping of DE jet downstream of nozzle exit at NPR = 1.52. ----58

Figure 7.5 Instantaneous velocity at cross exit plane of the DE nozzle [PIV results].----59

Figure 7.6 Planar image of DE nozzle exhaust flow showing individual slit-jets issuing in streamwise direction revealing merging location and jet instabilities [NPR = 1.12, U_j = 463 ft/s].----61

Figure 7.7 Planar image of DE nozzle exhaust flow showing individual slot-jets issuing in streamwise direction revealing merging location and jet instabilities [NPR = 152].----62

Figure 8.1 Microphone arrangement for testing of individual DE nozzle slots.----64

Figure 8.2 Configurations of DE nozzle used to examine individual slot-jets.----65

Figure 8.3 Effect of individual slot-jets of the DE nozzle on farfield noise [NPR = 1.52; ϕ = 90°; R = 12 ft; Corrected for atmospheric absorption]. ----66

Figure 8.4 Effect of one, four, and seven slot-jets of the DE nozzle on farfield noise [NPR = 1.52; $\phi = 90^{o}$; R = 12 ft; Corrected for atmospheric absorption]. ----------68

Figure 8.5 Effect of individual slot-jets of the DE nozzle on farfield noise [NPR = 1.52; $\phi = 90^{o}$; R = 12 ft; Corrected for atmospheric absorption]. ----------69

Nomenclature

A_j	Exit area of jet
a_o	Ambient speed of sound
k	From k-ω turbulence model – $1/2\Sigma(u'^2 + v'^2 + w'^2)$
ℓ	Turbulence length scale
M_j	Fully expanded jet Mach number
M_c	Eddy convection Mach number
NPR	Nozzle Pressure Ratio P_{Tj}/P_{amb}
NTR	Nozzle Temperature Ratio T_{Tj}/T_{amb}
OASPL	Overall Sound Pressure Level
P_{Tj}	Jet total pressure
P_{sj}	Jet static pressure
R	Radial distance from nozzle exit to microphone
$S_{t\text{-}D}$	Strouhal Number based on equivalent jet exit diameter
T_{Tj}	Jet total temperature
T_{sj}	Jet static temperature
u', v', w'	Fluctuating velocity in x-direction, y-direction, and z-direction respectively
γ	Ratio of specific heats
ϕ	Azimuthal angle
ρ_j	Density of jet
$\rho_{\sigma\tau\delta}$	Standard day density
θ	Polar angle
ω	(ε/k*Constant) from k-ω turbulence mo

1.0 Introduction

The aerospace community is being challenged to reduce the environmental impact of aeronautics and space transportation. This is evident in the three pillar goals of NASA that include reducing the perceived noise levels of the future aircraft by a factor of two (10 EPNdB) from today's subsonic aircraft within ten years and by a factor of four (20 EPNdB) within 25 years. These goals are extremely ambitious and to achieve them will require innovation thinking and new concepts. This report documents one such concept, the Distributed Exhaust (DE) nozzle. The main objective of this study was to validate the jet noise reduction potential of this concept. This was accomplished through detailed acoustic and fluid measurements along with a Computational Fluidic Dynamic (CFD) solution of the mean DE nozzle flowfield.

2.0 Distributed Exhaust Nozzle Concept and Design

The Distributed Exhaust (DE) nozzle concept is based upon splitting the exhaust system stream into a large number of very small exhaust plumes by discharging the flow through an array of small, appropriately spaced openings. Typical examples of such plumes using horizontal slots and triangular slots with chimney extensions are shown in Figure 2.1a and b, respectively. The potential of noise reduction stems from the fact that a large number of small jets will produce very high frequency noise and also, if spaced suitably, they will coalesce at a smaller velocity to produce low amplitude, low frequency noise. This concept is based upon a patent[1] and work conducted by Northrop-Grumman.

The design of the experiments described here was guided by the results of an earlier experiment conducted by NASA/Northrop-Grumman team, who tested a horizontal slot configuration at the NASA Langley Low Speed Anechoic Wind Tunnel. Both acoustic and thrust measurements were made[2]. It was determined that due to an insufficient spacing between the individual jets, the nozzle flow coalesced sooner than expected and produced noise comparable to the baseline 2D reference nozzle. Furthermore, it was felt that self-noise of the horizontal slots themselves contributed to the overall measured noise.

Our DE nozzle, designed by Northrop-Grumman, had individual jets that were spaced farther apart and were vertical instead of horizontal. Figure 2.2 and 2.3 show this new design. It consists of two pieces: a round to rectangular transition and a converging section that splits the exhaust stream into 14 equally spaced vertical slots. The latter having 7 slots on the upper slope and 7 slots on the lower slope of the nozzle. The slots were about 0.115 inches wide and were 4.5-inches along the slope of the nozzle. The projected height of each slot was about 1.2 inches.

Evolution of the Distributed Exhaust Design

Designing distributed exhaust nozzle wind-tunnel models is challenging because scale models dictate that relatively small exhaust holes be even smaller while their walls withstand the same pressures as full-scale nozzles. Thickening these walls to strengthen the model tends to increase drag and distort the plume characteristics. If the model is viewed as a full-scale portion of a nozzle, the limited number of mini-nozzles may overstate edge effects.

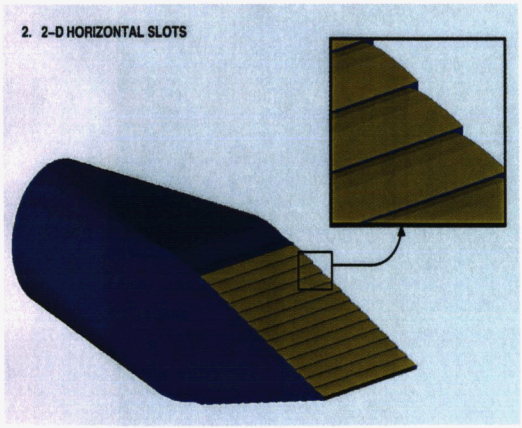

a) DEN with horizontal slots

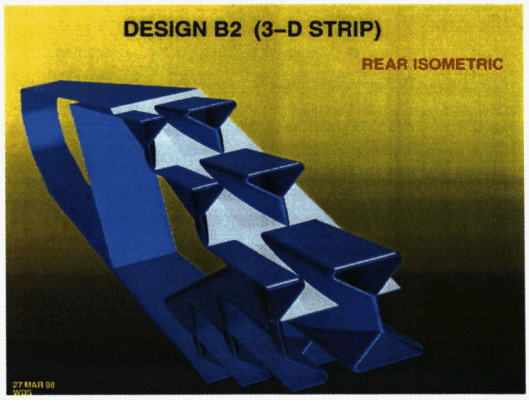

b) DEN with triangular nozzles

Figure 2.1 Examples of Distributed Exhaust nozzle design configurations.

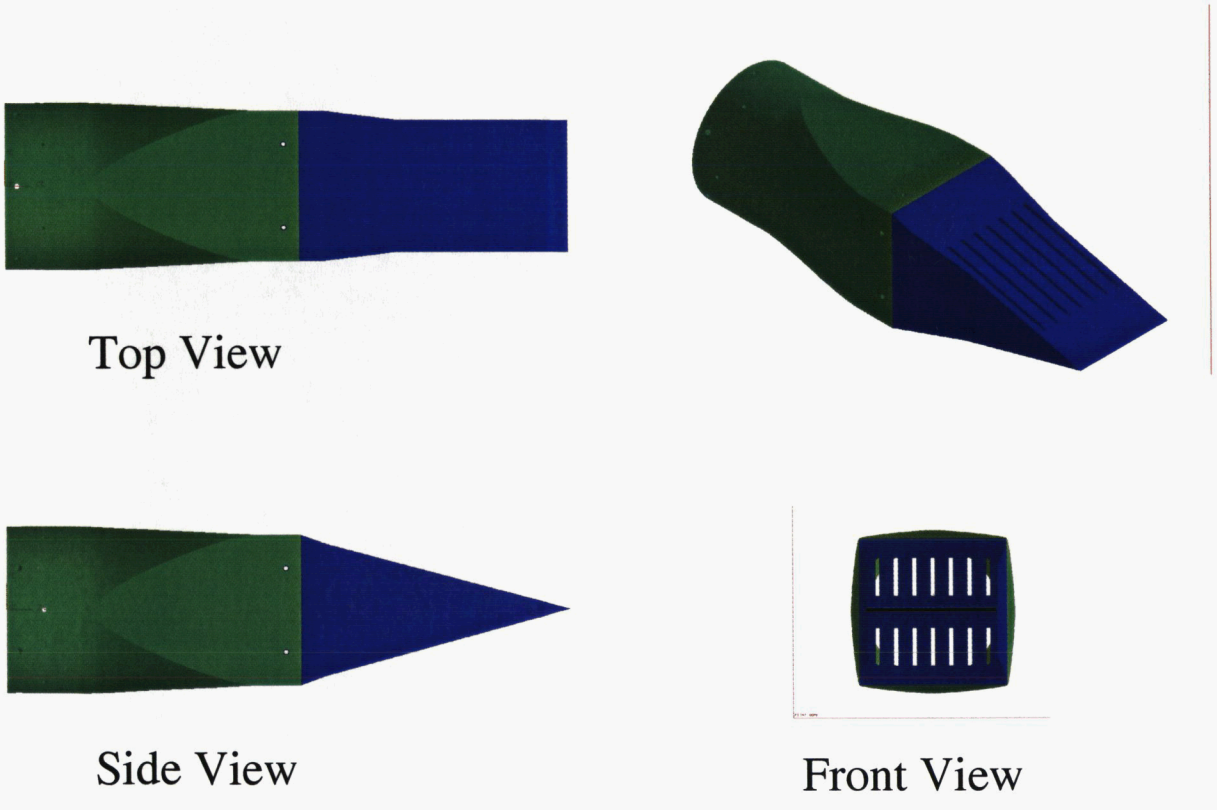

Figure 2.2 Northrop-Grumman DE nozzle tested in present study.

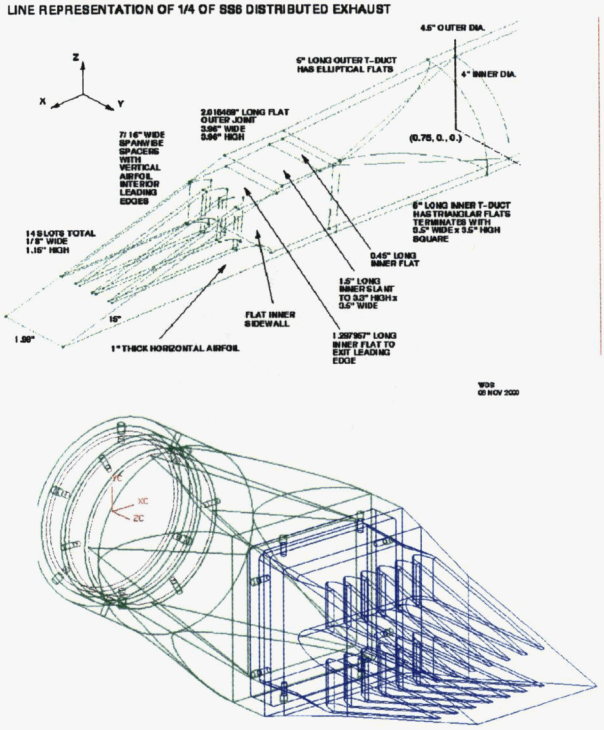

a) Wire Frame drawing of DE nozzle

b) Forward-looking-aft view of DE nozzle interior

Figure 2.3 Interior design of DE nozzle used for current work.

The design of the wind tunnel model to be tested evolved as a function of budget, schedule, the size of the test facility, the goals of GTRI and Northrop Grumman, and each organization's capabilities and experience. Originally, GTRI envisioned a hand-manufactured metal model with horizontal slots, based on Northrop Grumman's previous design tested at NASA Langley Research Center's Jet Noise Lab. Northrop Grumman preferred to investigate a derivative of a vertical slanted-slot design which earlier CFD studies indicated would have different plume coalescence characteristics. GTRI proposed hardware for this concept featuring slanted removable endplates to accommodate testing of nozzle variations, and a transition duct with the downstream rectangular exit circumscribed by the upstream diameter for manufacturing economy.

Northrop Grumman's earlier studies indicated that the proposed transition duct would not provide enough area for both an acceptable number of slots and sufficient spacing between them to delay plume coalescence. Northrop Grumman CFD investigated variations of slanted slots compatible with the removable endplate approach, but concluded that none provided an acceptable level of thrust and/or mass flow.

Removable endplates could probably be facilitated by more complex designs, but the CFD budget had not been estimated with such designs in mind, nor would they be easily hand-manufactured. The design refinement proceeded toward the goal of obtaining additional acoustic insight from a model of relative simplicity. A minimum wall thickness consistent with the steel round reference nozzle and facility hardware was used.

After completing the CFD runs, Northrop Grumman provided line drawings and dimensions to GTRI for AutoCAD modeling and model construction. GTRI suggested that a stereolithography model might be more appropriate, based on their latest experience. Northrop Grumman provided stereolithography files from Unigraphics version 15 with thicker walls over the upstream portion of the model than were analyzed in CFD. The impact of this difference on flow qualities should be minimal for the (static) wind-tunnel tests.

Numerical Results

CFD results between a round reference nozzle and the slanted slot DE nozzle (designated SS6) are now presented. The round reference nozzle has a 4″ upstream diameter and a 1.6″ exit diameter, yielding a 6.28 contraction ratio to a 2.00 square inch exit area. Nozzle SS6 has a 4″ upstream diameter and fourteen 1/8″ wide by 1.15″ high exit slots slanted on a 15 degree half-angle wedge, yielding a 6.24 contraction ratio to a 2.01 square inch aft-projected exit area. CFD dictated the slight increase in exit area (0.596%) for matching mass flow between the two nozzles. It compensates for the increased total boundary layer thickness associated with the SS6 nozzle's 7.12 times larger exit perimeter.

The following figures show contours of various jet properties for both the baseline round nozzle and the DE nozzle from the CFD results. Figure 2.4 shows the entire range of Mach number contours for this condition. The waterline cut in the bottom-most figure is at half the slot height rather than at SS6's center plane to show interaction between jets. Figure 2.5 shows the corresponding turbulence intensity. The three components (u′, v′, and w′) were of similar magnitude for the round jet. The maximum values were 16.2% for the round nozzle and 20.7% for SS6. The round reference nozzle's exit station centerline velocity of 840 feet per second was used to normalize the results of both nozzles. Turbulence length scales from Mentor's Shear Stress Transport turbulence model are compared in Figure 2.6. The maximum length scale for both nozzles was slightly greater than 0.5 inch (around 1/3 of the reference nozzle exit diameter).

The gage pressures in Figure 2.7 indicate a maximum net pressure on the walls of about 8 p.s.i. for a nozzle pressure ratio, PVPR, of 1.52. The finer scale for color resolution in Figure 2.8 is useful for evaluating the external pressure drag penalty associated with the SS6 nozzle. The slightly positive pressure along the horizontal spacer was anticipated. Since thrust stands only measure exit thrust minus external drag, Northrop Grumman prefers to present thrust comparisons the same way. Bookkeeping of the external drag begins 24″ upstream of the test facility connection point. At this non-choked condition, the round reference provided 25.34 lb_f thrust to yield a nozzle net CFG of 0.98542. The external drag penalty included in this number was only 0.150% of the ideal thrust. The predicted CFD thrust for the SS6 nozzle, when corrected for a slight mass flow deficit

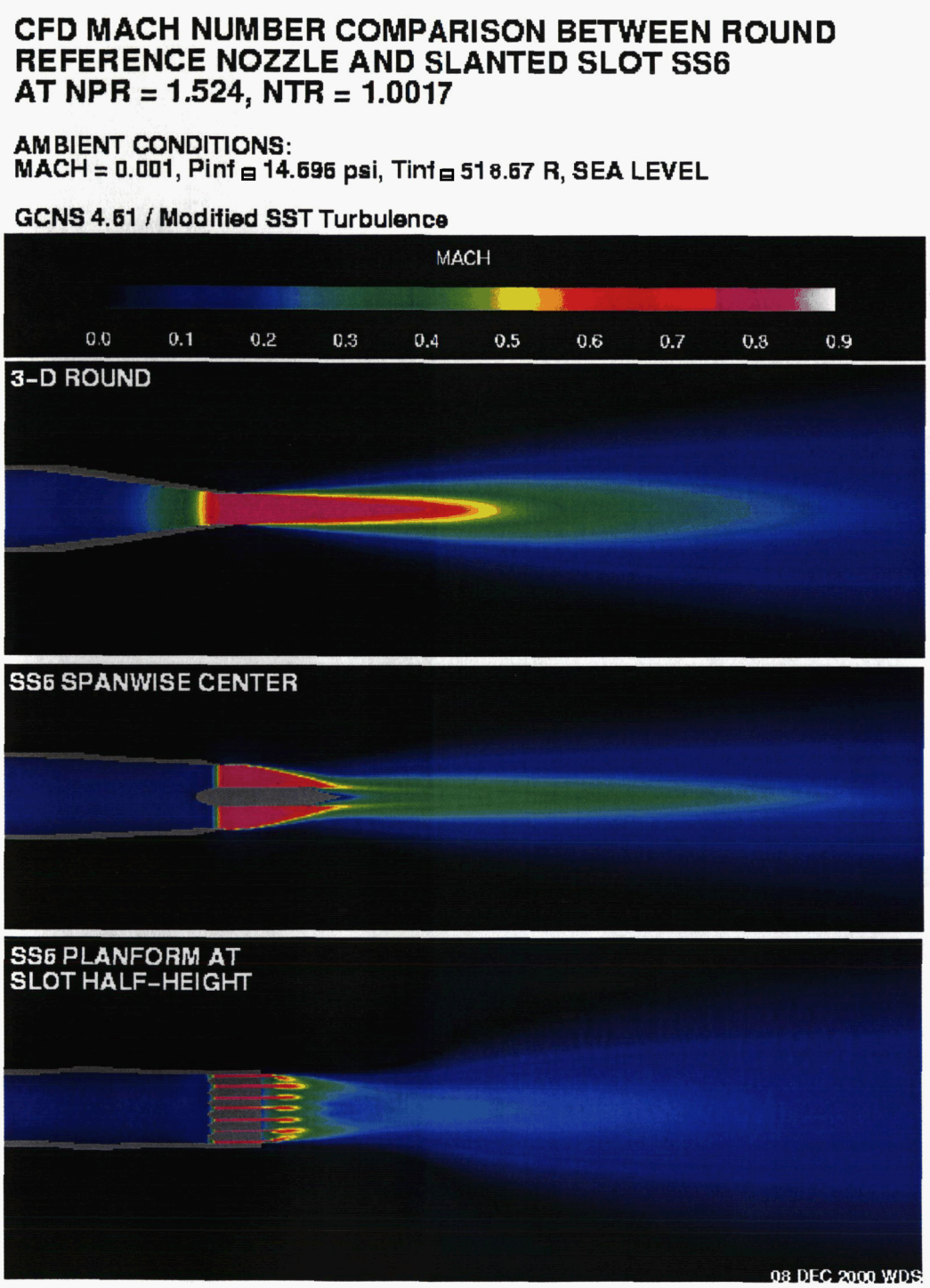

Figure 2.4 Mach number contours from CFD solution of SS6 nozzle with comparison to equivalent flow area round nozzle [NPR = 1.52; NTR = 1.00].

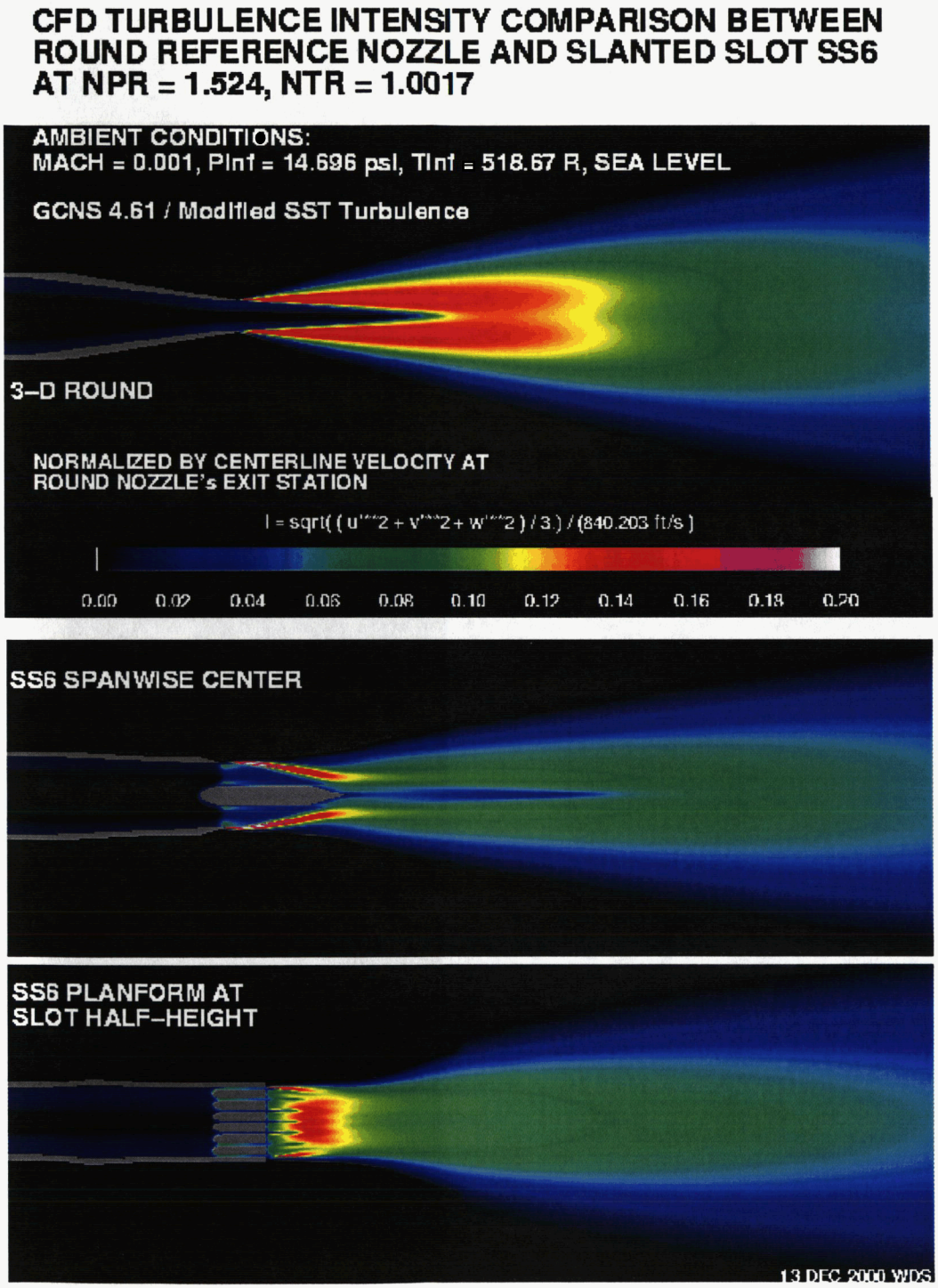

Figure 2.5 Turbulence intensity contours from CFD solution of SS6 nozzle with comparison to equivalent flow area round nozzle [NPR = 1.52; NTR = 1.00].

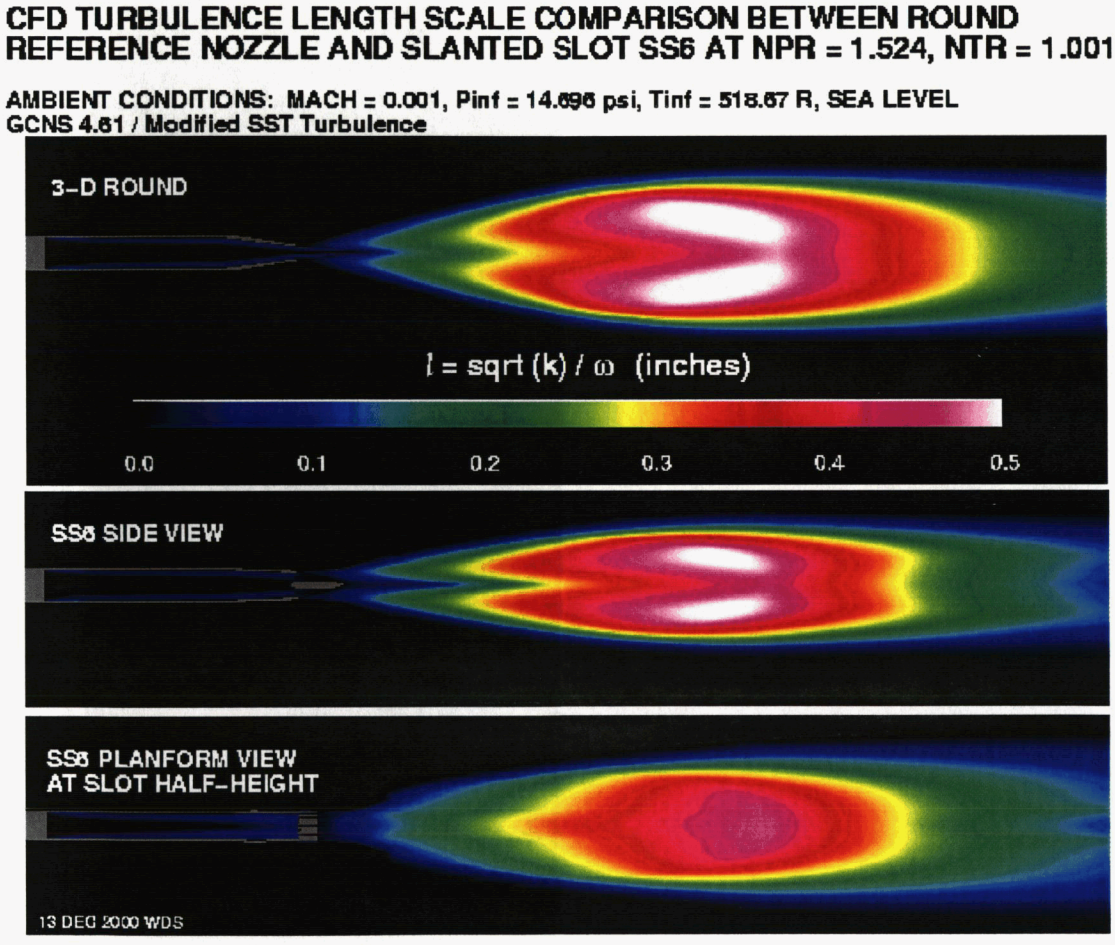

Figure 2.6 Turbulence length scale contours from CFD solution of SS6 nozzle with comparison to equivalent flow area round nozzle [NPR = 1.52; NTR = 1.00].

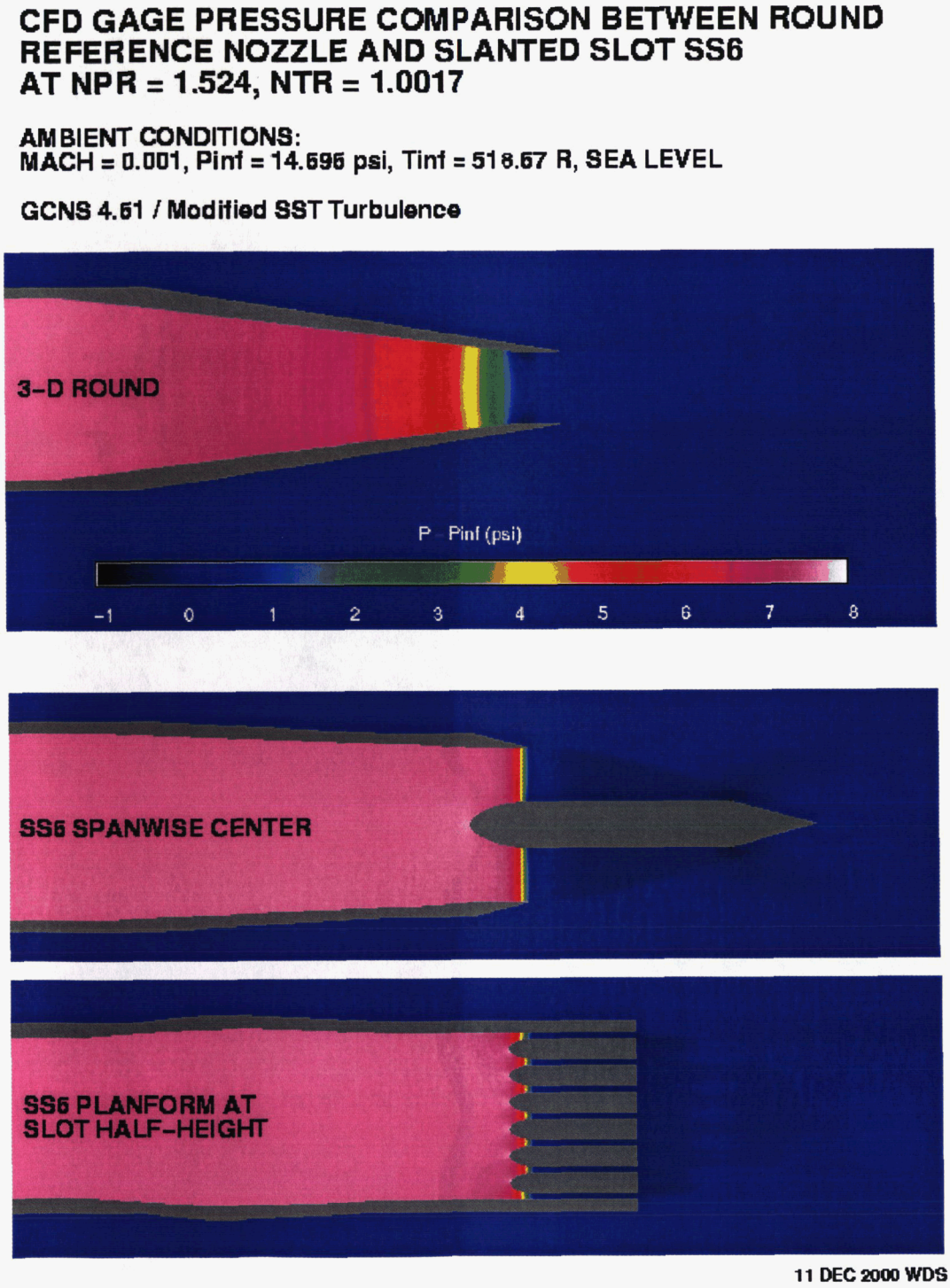

Figure 2.7 Internal gage pressure contours from CFD solution of SS6 nozzle with comparison to equivalent flow area round nozzle [NPR = 1.52; NTR = 1.00].

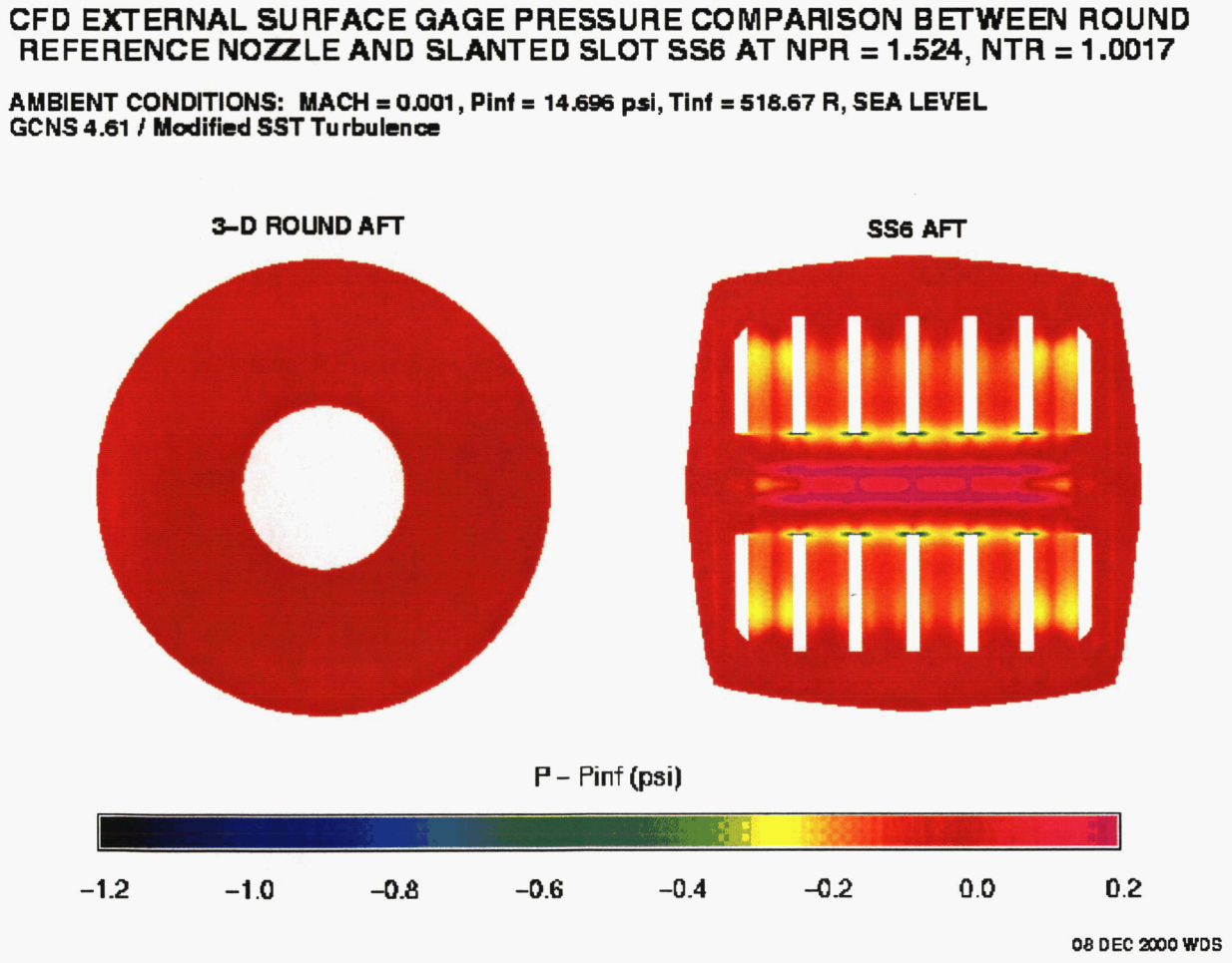

Figure 2.8 External surface gage pressure contours from CFD solution of SS6 nozzle with comparison to equivalent flow area round nozzle [NPR = 1.52; NTR = 1.00].

(98.9328% of the reference nozzle's 0.98289 lb_m/s flow rate), was 87.416% of the reference nozzle. The external drag accounted for less than 5% loss.

Similar to the calculations discussed above for a subsonic condition , CFD calculation were carried out for a supersonic condition , namely NPR = 2.45. The jet was operated choked and unheated. Figure 2.9 shows the entire range of Mach number contours for the NPR = 2.45 condition. The waterline cut is again at half the slot height rather than at SS6's center plane to show interaction between jets.

Figure 2.10 shows the corresponding turbulence intensity. The maximum values were 18.6% for the round nozzle and 25.1% for SS6. The round reference nozzle's exit station centerline velocity of 1040.733 feet per second was used to normalize the results of both nozzles.

Turbulence length scales from Mentor's Shear Stress Transport turbulence model are compared in Figure 2.11. The maximum length scale for both nozzles was about 0.65 inch (around 41% of the reference nozzle exit diameter).

The gage pressures in Figure 2.12 indicate a maximum net pressure on the walls of about 22 p.s.i. at this condition. Figure 2.13 shows external surface gage pressures. The finer scale for the color resolution from Figure 2.8 is retained here to show the greater amount of pressure drag for this condition. The pressure along the spacer is again slightly positive.

At this choked condition, the round reference provided 59.50333 lbf thrust to yield a nozzle net CFG was 0.99229. The external drag penalty included in this number was only 0.008% of the ideal thrust. The predicted CFD thrust for the SS6 nozzle, when corrected for a slight mass flow advantage (100.3950% of the reference nozzle's 1.63224 lbm/s flow rate), was 89.902% of the reference nozzle. The external drag again accounted for less than 5% loss.

The intent of the DE nozzle is to reduce jet noise by shifting the bulk of the mixing noise energy to higher frequencies which are less audible and more readily attenuated during atmospheric

propagation. Minimizing the residual low frequency noise due to downstream coalescence of the mini-plumes is critical to the distributed exhaust's acoustic performance. Additional CFD results are presented in Appendix A. The isosurface comparisons shown indicate that significant coalescence of the individual plumes occurs at about half the exit Mach number, suggesting that low frequency noise reduction from this design should be dramatic for both the subsonic and supersonic jet flow cases.

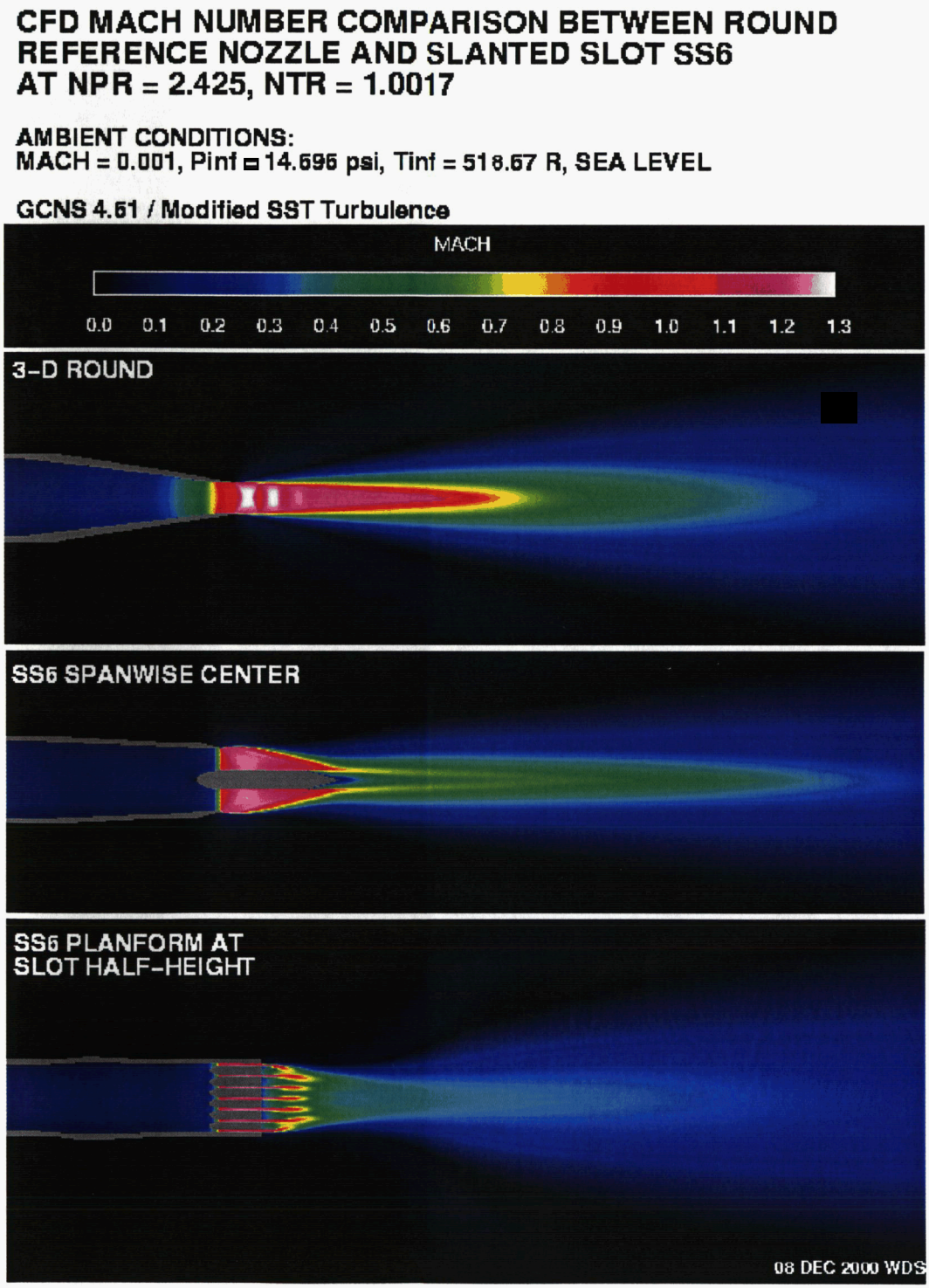

Figure 2.9 Mach number contours from CFD solution of SS6 nozzle with comparison to equivalent flow area round nozzle [NPR = 2.43; NTR = 1.00].

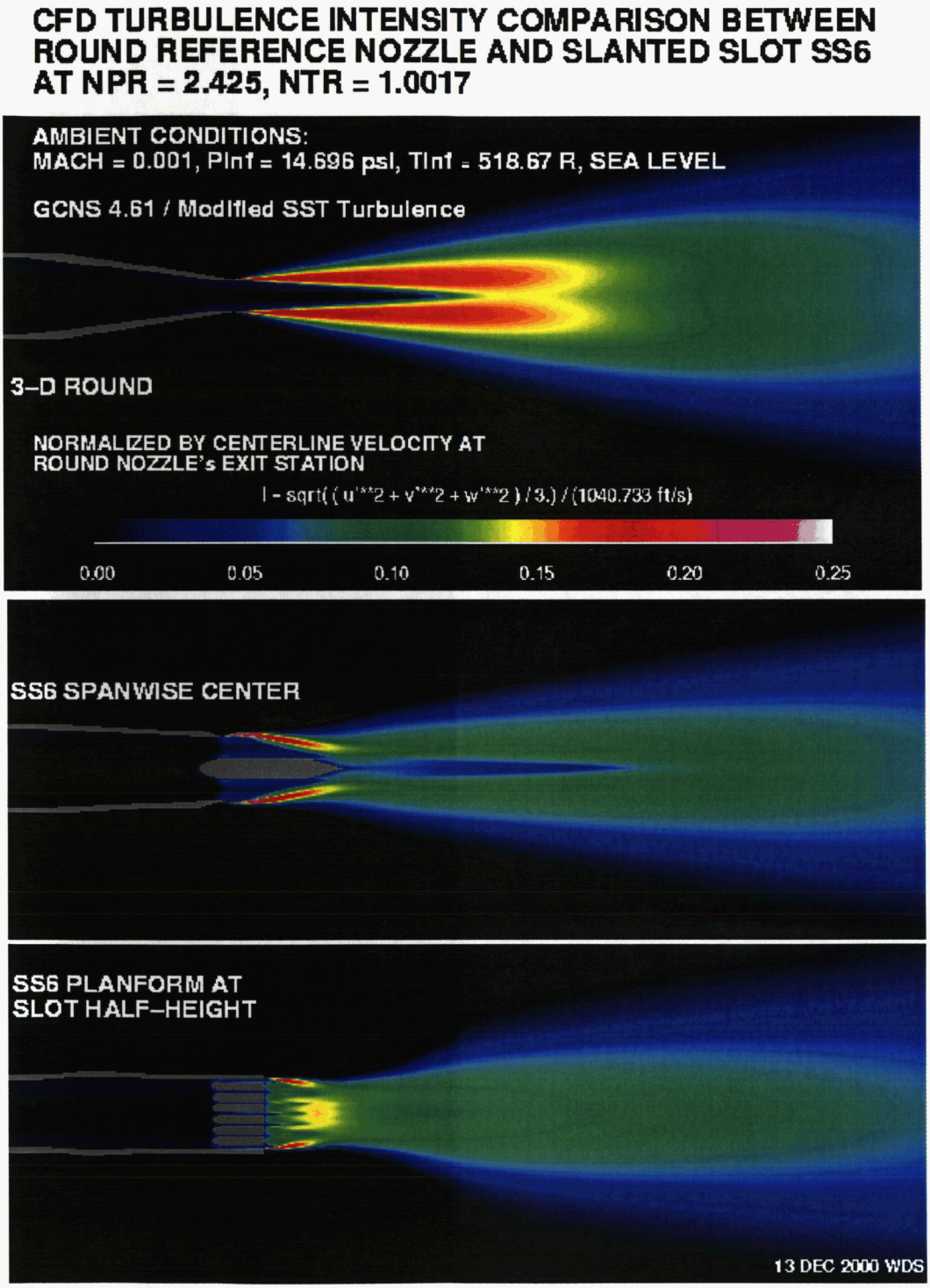

Figure 2.10 Turbulence intensity contours from CFD solution of SS6 nozzle with comparison to equivalent flow area round nozzle [NPR = 2.43; NTR = 1.00].

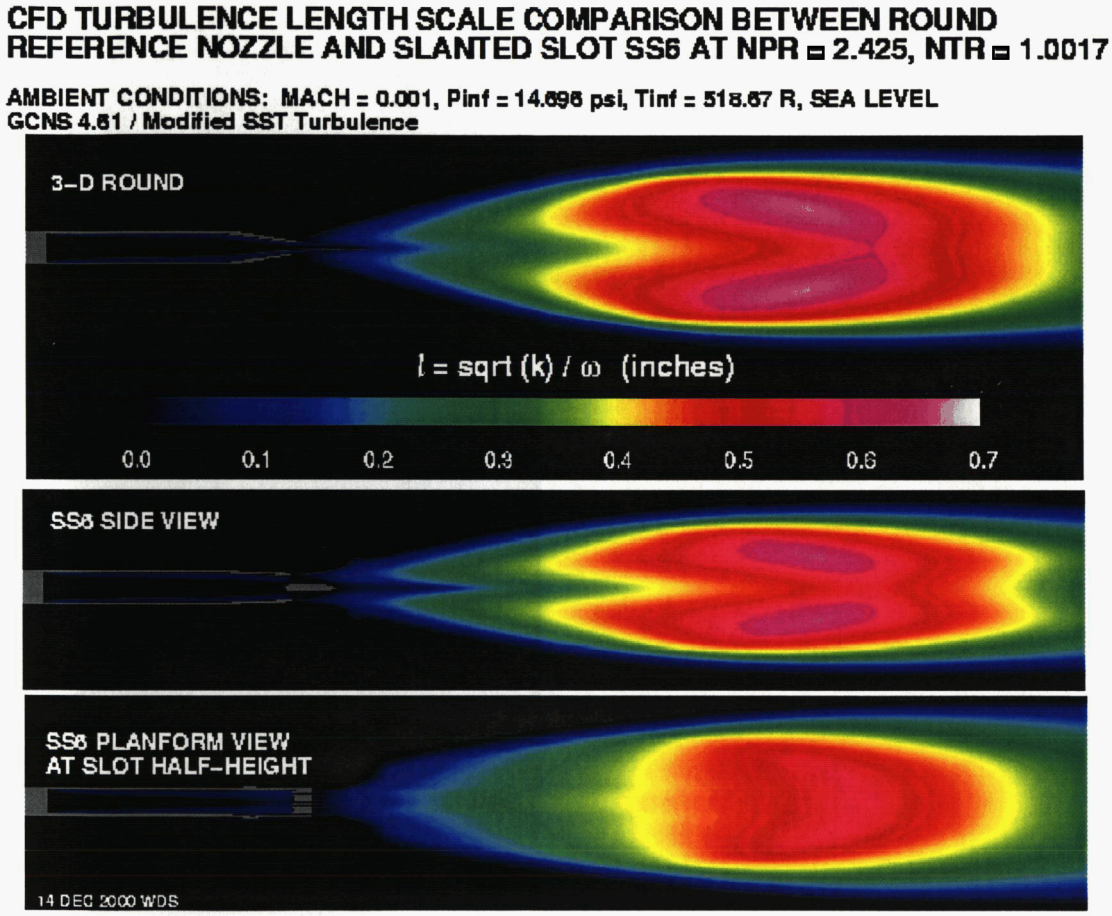

Figure 2.11 Turbulence length scale contours from CFD solution of SS6 nozzle with comparison to equivalent flow area round nozzle [NPR = 2.43; NTR = 1.00].

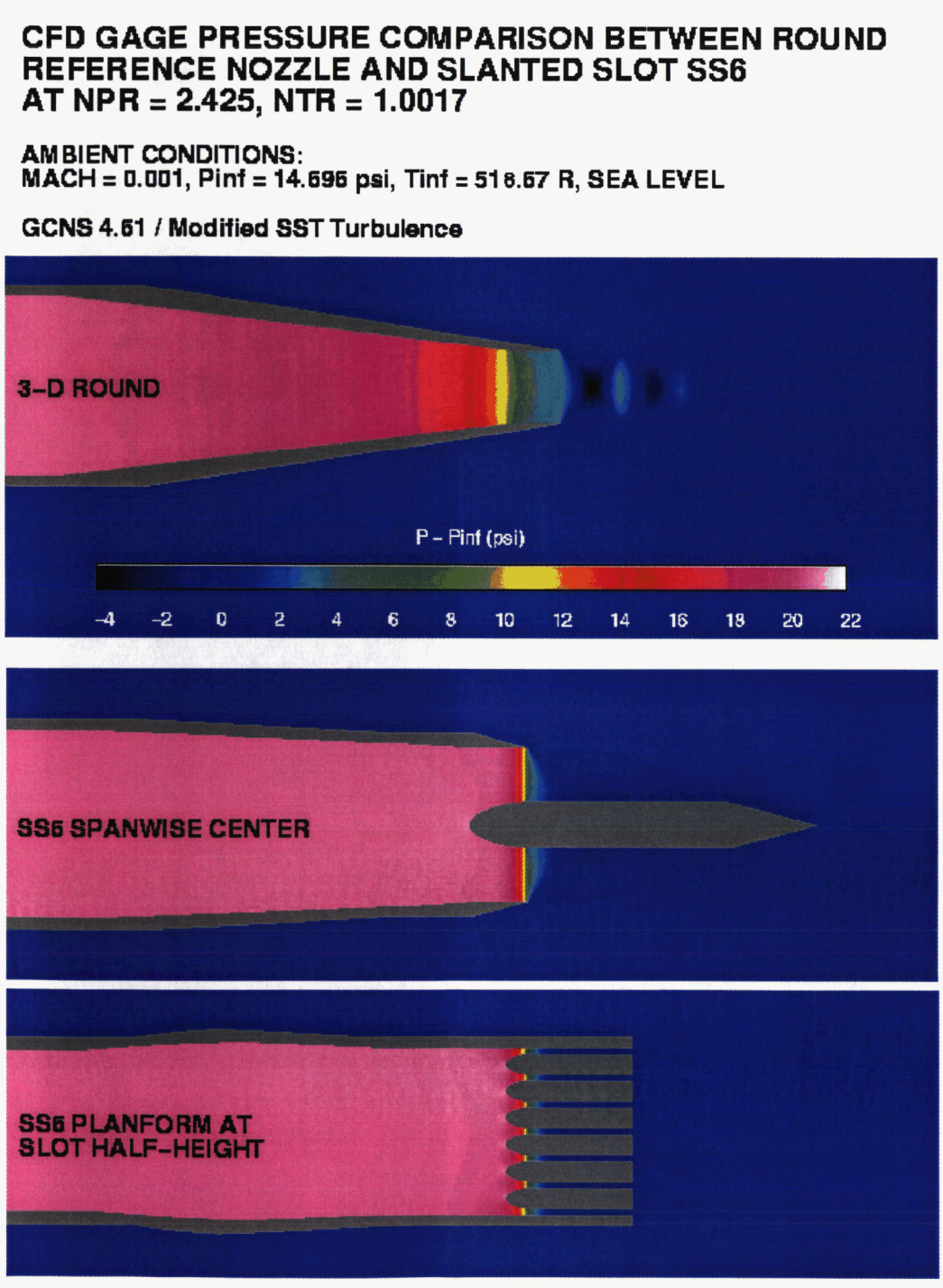

Figure 2.12 Internal gage pressure contours from CFD solution of SS6 nozzle with comparison to equivalent flow area round nozzle [NPR = 2.43; NTR = 1.00].

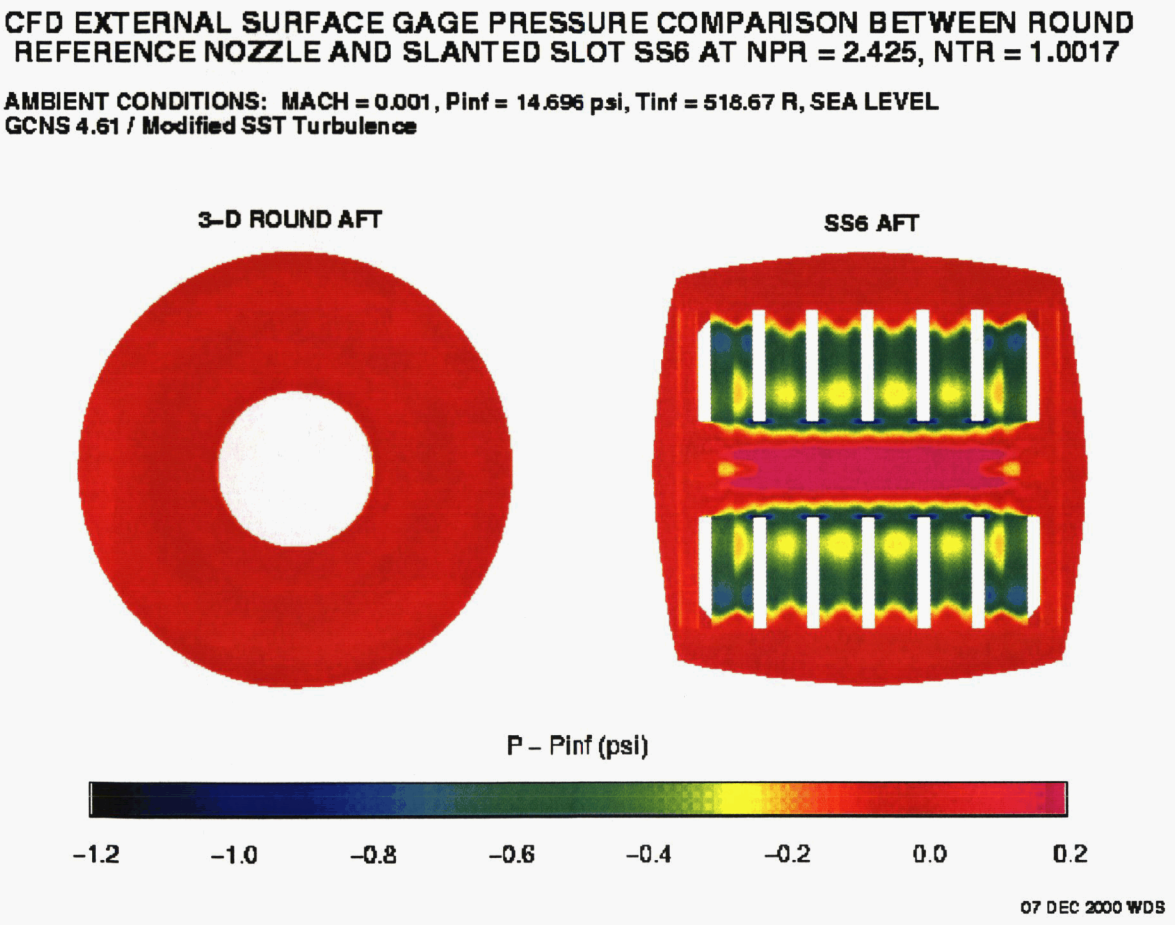

Figure 2.13 External surface gage pressure contours from CFD solution of SS6 nozzle with comparison to equivalent flow area round nozzle [NPR = 2.43; NTR = 1.00].

3.0 Technical Approach

The objective of the present study was to assess the farfield noise performance of the Distributed Exhaust (DE) nozzle. In addition to acoustic data, jet flow visualization was obtained of to facilitate understanding of its performance.

Acoustic Performance

The acoustic performance was quantified in an anechoic chamber with through-flow static jet capability. Evaluating the acoustic performance of the DE nozzle in the farfield necessitates the parallel acquisition of acoustic data for a conventional, round jet for comparison. Therefore, a round nozzle exit area equal to that of the DE nozzle was fabricated using Computational Fluid Dynamic (CFD) numerical techniques. The CFD analysis ensured that both nozzles exhausted the same amount of airflow for a given nozzle pressure ratio. Farfield noise was measured first for both nozzles at a variety of nozzle pressure ratios.

Flow Visualization

The flow structure of the DE nozzle was visualized using Particle Image Velocimetry (PIV). Seeding the flow through the DE nozzle allowed a laser sheet and a high performance CCD camera to capture the instantaneous velocity vector fields for the nozzle exhaust.

4.0 Test Facilities, Instrumentation, and Data Acquisition

Static Jet Anechoic Facility

The farfield acoustic data was acquired in GTRI's Static Jet Anechoic Facility. The chamber measures 6.7 m long by 6.1 m wide and is 3.5 m high between structural walls. All interior surfaces are lined with polyurethane foam wedges 38 cm long, rendering the facility 99 percent echo free at frequencies above 200 Hz. Two independently controlled air supply ducts allow single and co-annular jet noise measurements to be made. Both flow duct plenums maintain a flow area to nozzle exit area greater than 36:1 up to the nozzle inlet, and in-line duct mufflers minimize the propagation of unwanted noise generated upstream into the anechoic chamber. The air supply to the facility originates from a 2.07 x 10^6 N/m compressor, which supplies clean, dry air to the entire research center facilities. (Only the primary flow was used in this investigation. All tests were performed for the unheated flow.) The facility is designed to produce parallel, low-turbulence, coaxial flows, or single-stream flow with provision for simulating flight effects with a large secondary nozzle. The primary flow enters through a 25.6 cm diameter plenum, followed by an initial contraction to a 10.2 cm diameter acoustic source section duct. For 50.8 mm diameter test nozzles, the plenum-to-nozzle area contraction is 25. The flow in this facility may be heated to temperatures up to 2100°R at pressure ratios exceeding 4.

Microphones may be placed anywhere in the room up to a distance of 38 cm from the wedge tips, so as to be beyond any wedge near field effects. Ten microphones are typically mounted on a plar arc for measuring the farfield spectra of the jet at different polar angles. Figure 4.1 shows the nomenclature and arrangement of these microphones relative to the jet exit. Typically, the microphones at $\theta = 30^\circ$, 40°, 50°, 60°, 70°, 80°, and 90° are located at a measurement radius of 12 feet. The microphones at $\theta = 100^\circ$ and 110° are located at 11 feet. The $\theta = 120^\circ$ microphone is located at 7 feet.

Jet Flow Visualization Facility

The flow visualization data was acquired in another static jet facility, shown in Figure 4.2. This facility has a high pressure flow seeder for Particle Image Velocimetry (PIV) data acquisition. This facility is designed to produce parallel, low-turbulence, coaxial flows, or single-

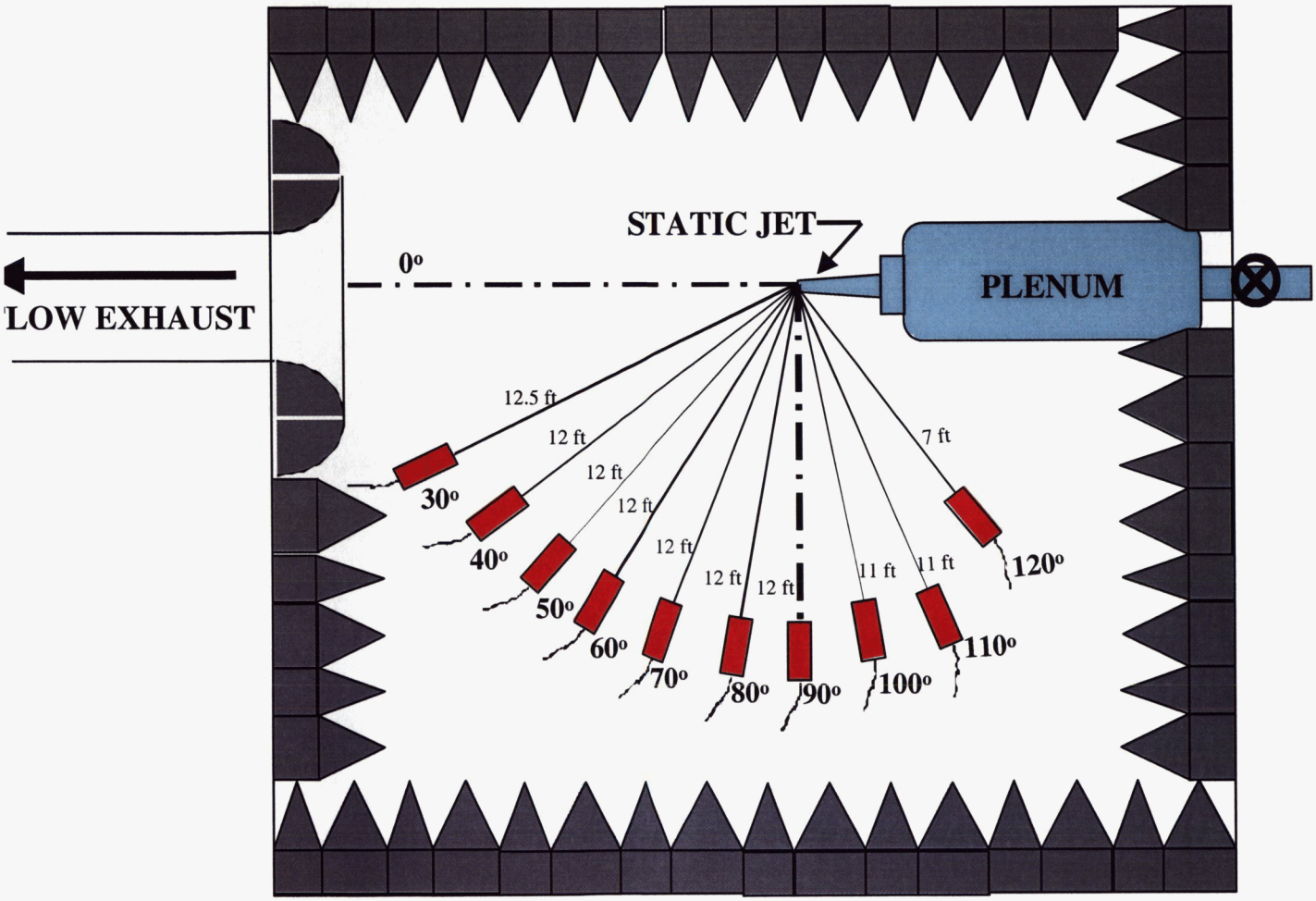

Figure 4.1 Polar microphone angle orientation in GTRI's Static Jet Anechoic Facility

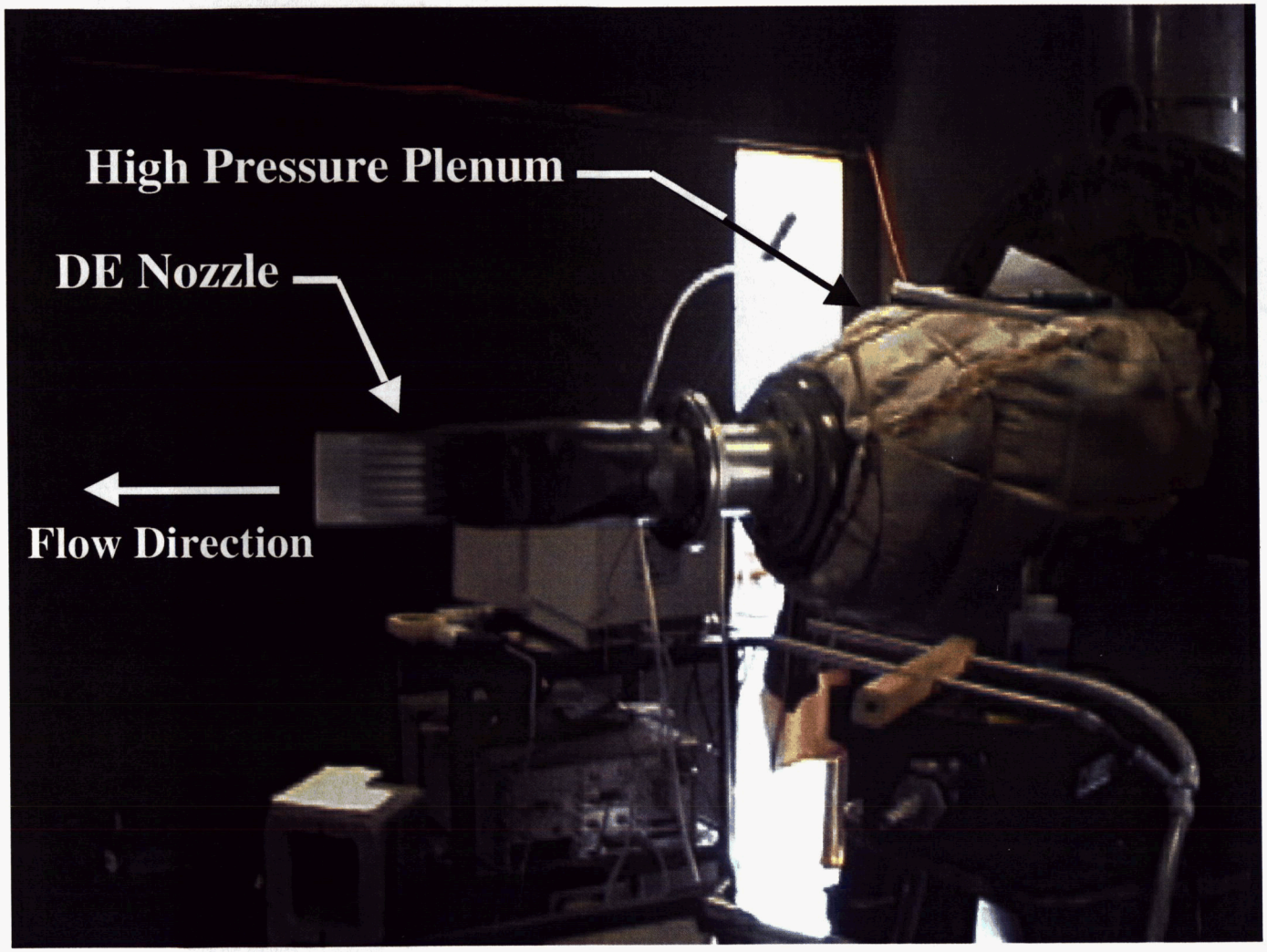

Figure 4.2 GTRI Static-Jet facility used for DE nozzle flow visualization.

stream flow with provision for simulating flight effects with a large secondary nozzle. The primary flow enters through a 25.6 cm diameter plenum, followed by an initial contraction to a 10.2 cm diameter acoustic source section duct. For 50.8 mm diameter test nozzles, the plenum-to-nozzle area contraction is 25. The flow in this facility may be heated to temperatures up to 2100°R at pressure ratios exceeding 4.

The flow seeder consists of a pressurized fluidized bed. Shop air is used to force titanium-oxide particles through conduit that enters the primary jet plenum. These particles are then visualized and used in the PIV data acquisition process.

Instrumentation

Acoustic pressure levels in the farfield were acquired with condenser microphones. These were Bruel & Kjaer (B&K) 4939 quarter-inch microphones, which were used in conjunction with a half-inch B&K 2669 pre-amplifier and adapter. The microphones were powered by a B&K 2609 Nexus power supply and amplifier.

Jet flow data was acquired using a pitot-static thermocouple probe located upstream of the nozzle exit in the round portion of the supply duct. Figure 4.3a shows this set-up. This probe measured the total and static pressure as well as the total temperature of the flow just upstream of the nozzle exit. The probe was present during all of the acoustic data acquisition process and therefore had the potential of affecting farfield noise due to its presence. It was verified that its presence did not affect the farfield spectra by comparing data with and without the probe in place (an upstream plenum pressure was used to repeat jet operating conditions). Figure 4.3b shows typical sound pressure level spectra obtained with and without the flow probe installed. It can readily be seen that the effect of the probe is negligible. Furthermore, no effect was seen at supersonic jet velocities.

Data Acquisition

The acoustic signals were fed into a Hewlett-Packard (HP) 3667A Multi-Channel Signal Analyzer for FFT analysis. The analyzer was operated from a Windows 98 platform on a 200 MHz-based computer. Figure 4.4 shows a schematic of the signal processing paths involved.

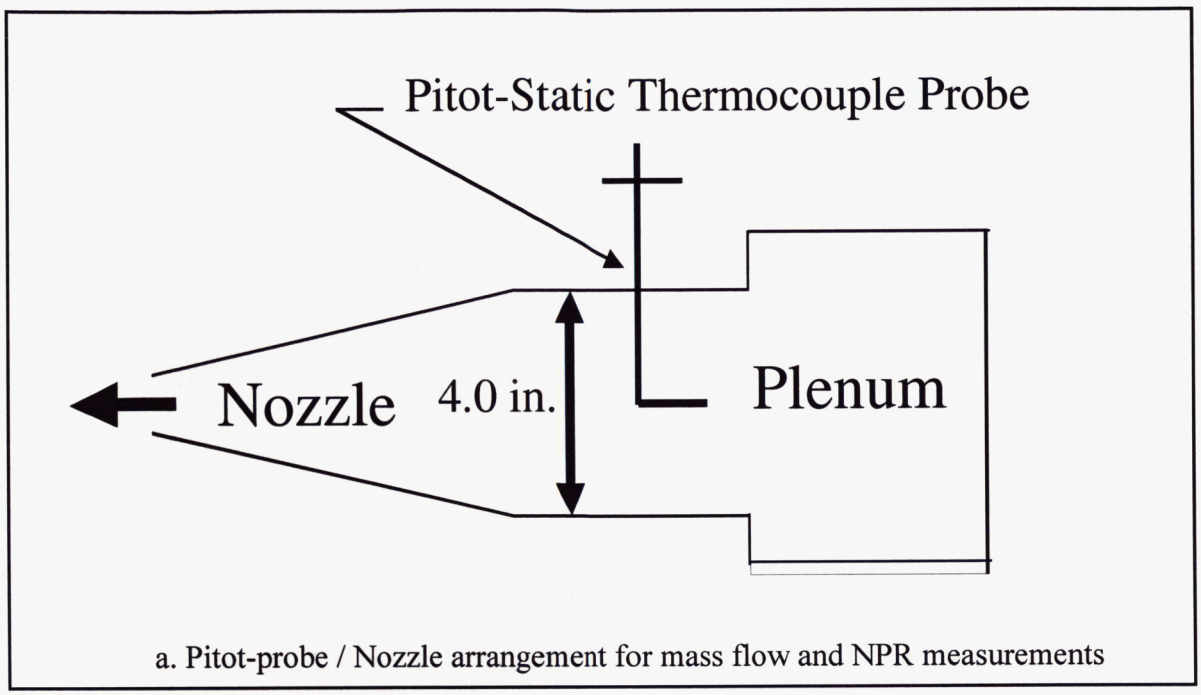

a. Pitot-probe / Nozzle arrangement for mass flow and NPR measurements

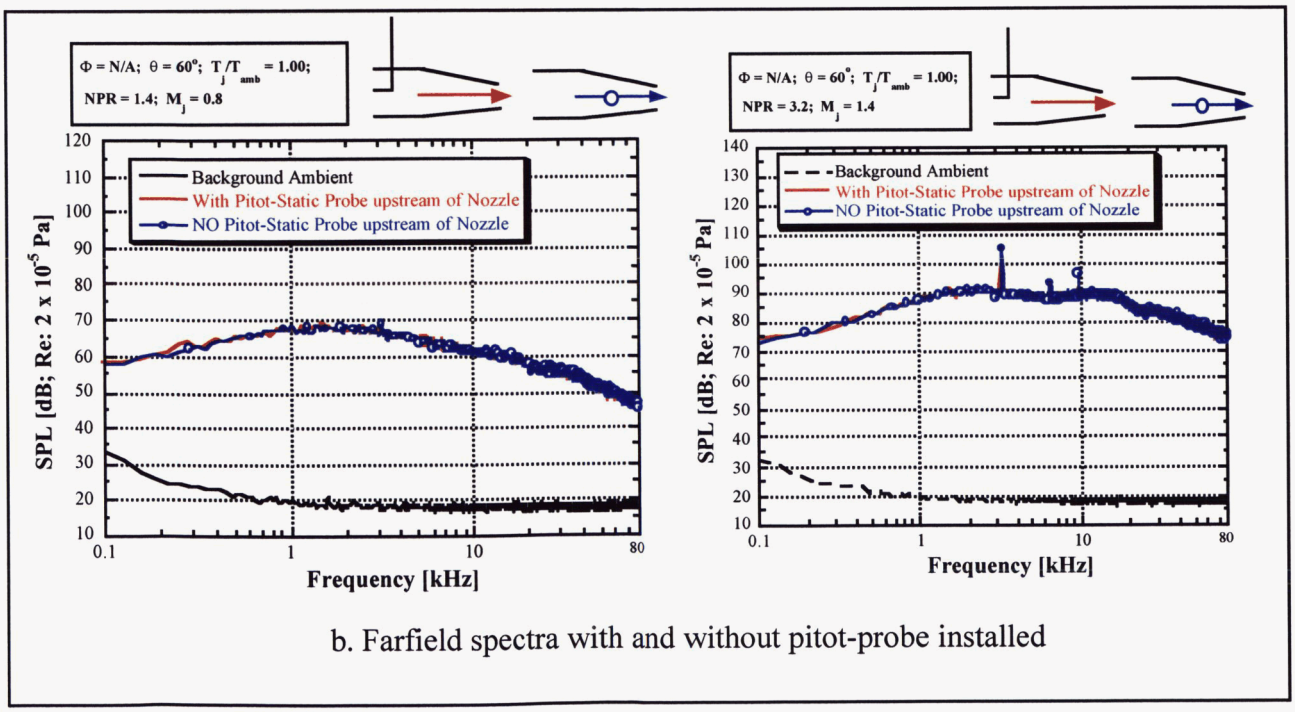

b. Farfield spectra with and without pitot-probe installed

Figure 4.3 Effect of upstream pitot-probe on acoustic measurements.

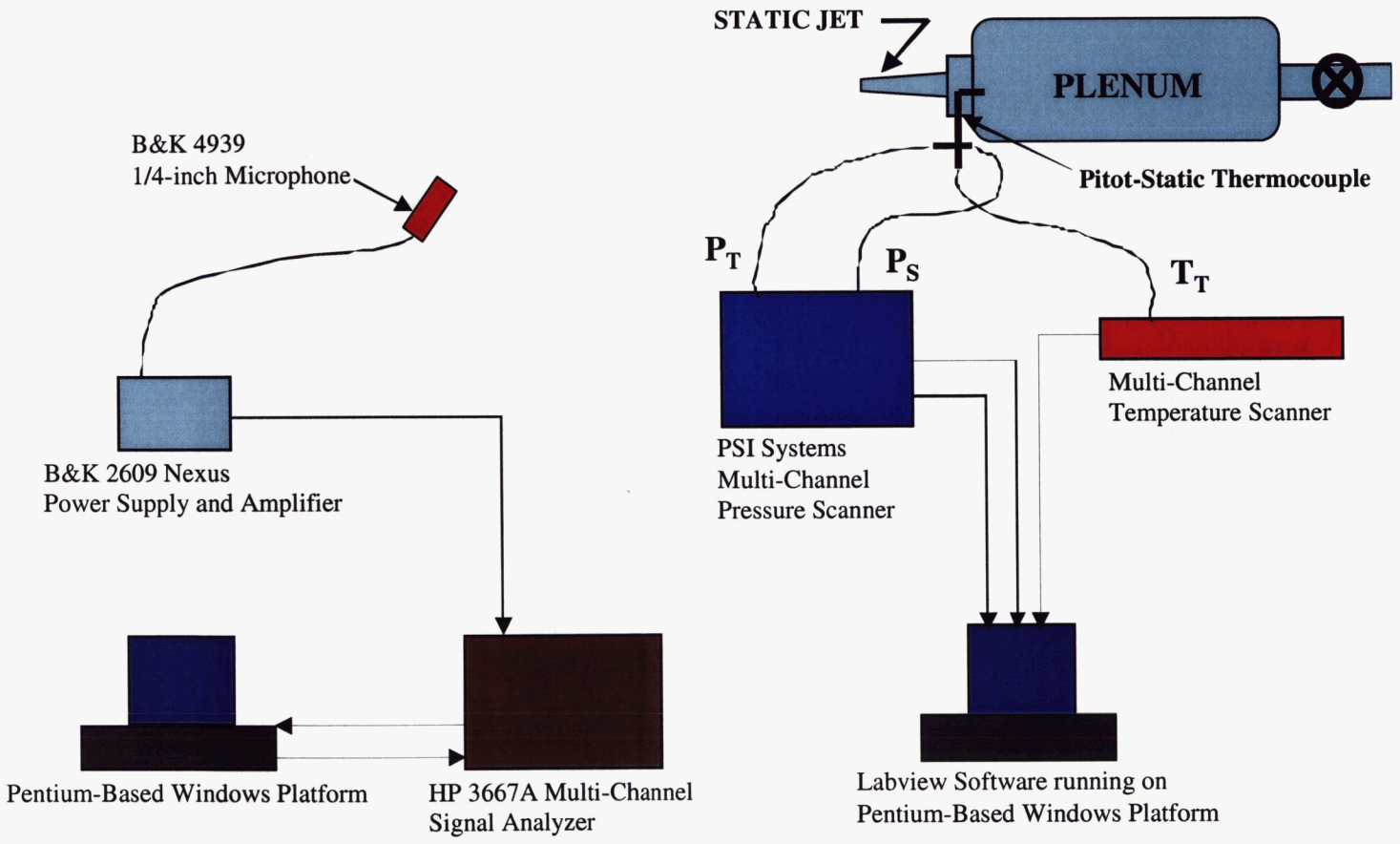

Figure 4.4 Data acquisition paths for flow and acoustic measurements.

The FFT analysis was performed with a frequency span of 0 – 102.4 Hz with a bandwidth of 32 Hz. Except where noted, 64 averages were used when sampling the microphone signals. Frequency domain data were saved for each run on the computer's hard drive in HP file format. These files were converted to ASCII text format and processed to quantify the sound pressure levels.

Pressure and temperature data were acquired using the Labview software tool running on a Windows 98 platform. Data from the pitot-static thermocouple were sampled and averaged to obtain jet velocity and mass flow data.

5.0 A Note About How Data Will Be Presented in This Report

Microphone Corrections

The data presented in this report will consist primarily of acoustic sound pressure levels and integrated sound pressure levels (overall sound pressure levels, 1/3-octave sound pressure levels). All acoustic data were acquired in narrow-band. All overall sound pressure levels (OASPL) and 1/3-octave data presented in this report were computed from the narrow-band data. The microphone data was calibrated before each test run with a 1000 Hz tone at 94 dB using a B&K 4231 sound level calibrator. A Free-field, pressure response and grid correction was applied to the raw, calibrated microphone data. Furthermore, all acoustic data was corrected for a specific distance and atmospheric absorption. Furthermore, the OASPL data was normalized with respect to density, temperature, and jet exhaust area. Details of all of these microphone corrections are supplied in Appendix B.

Calculation of jet exit velocity

The fully-expanded jet velocity was computed from using the isentropic flow equations and thus assumed no total pressure loss through the nozzle. Measuring the total pressure and total temperature and with the knowledge that the jet expands to match the ambient static pressure, the fully expanded jet velocity was computed as follows:

1) The fully expanded Mach number was computed from the isentropic pressure relation –

$$\frac{P_T}{P_s} = \left[1 + \frac{\gamma - 1}{2} M_j^2\right]^{\frac{\gamma}{\gamma - 1}} \qquad (1)$$

2) The jet velocity was computed from the definition of Mach number and the isentropic temperature relation –

$$M_j = \frac{U_j}{\sqrt{\gamma R T_s}} \qquad (2)$$

$$\frac{T_T}{T_s} = 1 + \frac{\gamma - 1}{2} M_j^2 \qquad (3)$$

Calculation of nozzle mass flow

The mass flow was determined by assuming a uniform flow profile across the circular portion of the upstream duct where total and static pressure and total temperature were measured. From these quantities, the velocity can be calculated using equations 1 through 3, except now the velocity is the local velocity, U, at the probe location. By invoking continuity (assuming the geometric area was equal to the flow area, i.e., no boundary layer), the mass flow through the nozzle was calculated as follows:

$$m = \frac{P_s}{RT_s} AU \qquad (4)$$

The corrected mass flow was computed following typical jet engine convention, namely:

$$m_{corr} = \frac{m\sqrt{\frac{T_T}{519\ \mathrm{R}}}}{\frac{P_T}{14.69\ \mathrm{psia}}} \qquad (5)$$

6.0 Farfield Acoustic Results

Farfield noise results of the DE nozzle are presented in this section. Results from a baseline round nozzle are presented alongside the DE nozzle for comparison.

Jet Noise Comparison – Round vs. Distributed Exhaust Nozzle Data

Data for both the round nozzle and the DE nozzle were acquired at nozzle pressure ratios (NPR) from 1.007 to 3.191, covering both subsonic and supersonic (up to $M_j = 1.4$) flow regimes. The DE nozzle was tested in three azimuthal positions, $\Phi = 0^o$, 30^o, and 90^o as shown in Figure 6.1. Mass flow measurements were made for both nozzles. Figure 6.2 shows the corrected mass flow as a function of nozzle pressure ratio (NPR) for the round nozzle and for the DE nozzle. At higher NPR, the DE nozzle appears to flow some 3% lower than the round nozzle. There is approximately a 1% scatter in the DE nozzle mass flow data, which in general can be considered to be providing good agreement between the flow rates of the two nozzles.

Figure 6.3 shows narrowband spectra for the DE nozzle [$\Phi = 90^o$] and round nozzle for two selected NPRs corresponding to a subsonic and a supersonic condition. These conditions also were selected to match numerical results of the DE nozzle using a Reynolds Averaged Numerical Simulation [RANS] code that were performed for this study, discussed in Section 2.

For the subsonic jet case (Figure 6.3a, NPR = 1.52), it is clear that the DE nozzle has a different spectral noise characteristic relative to the round nozzle. Below approximately 4 kHz, the DE nozzle is 4 – 8 dB quieter than the round jet in the farfield. The frequency of peak amplitude is higher for the DE nozzle and indeed the DE nozzle noise level is higher above about10 kHz. This corresponds to a Strouhal Number (St) of 1.6 based on equivalent diameter. The peak amplitude of the DE nozzle is lower than that of the round nozzle. As expected, the DE nozzle shifts noise from lower frequencies to a higher frequency region relative to an equivalent round nozzle.

For the supersonic jet case (Figure 6.3b, NPR = 2.40), one clearly sees the screech phenomenon and shock associated noise in the round noise spectrum. The large tone near 5 kHz (St = 0.8)

a) 1.60-inch diameter convergent round nozzle

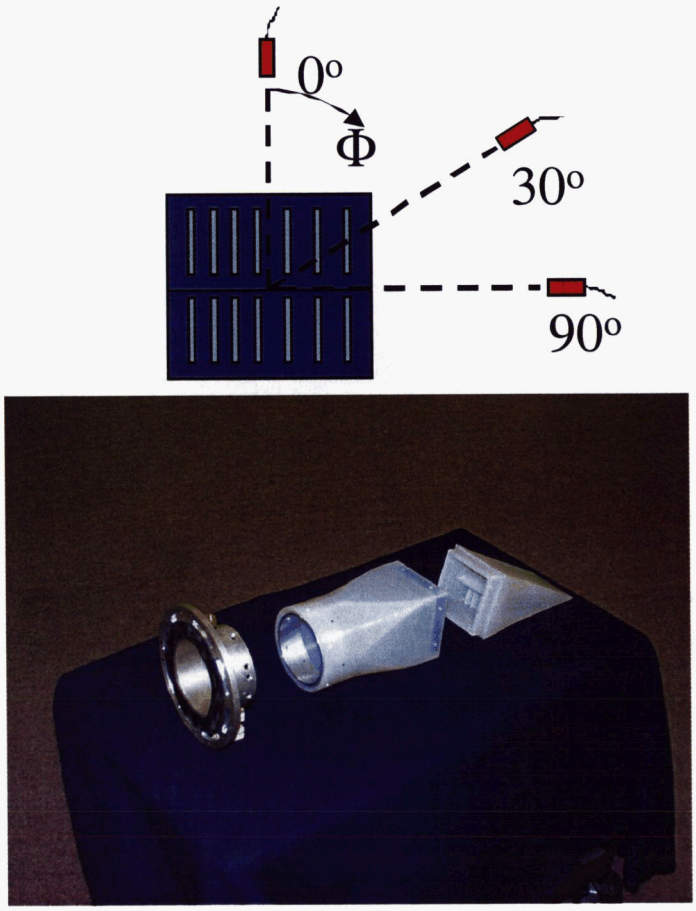

b) Exploded view of DE nozzle and azimuthal mic locations

Figure 6.1 a) Baseline round nozzle b) DE nozzle and orientation of azimuthal microphone positions.

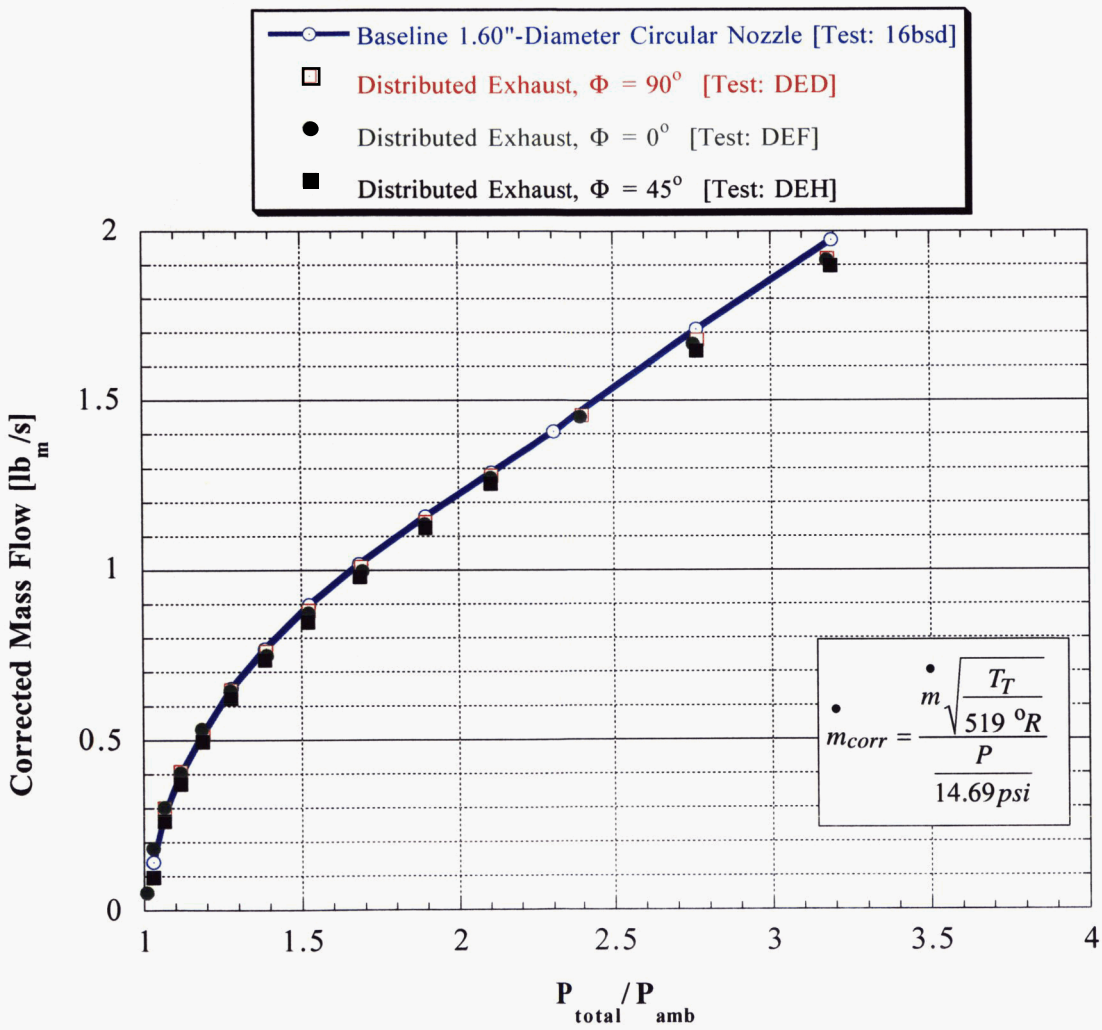

Figure 6.2 Corrected mass flow of DE nozzle and baseline round nozzle at various nozzle operating pressures.

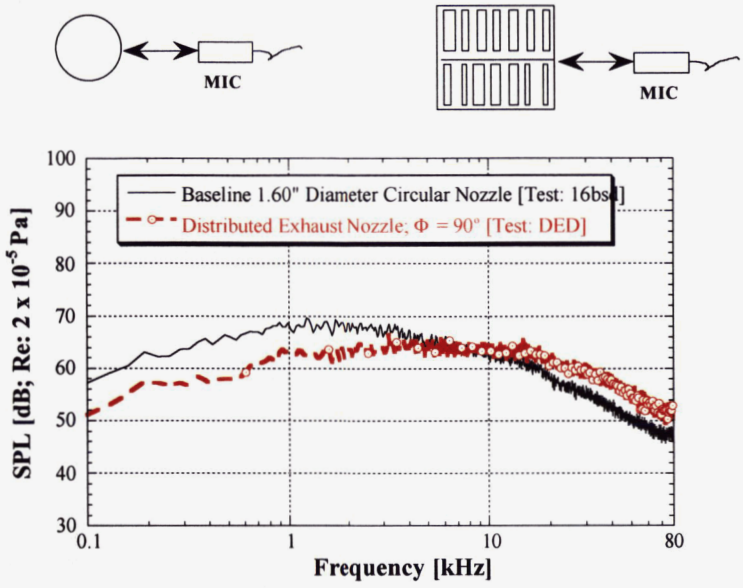

a) NPR = 1.52; V_j = 830 ft/s; Corrected mass flow = 0.881 lb_m/s

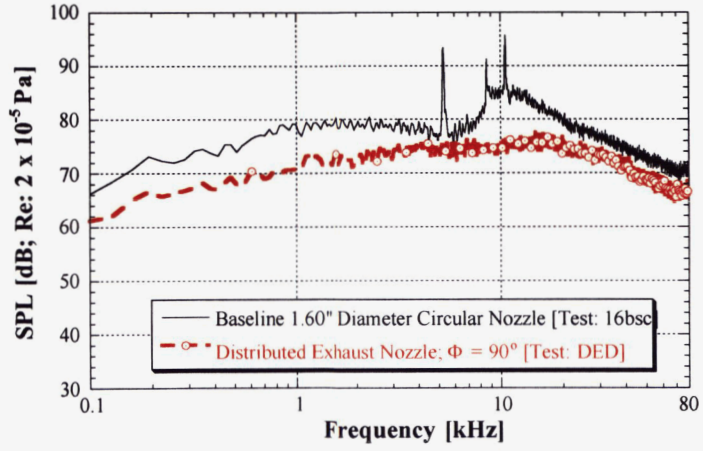

b) NPR = 2.40; V_j = 1157 ft/s; Corrected mass flow = 1.457 lb_m/s

Figure 6.3 Farfield noise comparison between DE and round nozzle[$\phi = 90^\circ$; $\theta = 90^\circ$; 64 avgs.; $\Delta f = 32$ Hz; SPL adjusted for R=12 ft, microphone grid and atmospheric absorption].

and two other tones are screech related and the increased broadband region beyond the first tone is the shock-associated broadband jet noise. The DE nozzle spectrum is distinctly different. It clearly does not show any screech or significant shock-associated broadband noise. The DE nozzle noise level is considerably lower than that of the round nozzle across the entire frequency range. It appears that the jet mixing noise has decreased across the entire spectrum by as much as 8 dB; the screech is non-existent, and the shock-associated noise has also reduced by as much as 12 dB.

Figures 6.4 and 6.5 show a comparison of narrowband spectra for all polar angles at NPR = 1.52 and 2.40, respectively. The trends discussed above are consistent for all microphone angles. For the subsonic case (Figure 6.4), note that at the lower polar angles, the DE nozzle exhibits a "flatter" spectral noise shape compared with the round nozzle. It is not as evident at the higher polar angles. Another feature of the DE nozzle spectra is the apparent shift of the peak levels from lower to higher frequencies as compared to the round nozzle. In this case, the shift is approximately 10 kHz. At the supersonic exhaust velocity (Figure 6.5), the DE nozzle shows significant noise reduction above 8 kHz at the forward arc angles (100, 110, and 120 degrees).

Figure 6.6 shows farfield spectra for the DE nozzle as a function of polar angle for the round nozzle and the DE nozzle at NPR = 1.52. Figure 6.7 shows similar data for NPR = 2.40. It is seen in these plots that the jet mixing noise is the highest at the smallest polar angle. Also at the supersonic condition, the screech is absent at all measurement angles for the DE nozzle. Similarly, the broadband shock-associated noise is significantly reduced at all angles.

The noise character of the DE nozzle in the azimuthal plane was examined by rotating the nozzle such that the farfield microphones were positioned at $\Phi = 0^o$, 30^o, and 90^o (see Figure 6.1). Spectra as a function of the azimuthal angle are shown in Figure 6.8a and 6.8b for NPR = 1.52 and 2.40, respectively, at a polar angle of 90^o. There is clearly a dependence on azimuthal angle for the DE nozzle. The noise measured at a $\Phi = 0^o$ appears to be higher in amplitude than the round nozzle in a frequency range of 800 – 3000 Hz ($St_{D\text{-equivalent}} = 0.13 - 0.48$). A similar trend can be seen in the supersonic jet data. It is possible that fluid shielding and/or turbulence scattering

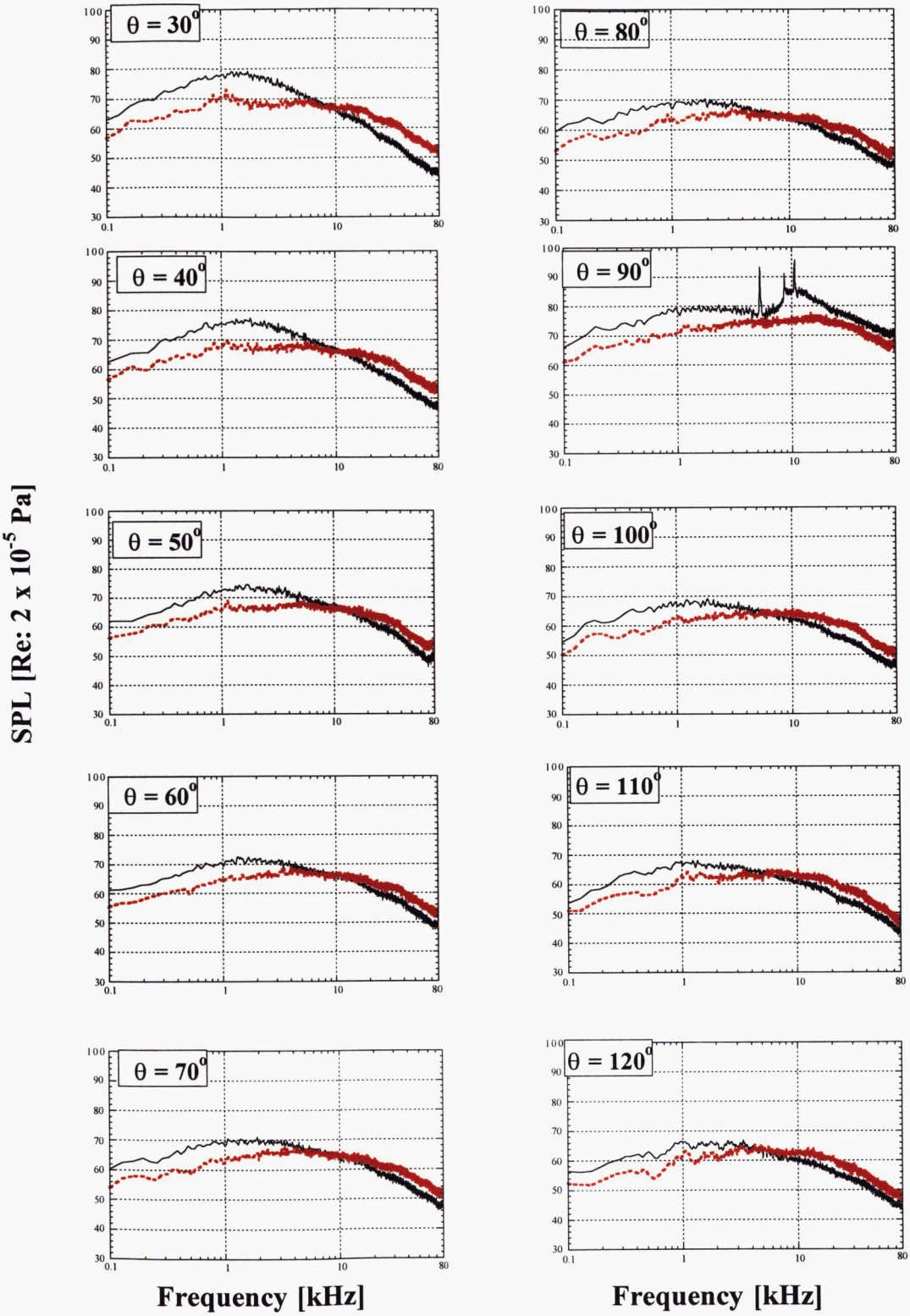

Figure 6.4. Comparison of farfield spectra; $\phi = 90^{o}$; R = 12 ft; 64 avgs.; 0-102.4 kHz; Δf = 32 Hz; T_j/T_{amb} = 0.975; NPR = 1.52; Uj = 830 ft/s; corrected mass flow = 0.881 lbm/s.
——— Baseline 1.596-inch Circular Nozzle - - - - - Distributed Exhaust Nozzle

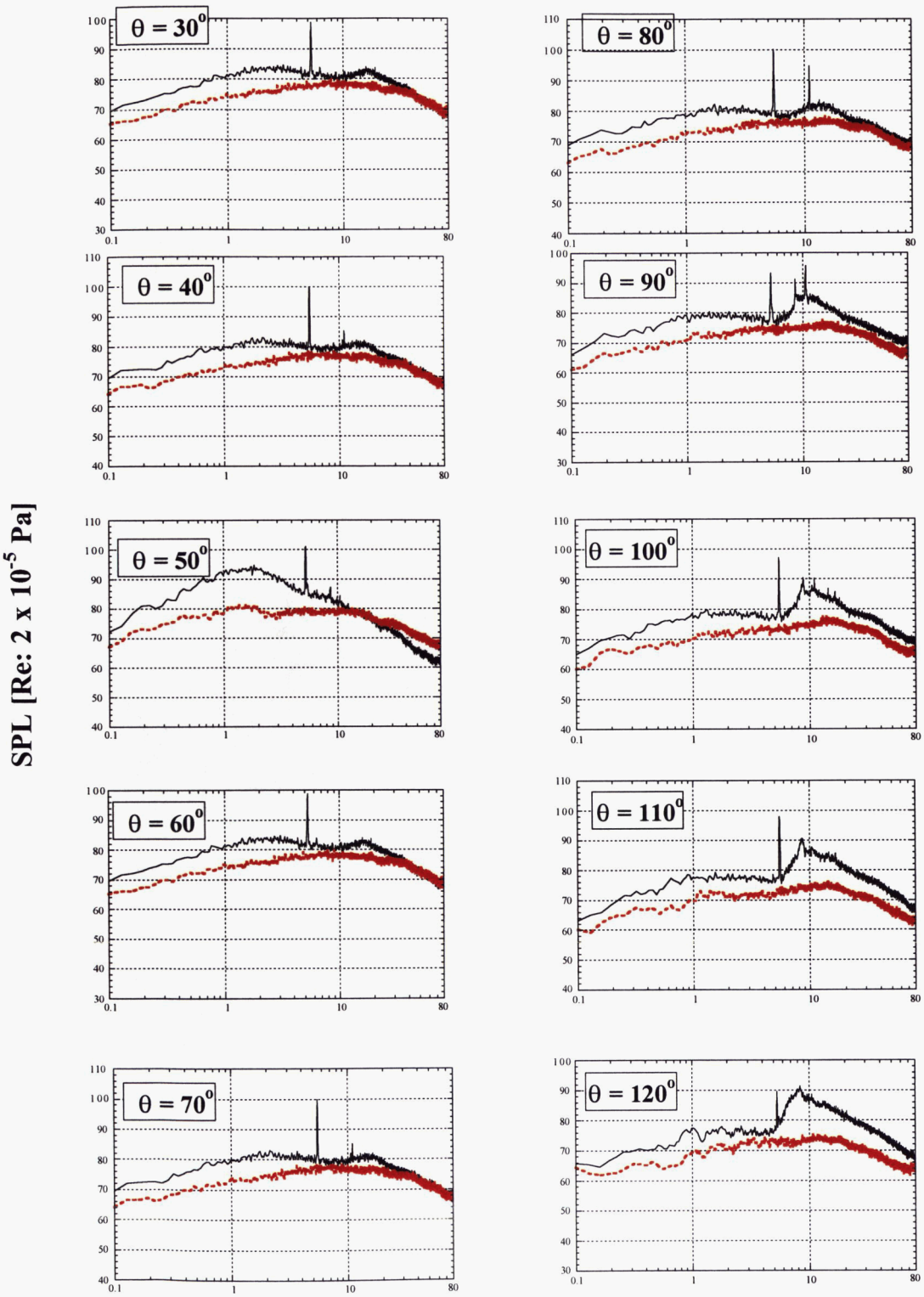

Figure 6.5 Comparison of farfield spectra; $\phi = 90^{o}$; R = 12 ft; 64 avgs.; 0-102.4 kHz; Δf = 32 Hz; T_j/T_{amb} = 0.975; NPR = 2.4; Uj = 1159 ft/s; corrected mass flow = 1.457 lbm/s.
——— Baseline 1.596-inch Circular Nozzle - - - - - Distributed Exhaust Nozzle

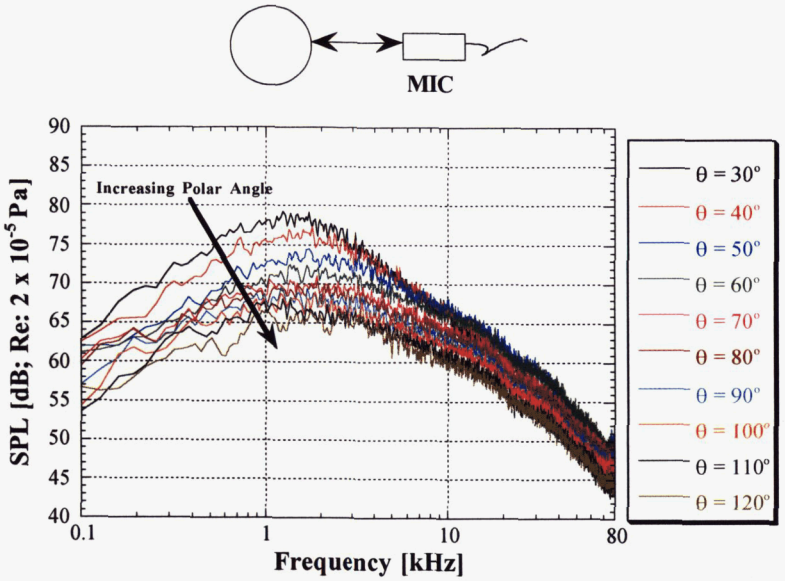

a) NPR = 1.52; V_j = 830 ft/s; ROUND Nozzle

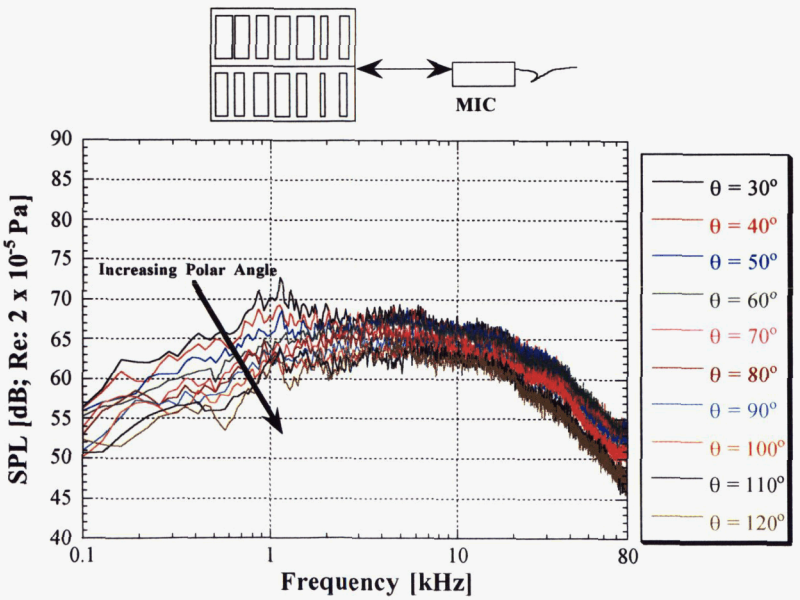

b) NPR = 1.52; V_j = 830 ft/s; DE Nozzle

Figure 6.6 Polar angle trends for farfield noise a) Round Nozzle, b) DE nozzle [$\theta = 90^{\circ}$; 64 avgs.; $\Delta f = 32$ Hz; SPL adjusted for R=12 ft, microphone grid and atmospheric absorption].

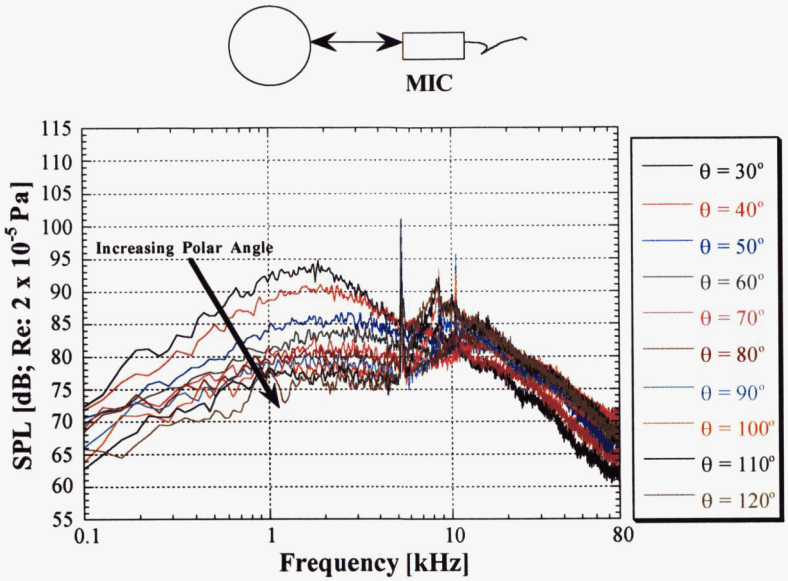

a) NPR = 2.40; V_j = 1157 ft/s; ROUND Nozzle

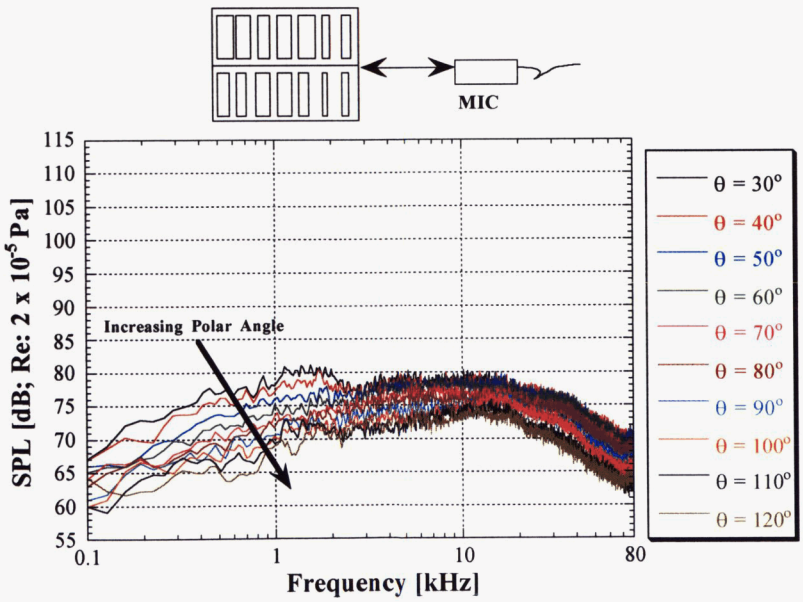

b) NPR = 2.40; V_j = 1157 ft/s; DE Nozzle

Figure 6.7 Polar angle trends for farfield noise a) Round Nozzle, b) DE nozzle [$\theta = 90^o$; 64 avgs.; $\Delta f = 32$ Hz; SPL adjusted for R=12 ft, microphone grid and atmospheric absorption].

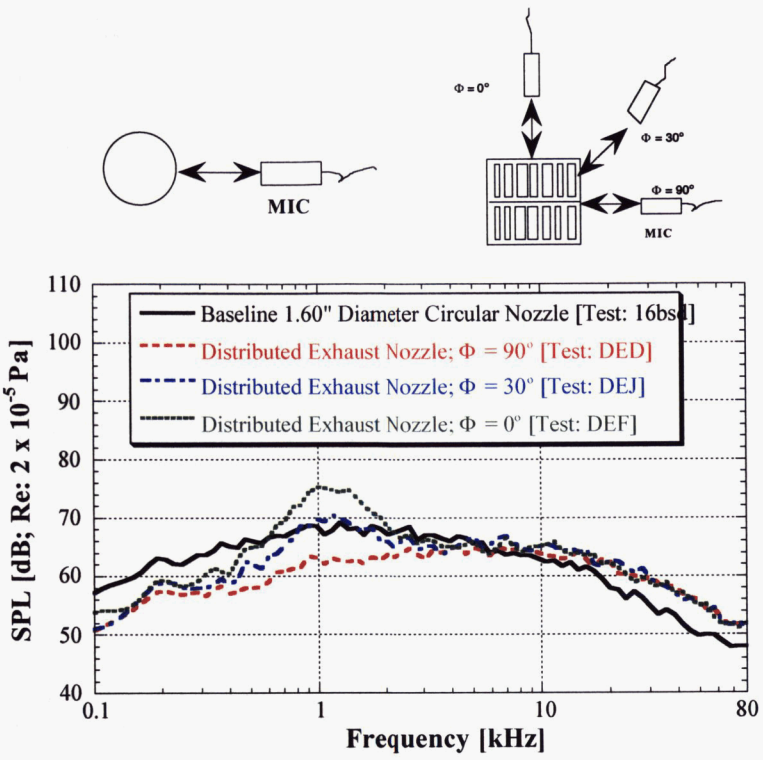

a) NPR = 1.52; V_j = 830 ft/s

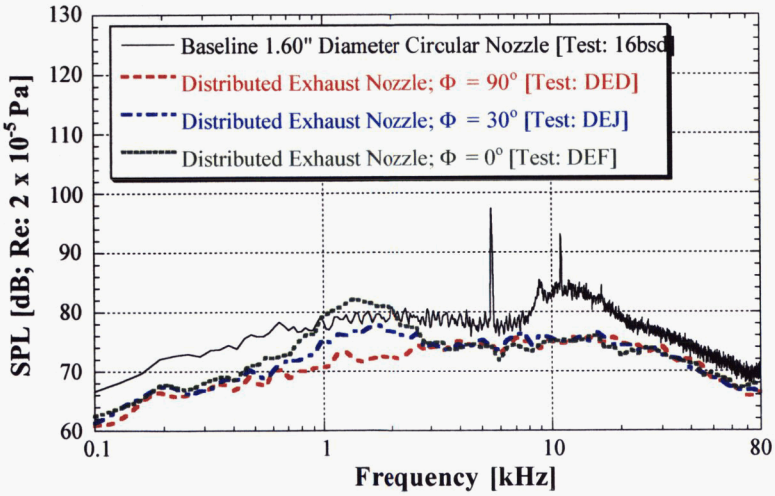

b) NPR = 2.40; V_j = 1157 ft/s

Figure 6.8 Azimuthal variation in farfield noise spectra [$\theta = 90^o$; 64 avgs.; $\Delta f = 32$ Hz; SPL adjusted for R=12 ft, microphone grid and atmospheric absorption].

could be the reason for this behavior. This will be discussed in some detail in the next section. Figures 6.9 and 6.10 show azimuthal comparisons at other polar angles for a NPR of 1.52 and 2.40, respectively. The trend seen in Figure 6.8 seems more pronounced at higher polar angles.

Overall Sound Pressure Level Data – Farfield Directivity

Figures 6.11 a-d show farfield OASPLs for polar angles from 30 to 120 degrees. Azimuthal angles of 0, 30, and 90 degrees for the DE nozzle are shown along with the round nozzle data for comparison. For subsonic jet velocities, the round nozzle exhibits the well-established high noise lobe near the lower polar angles, (Ahuja/Bushell[3]) sloping to lower OASPLs at the higher polar angles. At lower subsonic jet velocities (U_j = 539 ft/s, Figure 6.11a), the DE nozzle shows less directivity than the round nozzle. Also note the distinct difference in OASPL between the different azimuthal angles of the DE nozzle. The DE nozzle is shown to have higher OASPL levels at most of the polar angles relative to the round nozzle. The levels progressively decrease as the azimuthal angle, Φ, increases from 0 to 90 degrees. At higher subsonic jet velocities, the directivity of the DE nozzle is more similar to the round nozzle [U_j = 828 ft/s, Figure 6.11b) while there is not as much spread with azimuthal angle as compared to the lower subsonic case.

At supersonic jet velocities, the DE nozzle shows reduced OASPL's compared to the round nozzle at all polar angles (Figure 6.11c-d). This is due to the fact that the DE nozzle does not exhibit screech and has little contribution from shock-associated broadband noise like the round jet. Also, it is interesting to note that the azimuthal dependence for the DE nozzle is not as strong as in the subsonic case.

A more detailed presentation of the farfield directivity of the DE nozzle appears in Figure 6.12. OASPL directivities are shown for a range of jet velocities for the round nozzle and three azimuthal configurations of the DE nozzle. Jet velocities ranging from 434 ft/s to 1309 ft/s are shown. It appears from these data that the DE nozzle operating at lower subsonic jet velocities exhibits a more symmetrical farfield noise directivity (as seen by the "flatness" of the curves below 700 ft/s). At a jet velocity of 828 ft/s, the round nozzle shows approximately a 9 – 10 dB change between polar angles of 30 and 120 degrees. At an equivalent velocity for the DE nozzle, a 2.5 – 5 dB change is observed.

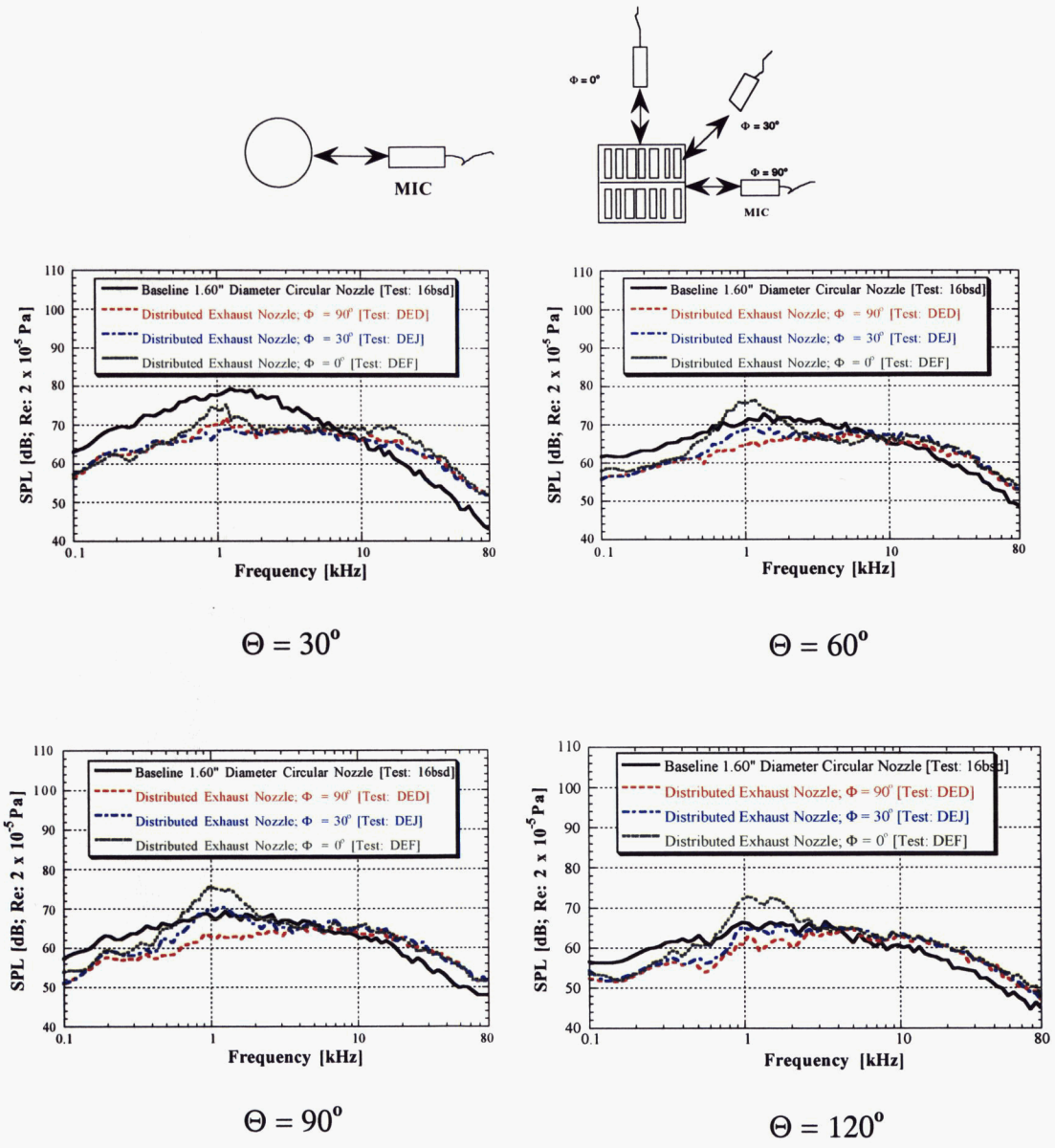

Figure 6.9 Effect of azimuthal angle on DE nozzle at selected polar angles for NPR = 1.52 [$\theta=90^{o}$; 64 avgs.; Δf = 32 Hz]

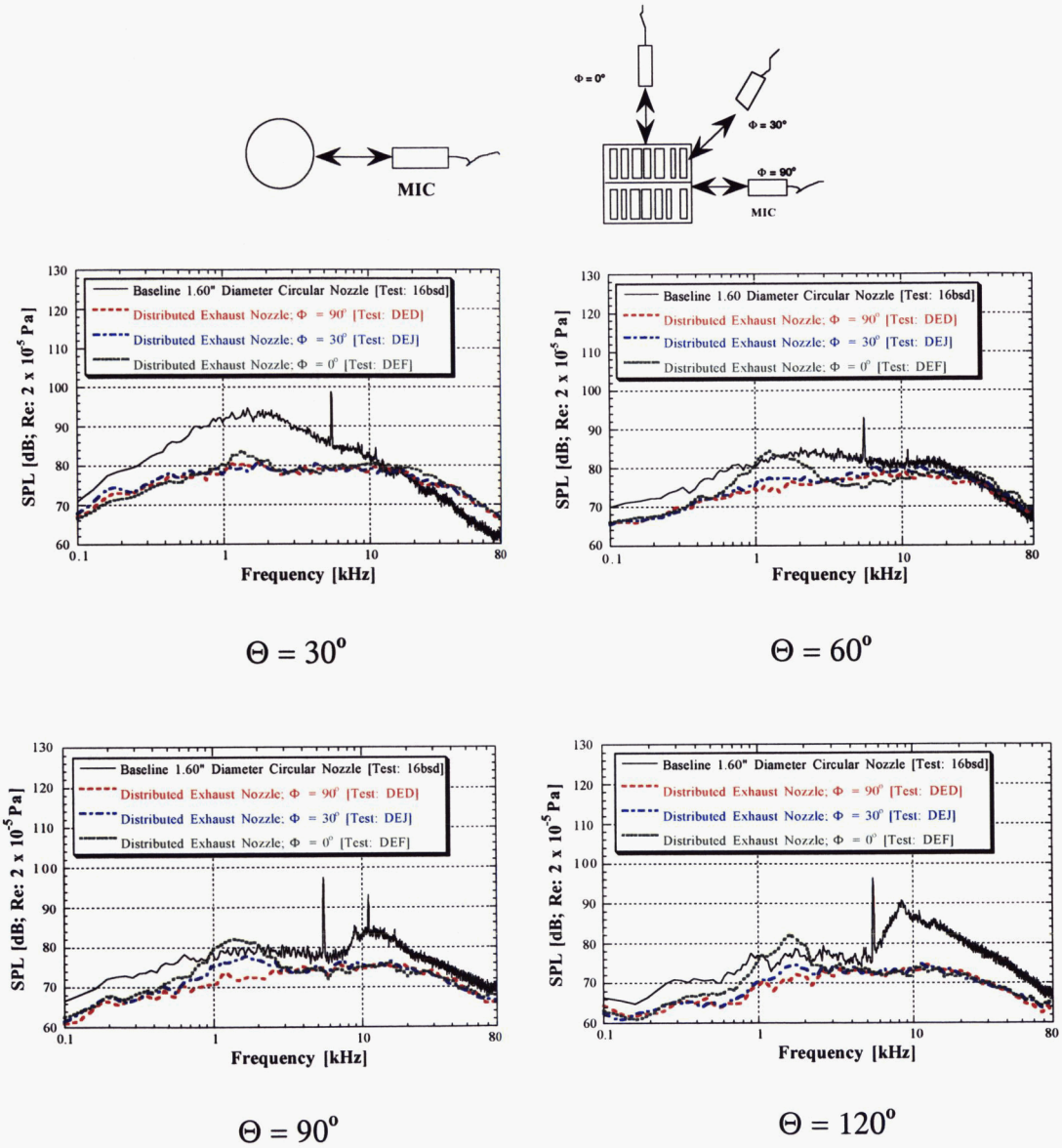

Figure 6.10 Effect of azimuthal angle on DE nozzle at selected polar angles for NPR = 2.40 [$\theta=90^{o}$; 64 avgs.; $\Delta f = 32$ Hz]

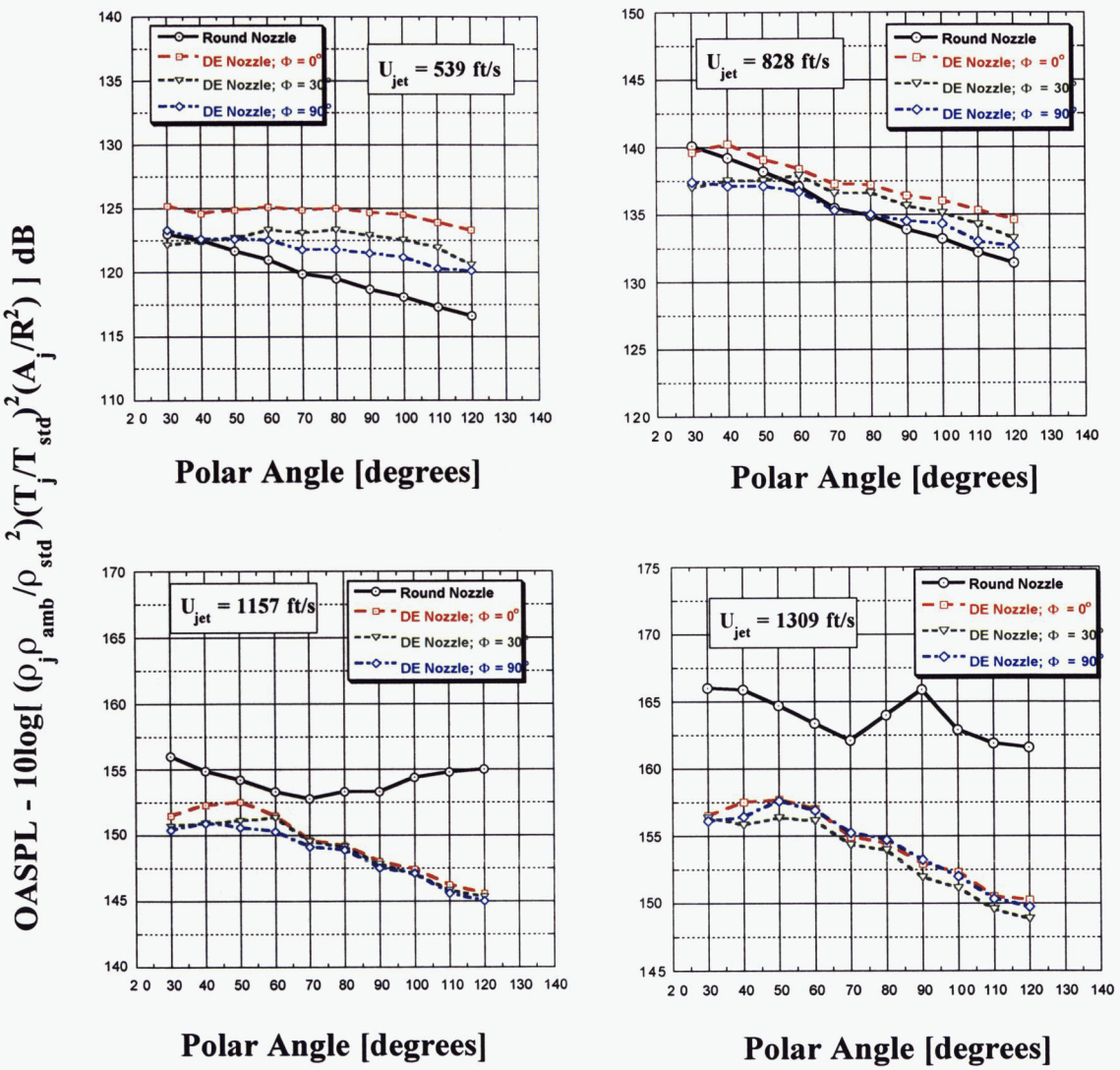

Figure 6.11 Comparison of OASPL directivity; R = 12 ft; 64 avgs.; 0-102.4 kHz; Δf = 32 Hz; T_j/T_{amb} = 0.975.

Round Nozzle — DE Nozzle $\Phi = 0^\circ$ — DE Nozzle $\Phi = 30^\circ$ — DE Nozzle $\Phi = 90^\circ$

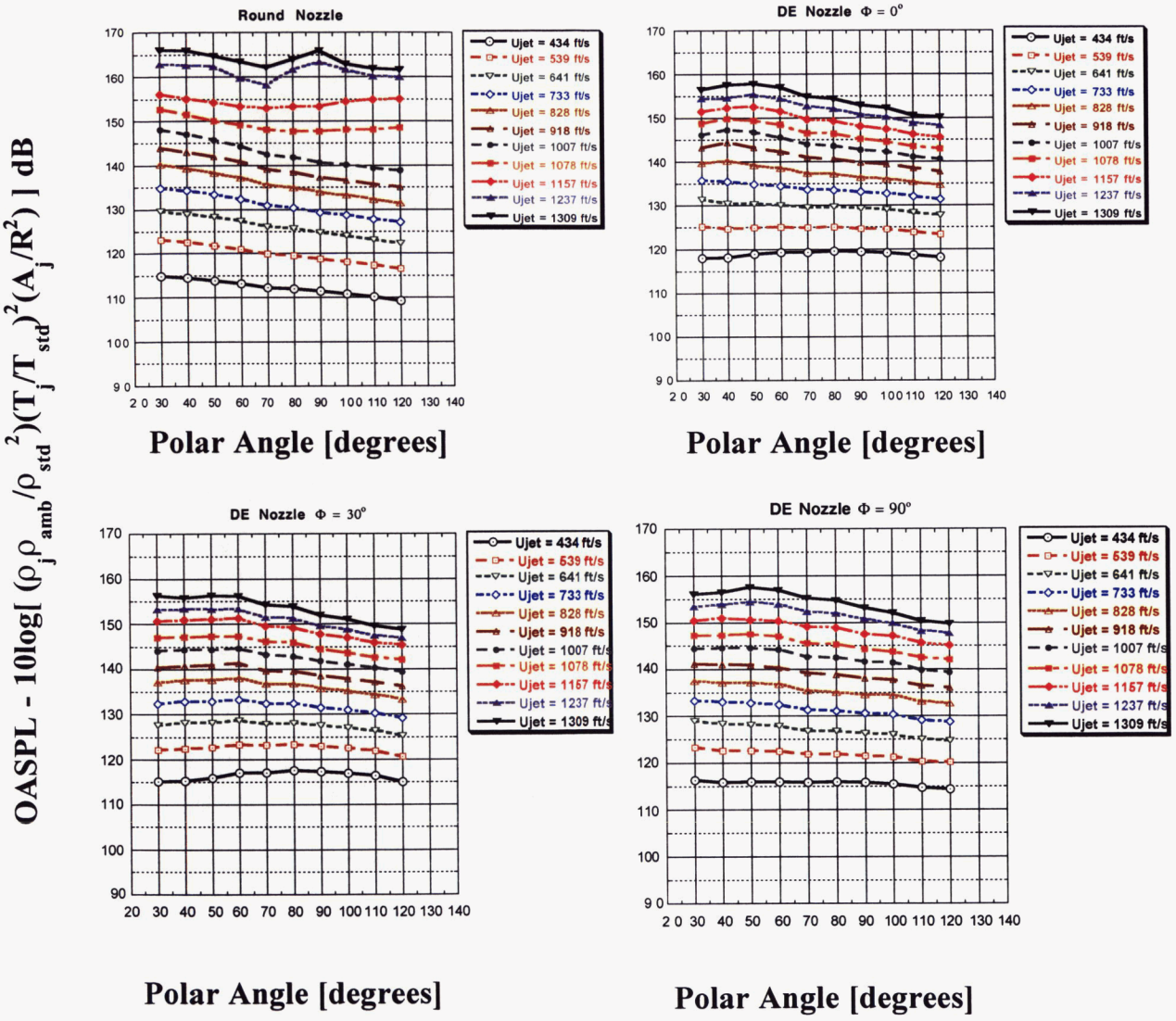

Figure 6.12 Comparison of OASPL directivity versus jet velocity; R = 12 ft; 64 avgs.; Δf = 32 Hz; T_j/T_{amb} = 0.975.

Velocity Dependence of Jet Noise

The well-known Lighthill Analogy for farfield jet noise (Lighthill[4,5]) postulates that the jet noise intensity at a distance R is proportional to the jet velocity. This is given by (Ahuja-Bushell[3]):

$$I \propto \frac{\rho_m^2 U_j^8 D^2}{\rho_o a_o^5 R^2}\left[1 - M_c \cos\theta\right]^{-5} \qquad (6)$$

where D is the typical dimension in the flow, M_c the eddy convection Mach number (= $0.65M_j$) and ρ_m is the density of the mixing region. Figures 6.13 through 6.16 compare the OASPL at several polar angles (30, 60, 90, and 120 degrees, respectively) as a function of jet velocity for the round and DE nozzle. An indication of the predicted velocity (see equation 6) dependence is shown on each plot with a line possessing a U_j^8 slope . For subsonic velocities above 400 ft/s, the round jet follows the U_j^8 dependence reasonably well. The DE nozzle seems to have a shallower slope for subsonic velocities at smaller polar angles (see Figure 6.13) than at larger angles. Indeed, at a polar angle of 90 degrees (see Figure 6.15), a linear curve fit suggests that the data for the DE nozzle between jet velocities of 300 and 800 ft/s follows a $U_j^{6.3}$ relationship more closely. Since the theory does not account for screech or shock-associated noise, the U_j^8 dependence does not hold near and above sonic jet velocities for either the round or DE nozzles. The significantly reduced noise of the DE nozzle at supersonic jet velocities compared to the round nozzle (up to 10 dB) can be seen at all azimuthal angles.

Finally, as general comparison of how the DE nozzle compares with a large body of jet noise data, Figure 6.17 shows a compilation of OASPL as a function of jet velocity taken from Ahuja-Bushell. On this plot are jet noise data gathered from a range of jet engines as well as conical air jets from laboratory experiments at the peak noise polar angle. For the present data, 30 degree polar angle data was used, where the other data was compiled from spectra at a polar angle of 20 degrees. Furthermore, the convection Mach number term is not included in this data. Superimposed on this plot are the present set of round nozzle jet data and selected DE nozzle data. All data on this plot are at the peak noise polar angle, which for the present data was at 30 degrees. The present subsonic round jet data agrees extremely well with the clean, round air jet data (see the D curve in Figure 6.17). The DE nozzle data follows the same trend. However, as

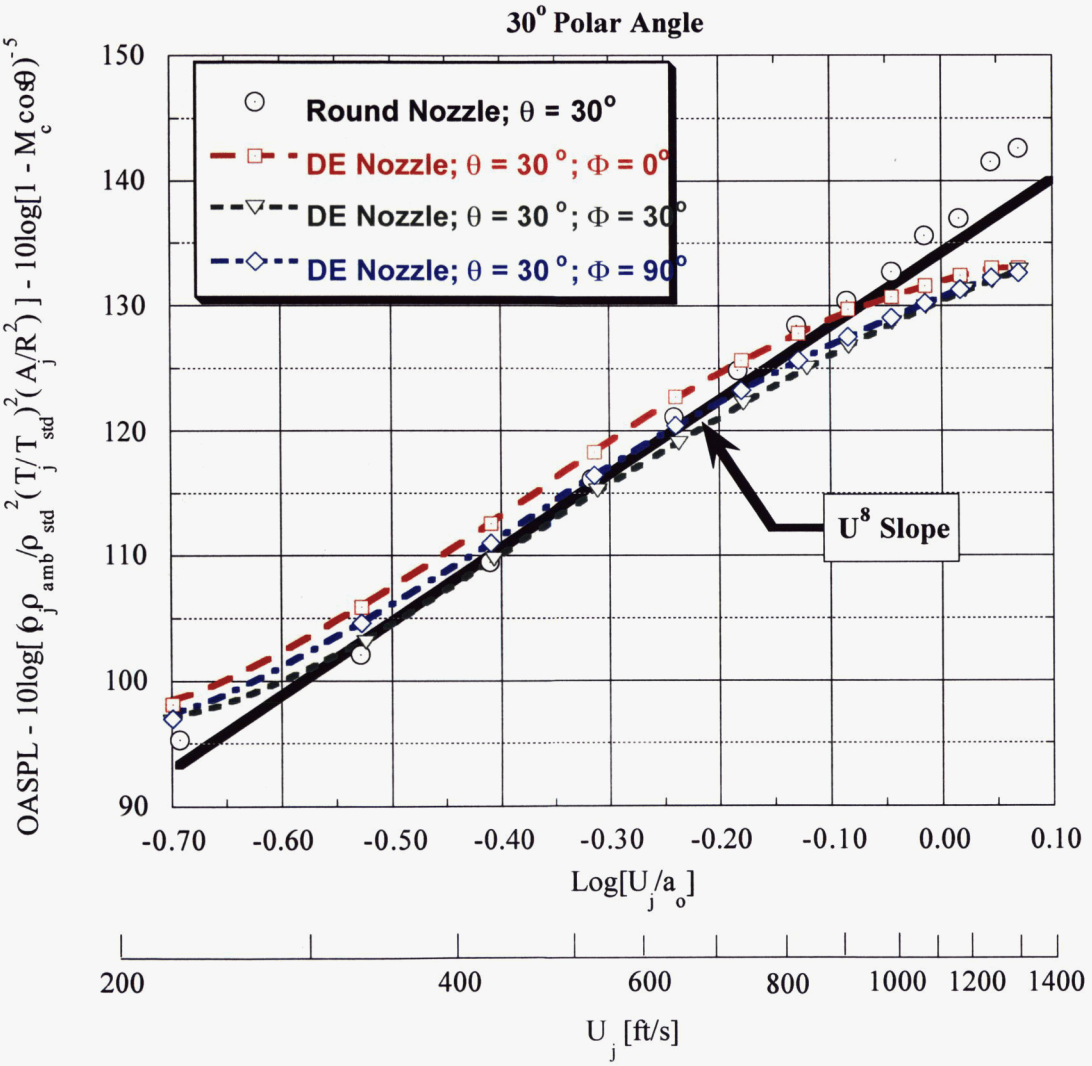

Figure 6.13 Velocity dependence of corrected OASPL for DE nozzle [θ=30°; 64 avgs.; SPL adjusted for R=12 ft and atmospheric absorption].

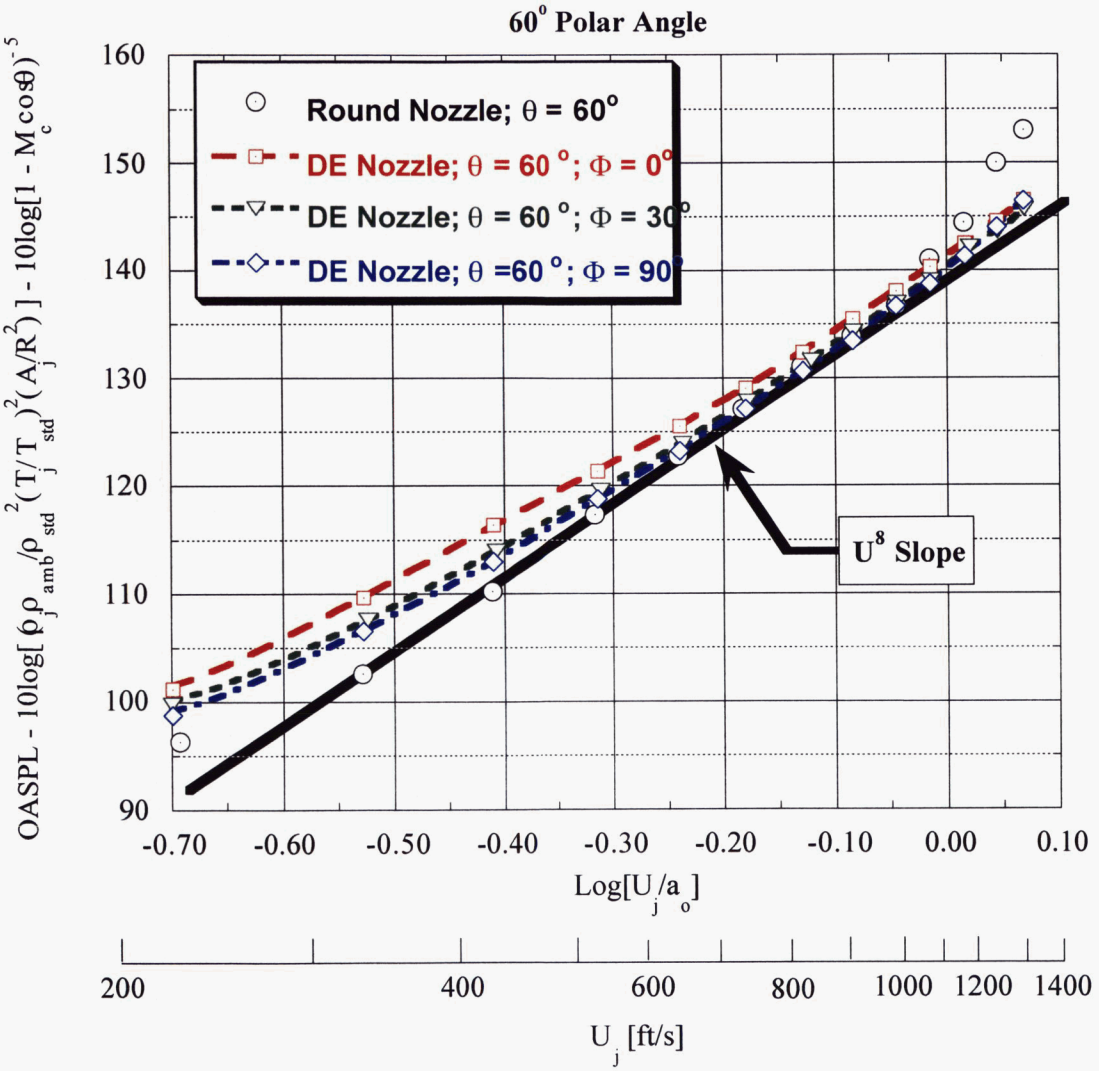

Figure 6.14 Velocity dependence of corrected OASPL for DE nozzle [θ=60°; 64 avgs.; SPL adjusted for R=12 ft and atmospheric absorption].

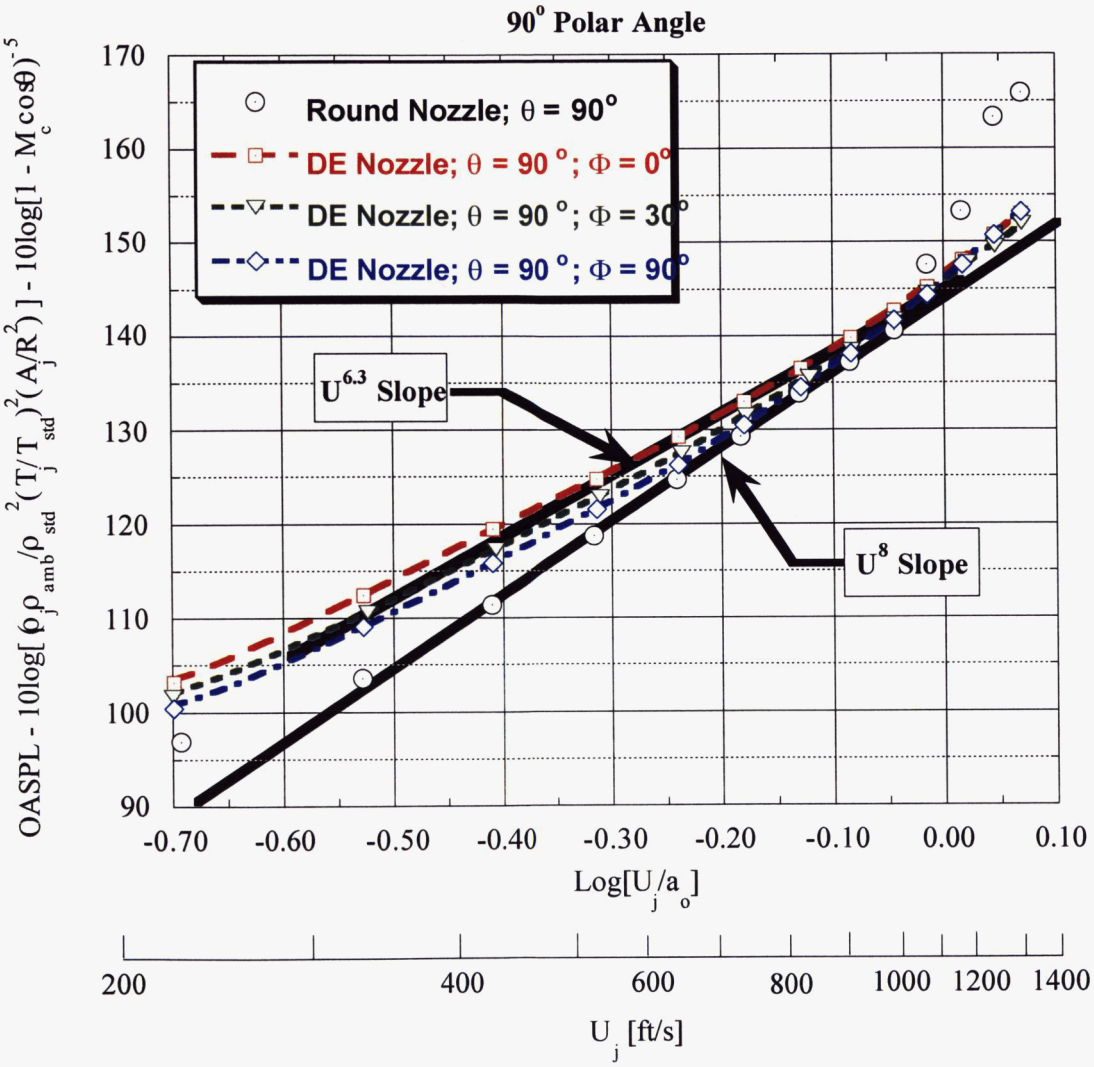

Figure 6.15 Velocity dependence of corrected OASPL for DE nozzle [θ=90°; 64 avgs.; SPL adjusted for R=12 ft and atmospheric absorption].

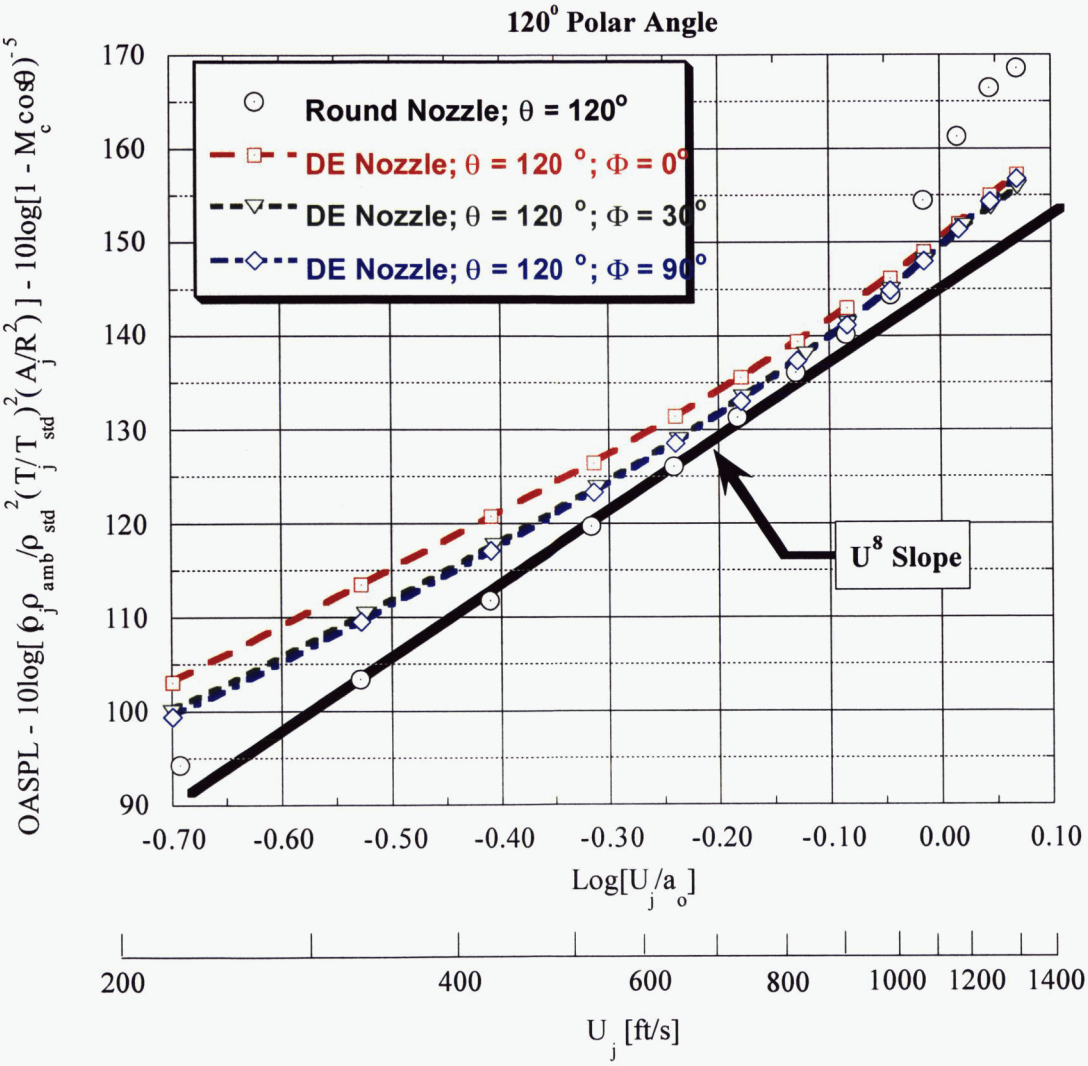

Figure 6.16 Velocity dependence of corrected OASPL for DE nozzle [θ=120°; 64 avgs.; SPL adjusted for R=12 ft and atmospheric absorption].

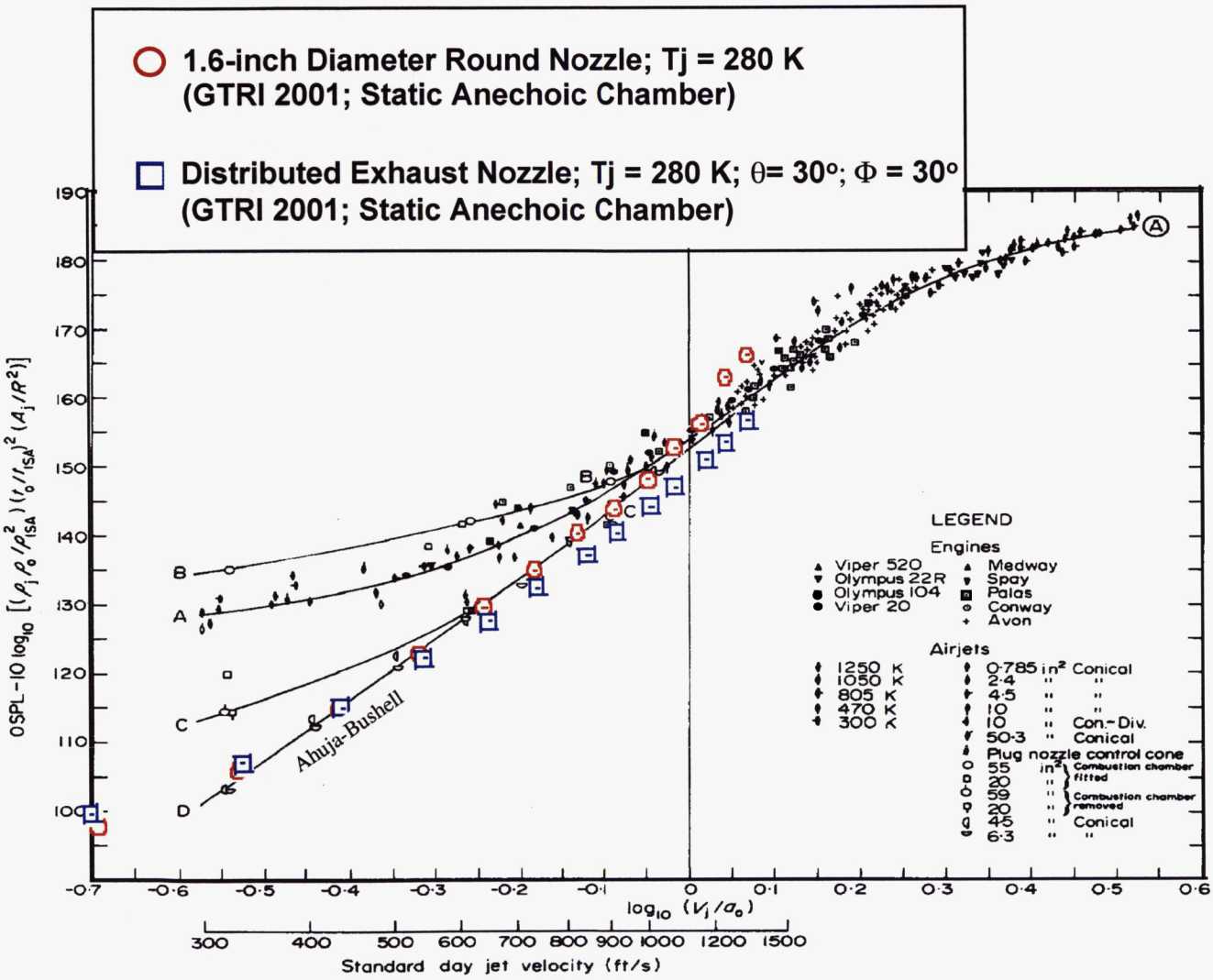

Figure 6.17 Comparison of present data with database of jet noise data from laboratory and engine tests; peak noise polar angle [ref. 3 - Ahuja and Bushell]

the jet velocities approach and exceed sonic velocities, the noise level is reduced relative to the round jet data.

Discussion

Several observations can be made from the preceding farfield noise results.

1. At subsonic jet velocities, the DE nozzle exhibits a "flatter" noise spectrum at lower polar angles than a equivalent area round nozzle (see Figure 6.4). Compared to an equivalent round nozzle, The DE nozzle appears to produce lower noise (as much as 4 – 8 dB) at lower frequencies. The DE nozzle produces higher noise beyond 8 – 9 kHz (St = 1.3 – 1.5).

2. At subsonic jet velocities, the peak spectral noise levels for the DE nozzle are shifted to higher frequencies compared to the round nozzle peak levels (see Figure 6.4).

3. The DE nozzle does not exhibit the screech phenomenon at supersonic jet velocities. The shock-associated broadband noise also appears to be insignificant resulting in significant noise reductions compared to the round nozzle across the spectrum at all polar angles (see Figure 6.5).

4. The DE nozzle exhibits azimuthal directivity, but only in a small frequency range, 800 – 3000 Hz (St = 0.13 – 0.48), see Figure 6.8. This effect is greater at subsonic rather than at supersonic velocities.

5. At low subsonic velocities, the DE nozzle shows a greater dependence on azimuthal angle than at higher subsonic and supersonic velocities (see Figure 6.11).

6. At low subsonic velocities, the DE nozzle shows a lesser dependence on polar angle than a round nozzle.

7. The DE nozzle exhibits the general velocity dependence on farfield jet noise as typical round nozzles at subsonic velocities, namely the U_j^8 relationship. However, at velocities less than 800 ft/s, the DE nozzle follows a $U_j^{6.3}$ relationship at polar angles above 30 degrees. It is not clear

why a $U_j^{6.3}$ relationship is obtained for the DE nozzle at lower velocities, whereas it is actually U_j^8 for the round jet. One could speculate that there may be some extraneous noise produced at the passages of the flow from the nozzle interior to the slot exit, resulting in a dipole type scaling of $U_j^{6.3}$. If this is the case, the noise reductions obtained from a DE nozzle compared to an equivalent round nozzle can be expected to be even higher.

The observed farfield noise character of the DE nozzle support at least two of the nozzle's intended design consequences, namely, the shifting of noise frequency content. By splitting the exhaust area into a number of smaller jets, much of the noise is produced at a higher frequencies compared to a single equivalent area round nozzle. Furthermore, coalescing of the suitably-spaced jets produces a lower velocity jet downstream, thus reducing noise in the lower frequency region. The increase in noise at the higher frequencies affects the OASPLs. Thus, at subsonic jet velocities, the overall sound radiated by the DE nozzle is between 1 to 5 dB higher than of an equivalent round nozzle. However, since the DE nozzle does not exhibit the jet screech phenomenon or the shock-associated broadband noise, the DE nozzle is significantly quieter than the round nozzle at supersonic jet velocities.

The observed dependence on azimuthal angle on the farfield jet noise of the DE nozzle is striking. Clearly, in a certain frequency range, the observer in the farfield can sense a difference in noise level depending upon the orientation of the DE nozzle (see Figure 6.8). A higher level is measured at an azimuthal angle of 0 degrees compared to 90 degrees. Some insight can be obtained from examining the smaller jet orientation of the DE nozzle as shown in Figure 6.1. In the 0 degree orientation, the observer sees all of the smaller jets expanding to the ambient pressure. The jets coalesce across the long side of the rectangular projection. At the 90 degree orientation, the observer only sees the outside jet sheet formed from the outer small jet. The noise from the inner jets are shielded. It is quite likely that this can account for the reduction observed noise at 90 degrees as opposed from 0 degrees.

It is also likely that the noise from the interior jets is being refracted (via Snell's Law) by the adjacent jet shear layers and thus projecting the noise to even lower polar angles along the jet

axis. To examine these hypotheses more closely, the DE nozzle was tested with only a selected number of the smaller jets allowed to flow. This is discussed in Section 8.0. Additional insight into the behavior of the unique interaction between the slanted exhaust jets can be obtained from examining some flow visualization of the DE nozzle. This is discussed in Section 7.0.

7.0 DE Nozzle Flow Visualization

The objective of the flow visualization was to discern qualitatively, the behavior of the individual slotted-jets, e.g., how far downstream from the exhaust plane of the nozzle do the jets merge. In addition, the flow visualization could provide qualitative validation of the numerical simulation.

Flow visualization of the DE nozzle was obtained using a high pressure flow seeder and PIV as described in section 4 of this report. Instantaneous velocities were measured at selected locations in the DE nozzle exhaust field. The high pressure plenum upstream of the nozzle was seeded with titanium-oxide particles to provide imagery for the PIV apparatus. In general, two viewing planes were examined: 1) the axial plane that is parallel to the streamwise direction at the mid-span location and 2) the cross plane that is parallel to the sloping plane of the DE nozzle at the slot-jet exit. Figure 7.1 shows these planes schematically.

The DE nozzle was operated at a nozzle pressure ratio (NPR) of 1.52, which corresponded to a numerical simulation condition of the present work. The fully-expanded isentropic velocity was approximately 830 ft/s. Figure 7.2 shows several PIV images of the instantaneous velocity field in the axial mid-span plane of the DE nozzle exhaust. Note that the flow tends to follow the slant of the nozzle. The flows on the top and bottom side merge and form a jet that is smaller in the y-direction than the projection of the slot height in the y-direction. Figure 7.3 shows another mid-span plane view of the velocity field discerned from PIV measurements alongside a numerical solution of the same plane showing mean Mach number contours. The general flowfield is similar between the PIV and the numerical results. However, the instantaneous nature of the PIV measurements show the presence of large scale instability (in the y-direction). This is more clearly seen in Figure 7.4, which shows the instantaneous velocity field at some point downstream. At approximately $x \sim 17$ inches from apex of the DE nozzle, a flapping instability is observed from two images that are some time, Δt, apart.

A closer view of the initial emergence of the individual jets can be seen in Figure 7.5. Imaging a plane parallel to the slope of the DE nozzle, the PIV measured instantaneous velocities less than a quarter of an inch from the surface. It is clear from the velocity vectors shown in Figure 7.5

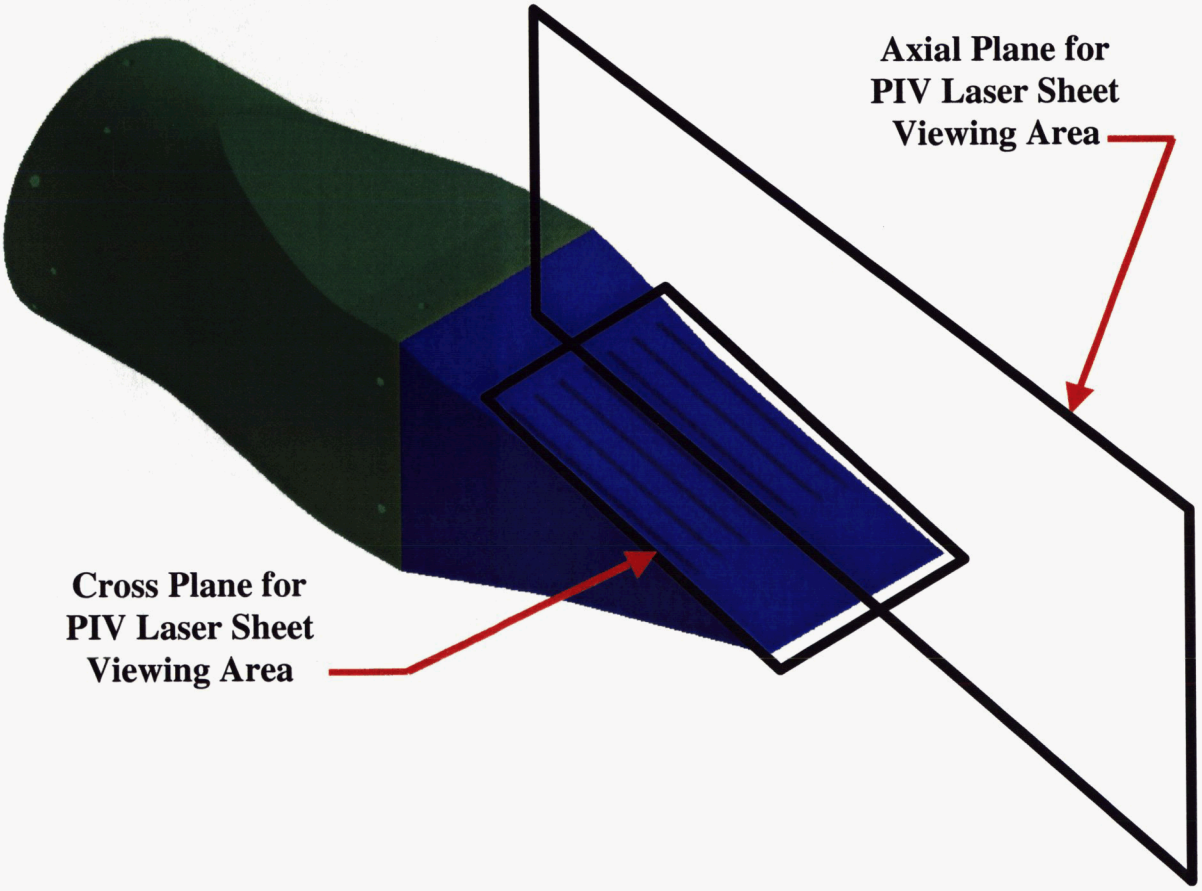

Figure 7.1 Viewing planes for PIV diagnostic imagery.

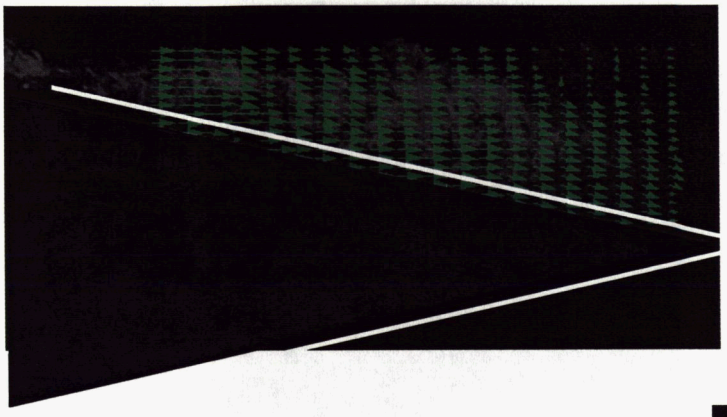

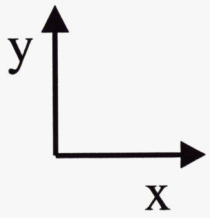

a) Velocity field on downward nozzle ramp

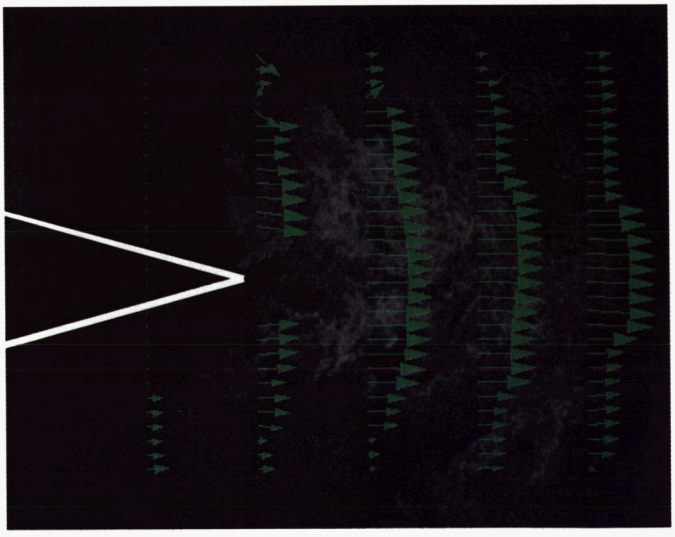

b) Velocity field just downstream of nozzle apex

Figure 7.2 Instantaneous velocity at mid-span plane [PIV results]

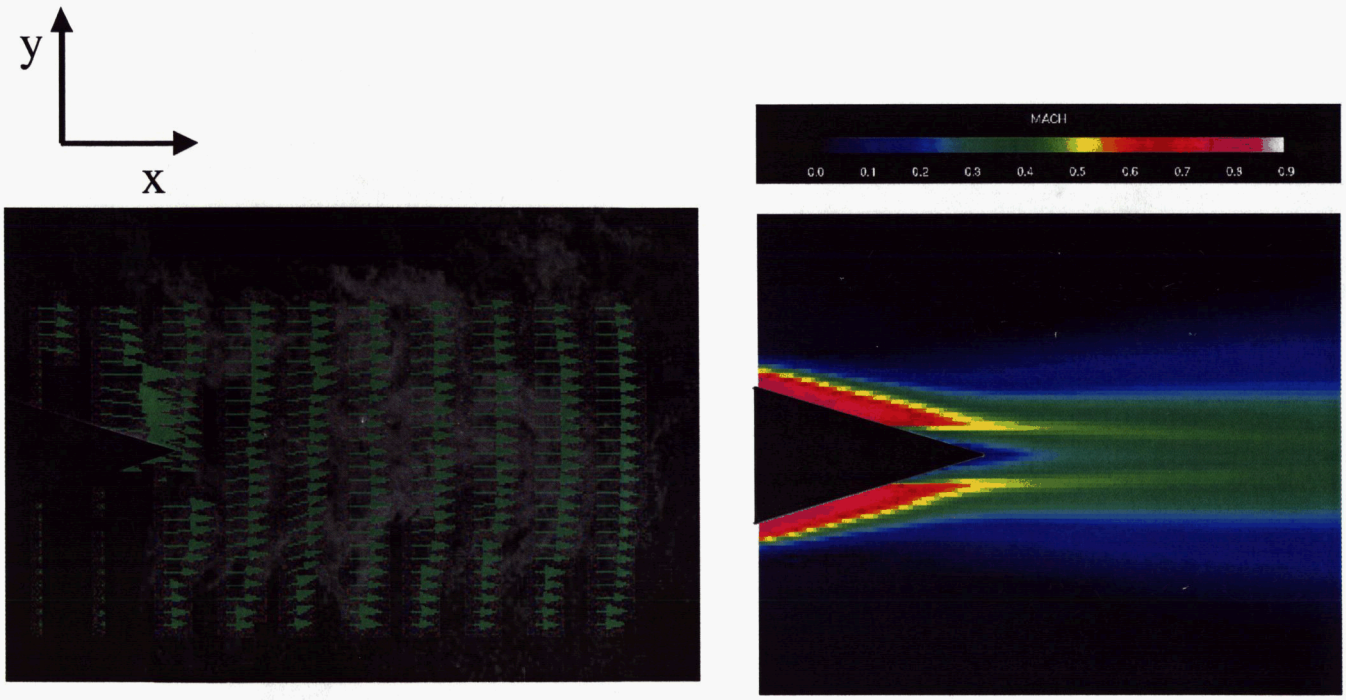

a) Instantaneous Velocity at Mid-Span plane [PIV results]

b) Mean Mach number at Mid-span plane [RANS solution]

Figure 7.3 Instantaneous velocity at mid-span plane comparison with mean Mach number numerical solution.

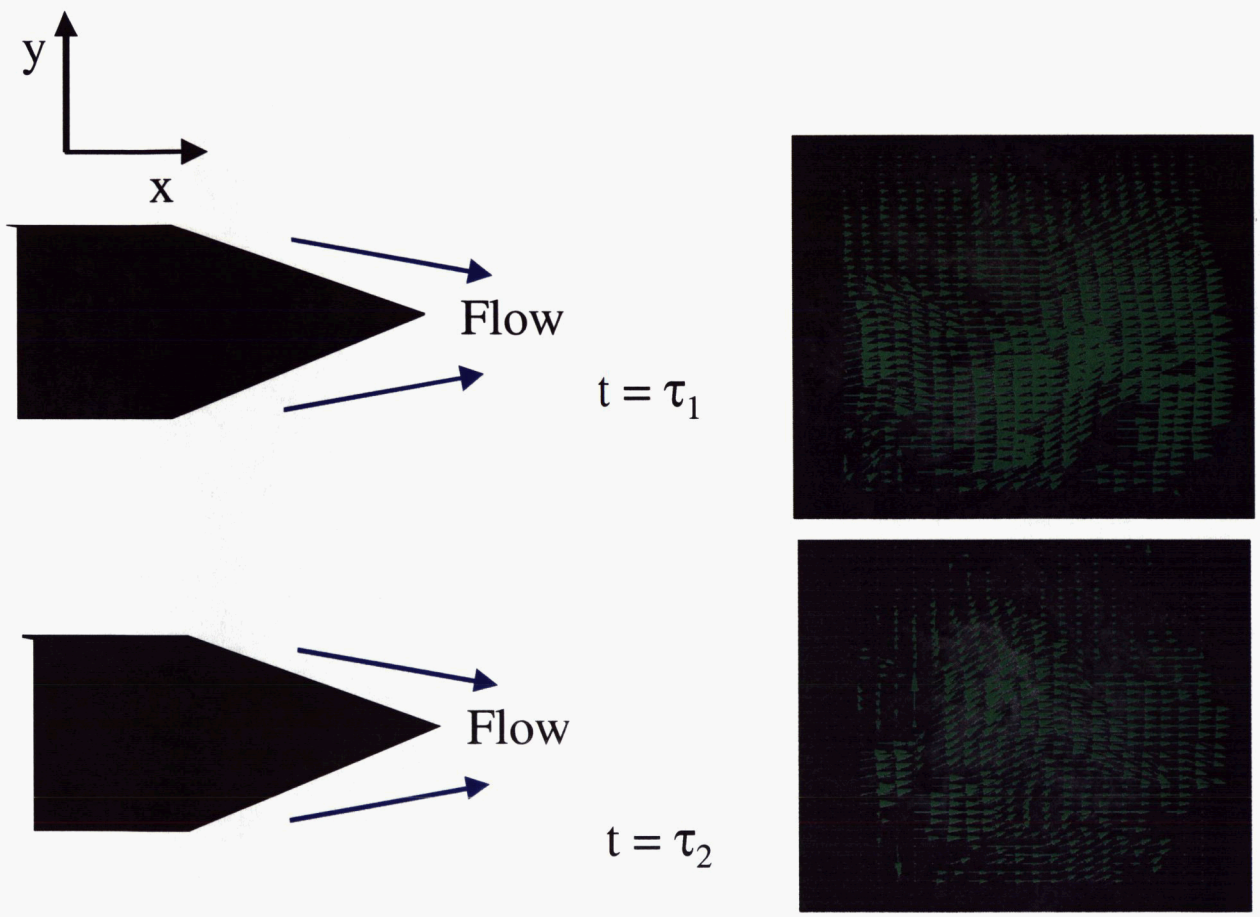

Figure 7.4 Observed flapping of DE jet downstream of nozzle exit at NPR = 1.52

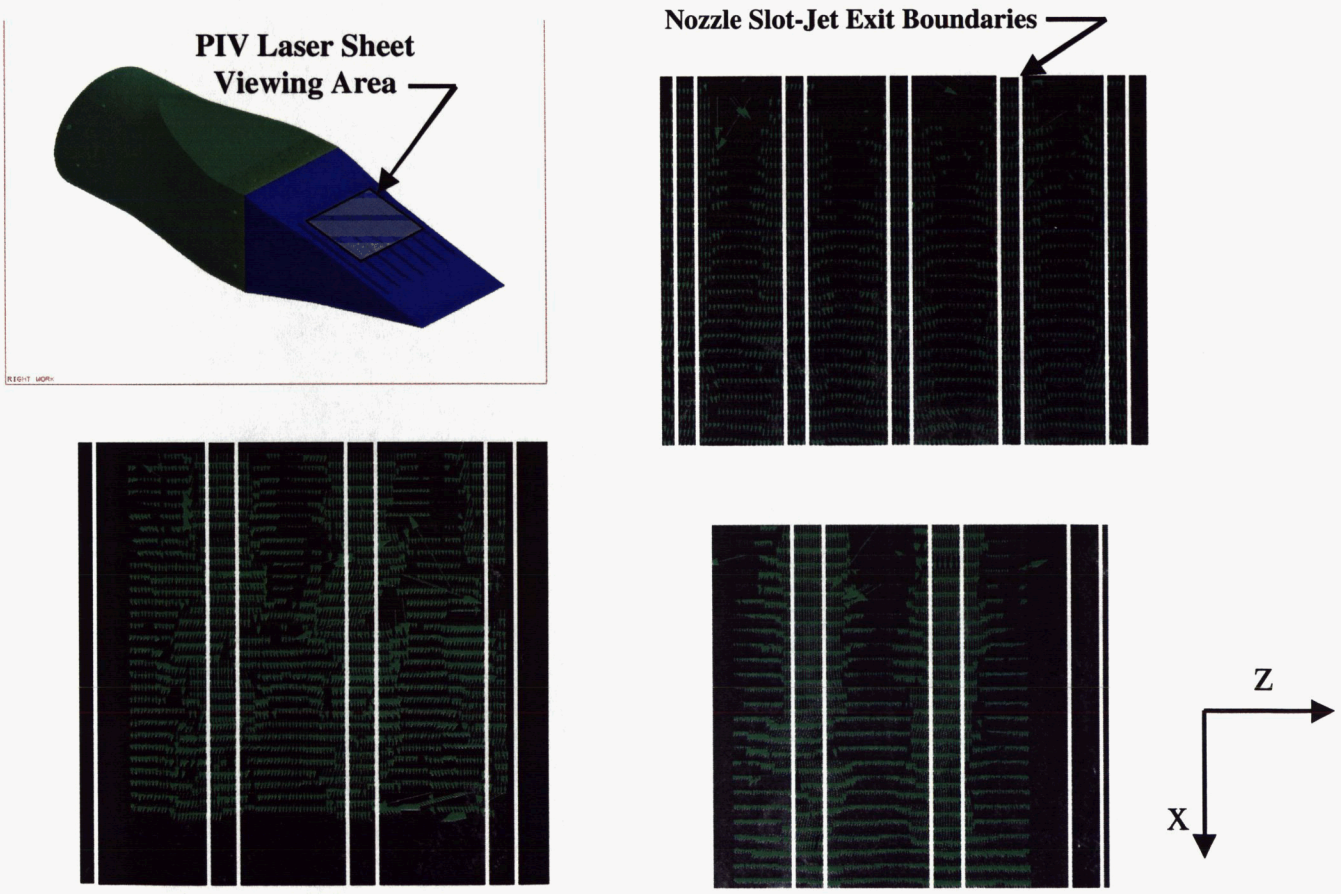

Figure 7.5 Instantaneous velocity at cross exit plane of the DE nozzle [PIV results].

that the individual jets are not fully merged in the first quarter section of the nozzle slope. Furthermore, the velocity vectors show a coherent fluctuation in the z-direction. This is evidence of the inherent instability in each individual jet. Figure 7.6 shows one of the slanting sides of the DE nozzle, with the laser sheet imaging the same plane as shown in Figure 7.5. Note the merging of the jets and the instability waves. Finally, Figure 7.7 shows, under more subtle lighting, that the instability waves perpetuate to nearly the tip of the slant nozzle.

The flow visualization of the DE nozzle confirms the unique individual jet evolution into a single larger jet. It should be recalled that, it was desired that the individual jets should retain their identity for as far downstream as possible. This would allow them to coalesce into each other at a lower velocity, thus producing lower noise amplitudes at the lower frequencies. The acoustic results shown earlier and the flow visualization results presented here seem to confirm that this goal was achieved.

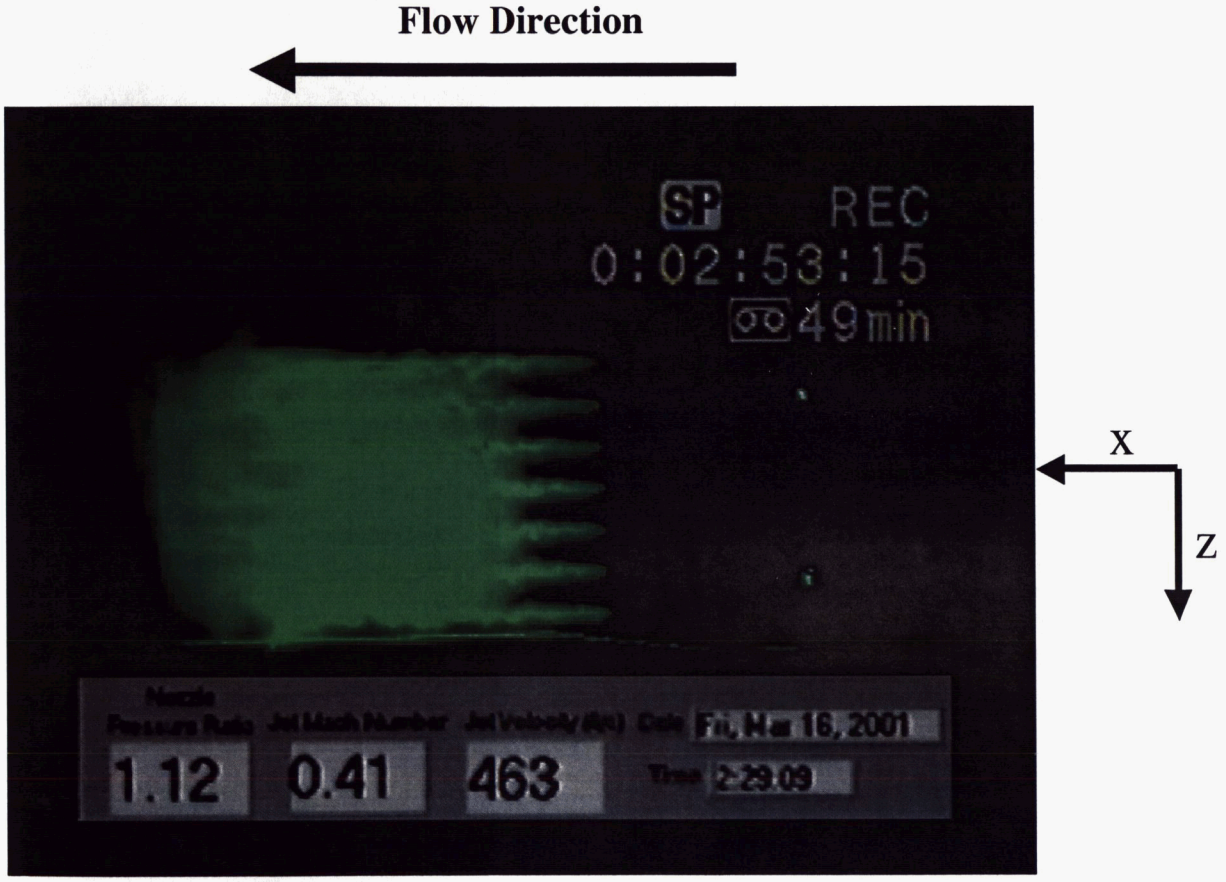

Figure 7.6 Planar image of DE nozzle exhaust flow showing individual slot-jets issuing in streamwise direction revealing merging location and jet instabilities [NPR = 1.12, U_j = 463 ft/s].

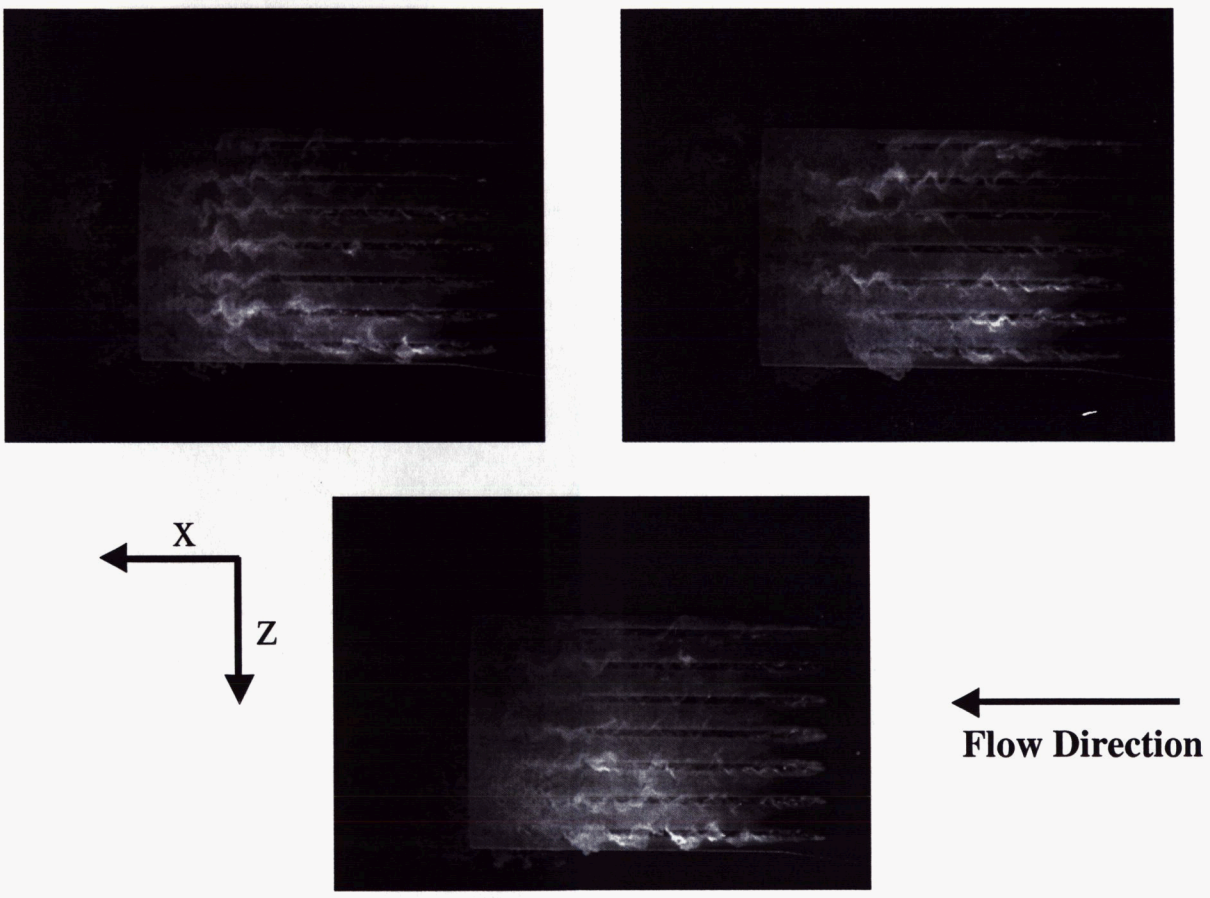

Figure 7.7 Planar image of DE nozzle exhaust flow showing individual slot-jets issuing in streamwise direction revealing merging location and jet instabilities [NPR = 1.52].

8.0 Fluid Shielding in Distributed Exhaust Nozzle Arrangement

After examining the acoustic data of the microphones located at the azimuthal angles of $\Phi = 90^{\circ}$, it was suspected that if the view of a given slot were blocked by an adjacent slot jet or collection of jets, that latter might be shielding the noise of the jet they are shielding. To establish the role of such fluid shielding, the acoustic performance of the DE nozzle was examined by operating only a partial number of the slot-jets that make up the nozzle exhaust. The DE nozzle was installed in the same facility that was used for the flow visualization. While not an anechoic chamber, the walls of the facility were covered with 4-inch thick acoustic foam and the floor was partially covered with the same foam. Microphones were placed at polar angles of 30, 60, and 90 degrees at an azimuthal angle of 90 degrees and a 5 foot radius from the center of the slanted surface of the DE nozzle. Figure 8.1 shows a schematic of this set-up.

Individual slot-jets were allowed to flow air by alternately closing off several of the slot jets with a "plug" from the inside of the nozzle. Furthermore, the entire bottom half of the slots were closed off entirely. Figure 8.2 shows how the slot nomenclature for this series of testing. The slot-jets on the top half of the nozzle were numbered from 1 to 7, with slot 7 closest to the microphone.

Figure 8.3 shows the 1/3-octave spectra of the incremental addition of individual slot-jets of the DE nozzle at three polar angles at an NPR = 1.52. Interesting results are obtained. For example, at $\theta = 30^{\circ}$, on increasing the number of slot jets from 1 to 2, the noise at low frequencies (below 8 kHz) has increased between 2 – 6 dB, whereas it is within measurement error at the higher frequencies. On doubling the number of sources, one should expect the noise to increase by 3 dB. It appears that at the lower frequencies, additional noise is produced by the interaction of the two jets and thus the increase is somewhat more than 3 dB. Lack of such an increase at high frequencies indicates possible fluid shielding referred to above at these frequencies. In fact at $\theta = 30^{\circ}$, even increasing the slot number to seven, produces very little increase at all frequencies higher than 10 kHz.

At larger polar angles of 60° and 90°, the fluid shielding does not appear to make much difference at the higher frequencies. Noise at almost all frequencies increases with increasing

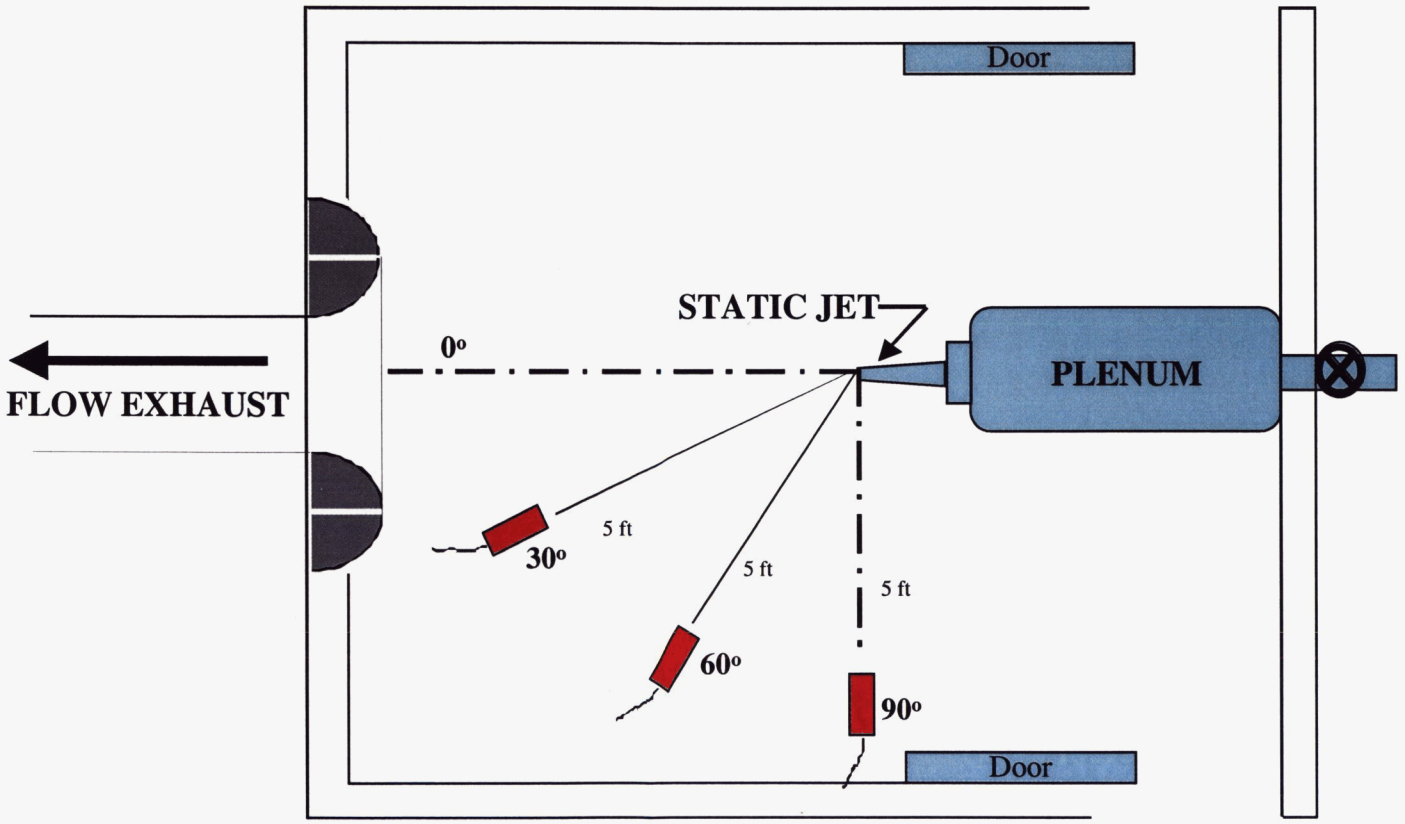

Figure 8.1 Microphone arrangement for testing of individual DE nozzle slots.

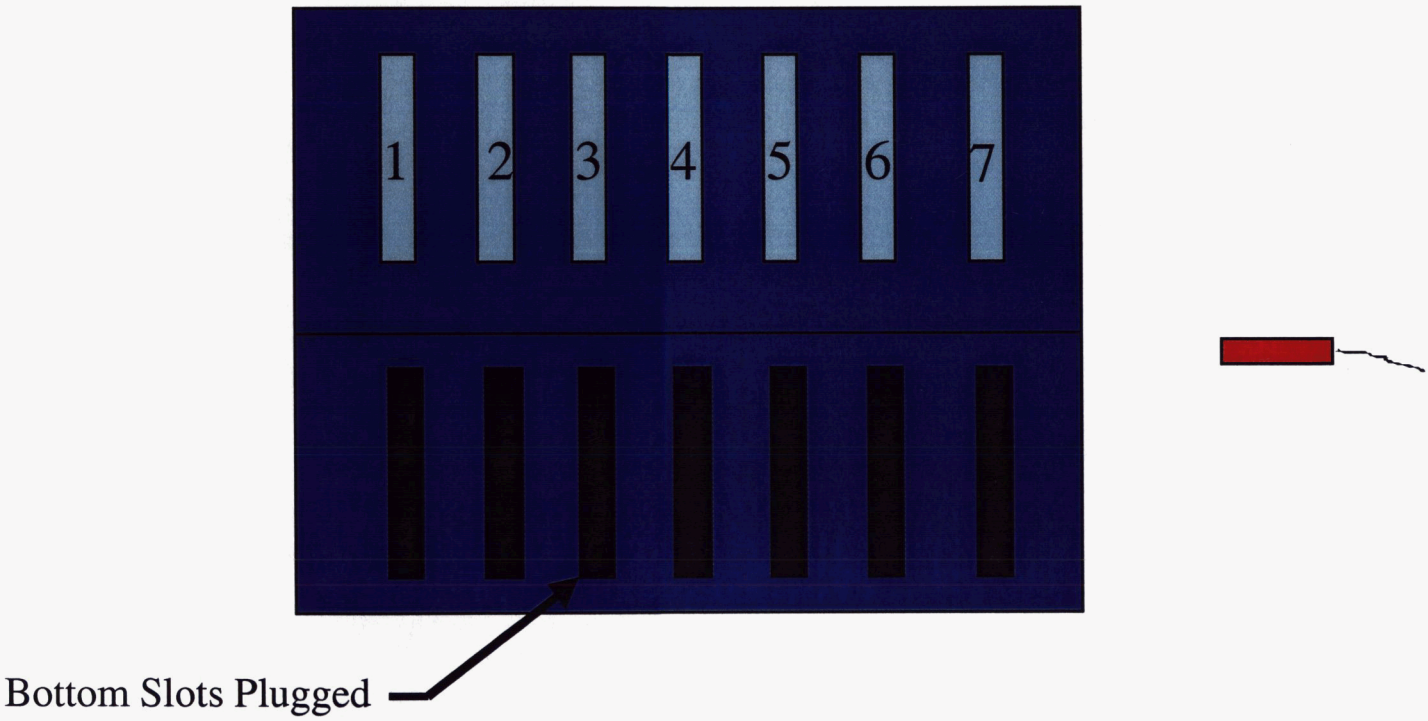

Figure 8.2 Configurations of DE nozzle used to examine individual Slot-Jets.

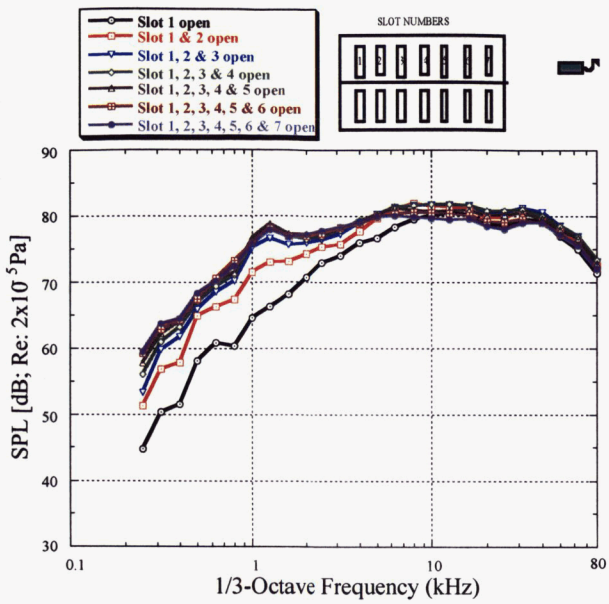

$\theta = 30^{o}$

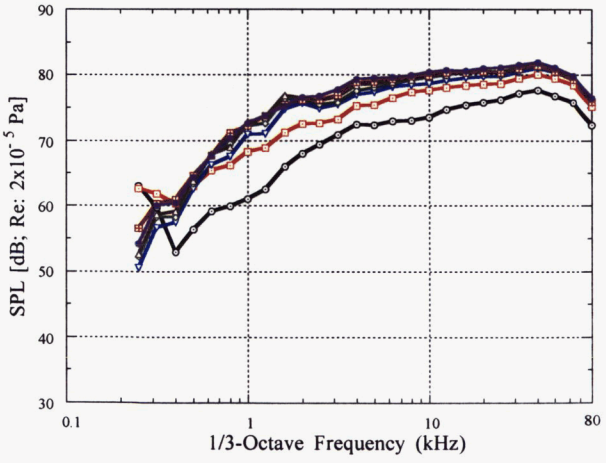

$\theta = 60^{o}$

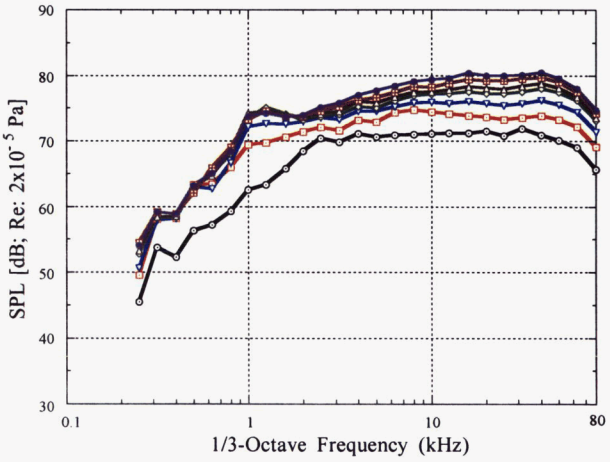

$\theta = 90^{o}$

Figure 8.3 Effect of individual slot-jets of the DE nozzle on farfield noise [NPR = 1.52; $\Phi = 90^{o}$; R = 12 ft; Corrected for atmospheric absorption]

the number of slots either in proportion to the exit area or even higher due to increased fluid dynamic interaction between the jets. At lower frequencies, noise does not change much when the number of slots is increased from 4 to 7. Figure 8.4 shows this more clearly. Figure 8.5 shows spectra for an NPR = 2.40. Trends similar to those for the subsonic data are observed at the supersonic condition.

A detailed analysis of the mechanism responsible for this interesting effect is beyond the scope of this effort, but should be made a part of the future research. Noting that the refraction effect is strong at higher frequencies and at shallow angles and the effect of refraction through multiple slot jets should be included in any future study. A computational aeroacoustic investigation complemented by a well-designed experimental study will be ideal. Effect of scattering and turbulence absorption of sound by the shear layer of multiple jets should also be incorporated.

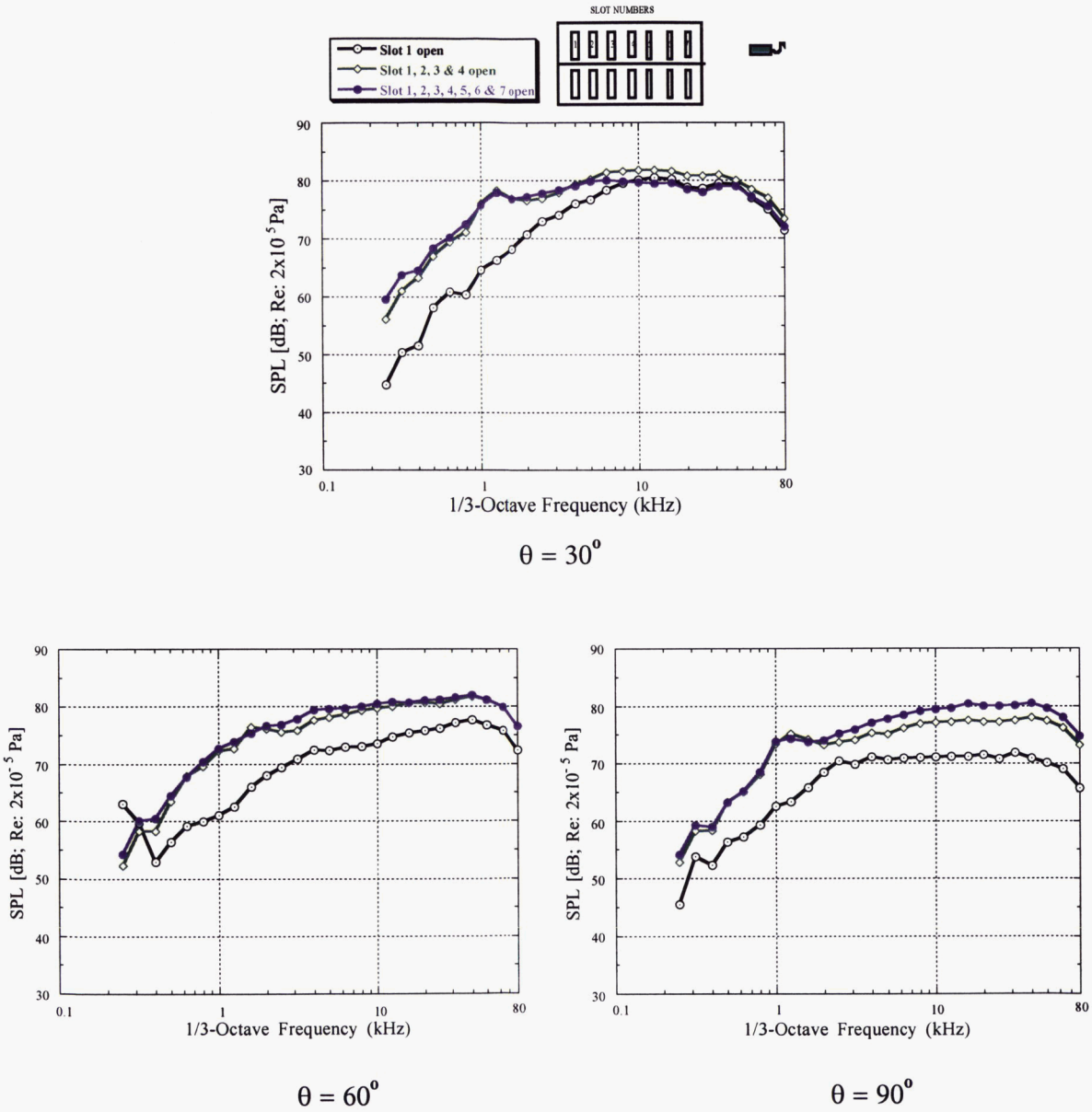

Figure 8.4 Effect of one, four, and seven slot-jets of the DE nozzle on farfield noise

[NPR = 1.52; $\Phi = 90^{o}$; R = 12 ft; Corrected for atmospheric absorption]

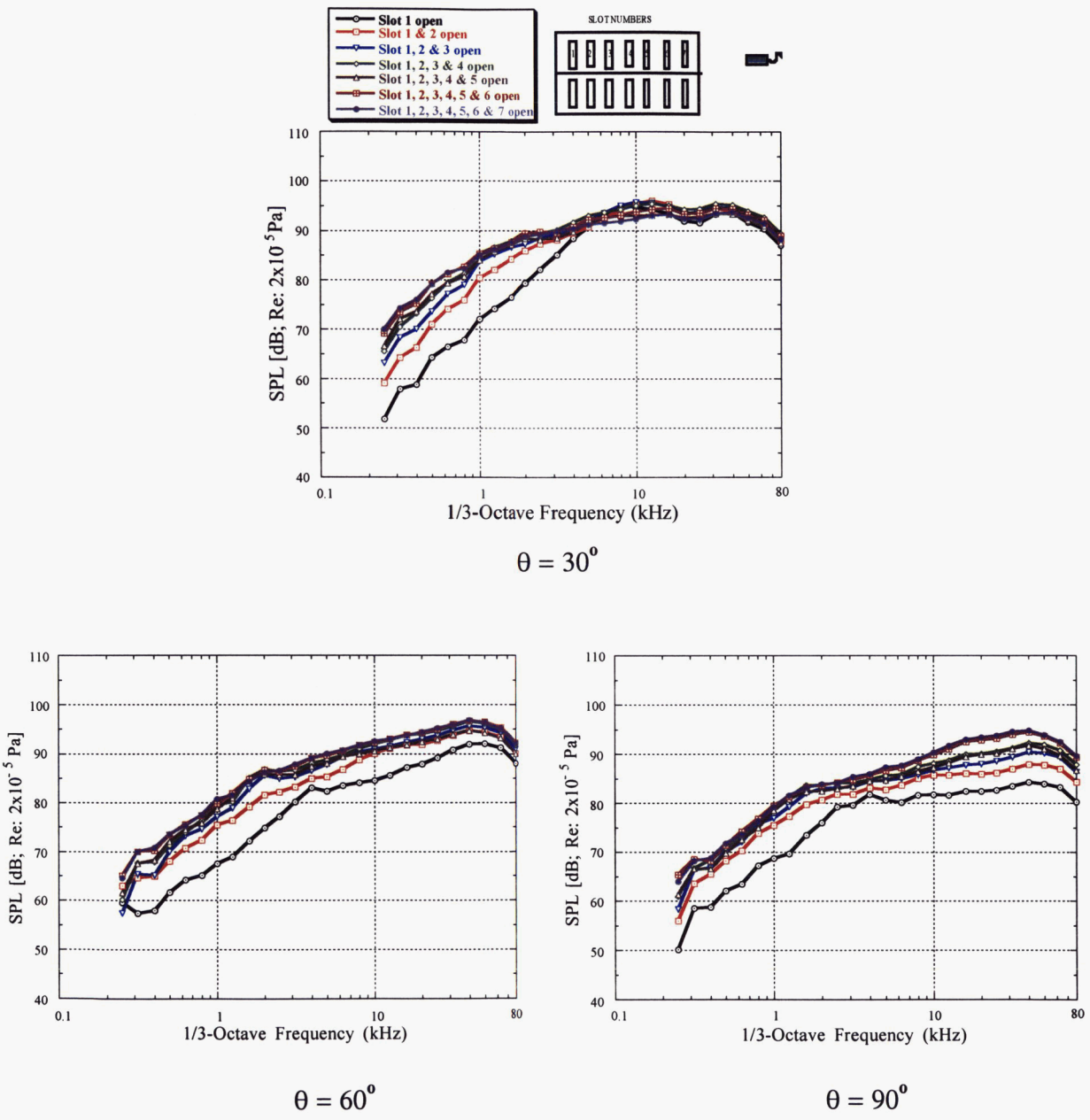

Figure 8.5 Effect of individual slot-jets of the DE nozzle on farfield noise [NPR = 2.40; $\Phi = 90^{\circ}$; R = 12 ft; Corrected for atmospheric absorption]

9.0 References

1. Griffin, Jr., Ralph Cornelius, William David Bard, and Schein, David Brian,"Sound Suppressor Exhaust Structure," United States Patent 5,717,172, February10, 1998.

2. Kinzie, K. W., Brown, M. C., Schein, D.B., and Solomon, W. D., *Measurements and Predictions for a Distributed Exhaust Nozzle* , AIAA paper No. 2001-2236, Presented at the 7th AIAA/CEAS Aeroacoustic Conference, 28-30 May, 2001, Maastricht, The Netherlands.

3. Ahuja, K. K. and Bushell, K. W., *An Experimental Study of Subsonic Jet Noise and Comparison with Theory.* Journal of Sound and Vibration, Vol. 30 No. 3, pp 317-341, 1973.

4. Lighthill, M. J. *On Sound Generated Aerodynamically. I. General Theory* , Proceedings of the Royal Society A 221, 564 – 578, 1952.

5. Lighthill, M. J. *On Sound Generated Aerodynamically. II. Turbulence as a source of sound.* Proceedings of the Royal Society A 222, 1 – 21, 1954.

Appendix A Results from Reynolds Averaged Numerical Simulation of DE Nozzle

Further results from the numerical simulation of the DE nozzle (SS6) along with an equivalent flow area round nozzle for comparison are presented in this Appendix. Figures A.1 through A.6 are for the Nozzle Pressure Ratio (NPR) 1.52 and Nozzle Temperature Ratio (NTR) 1.00 run condition in still sea-level air. Particle traces results in Figure A.1 show how the SS6 outboard exit jets move inboard in toward the relatively low-pressure inboard jets. Figures A.2 through A.6 show isosurfaces for comparing the potential decay.

Figures A.7 through A.14 are for the Nozzle Pressure Ratio (NPR) 2.425 and Nozzle Temperature Ratio (NTR) 1.0017 run condition in still sea-level air. Note how the particle traces in Figure A.7 show a greater level of suction by the inboard jets compared to the NPR 1.52 case. Shock cells are now evident on the round nozzle Mach 1.2 isosurfaces shown in Figure A.14.

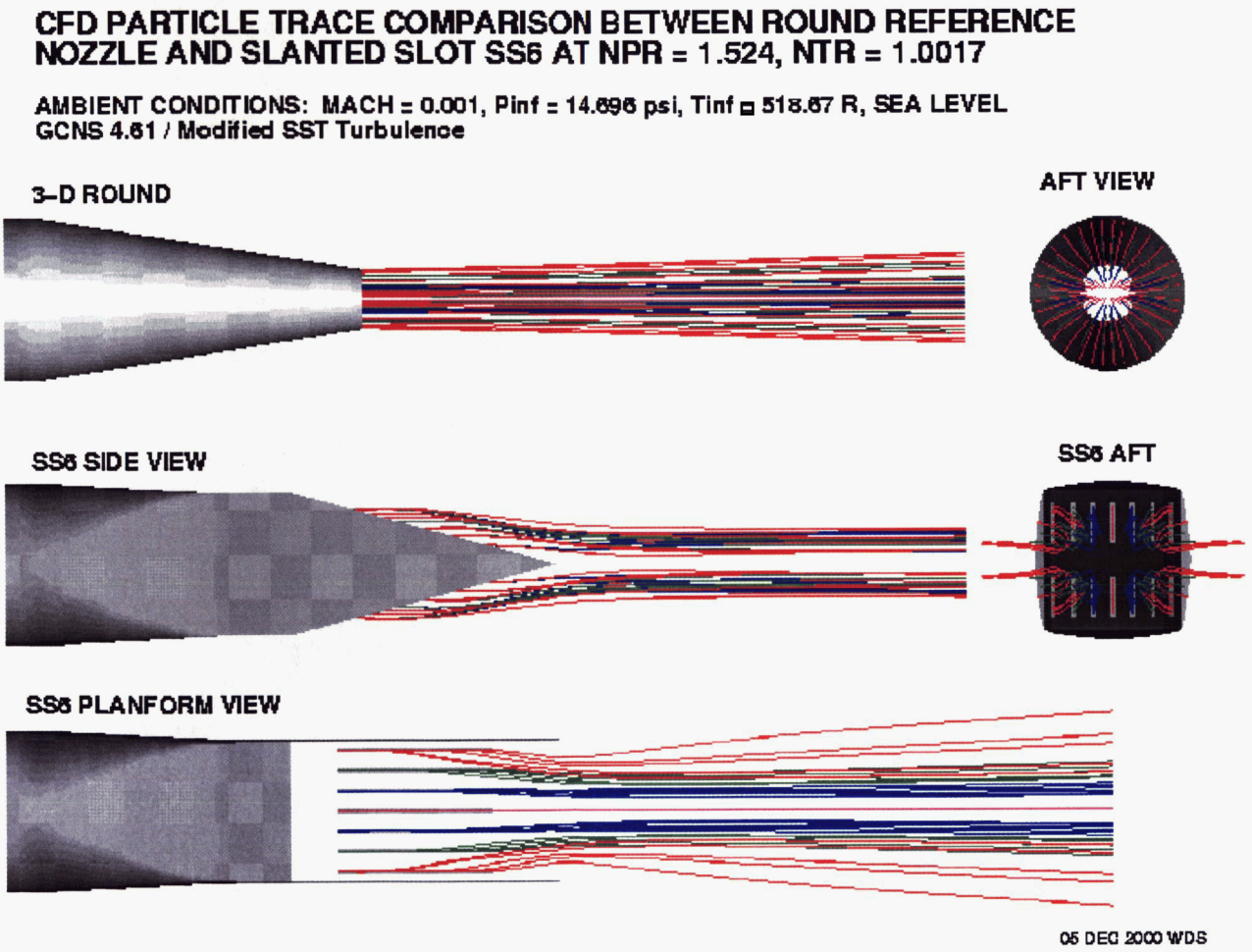

Figure A.1 Particle traces of DE SS6 nozzle with comparison to round nozzle [NPR=1.52; NTR=1.00]

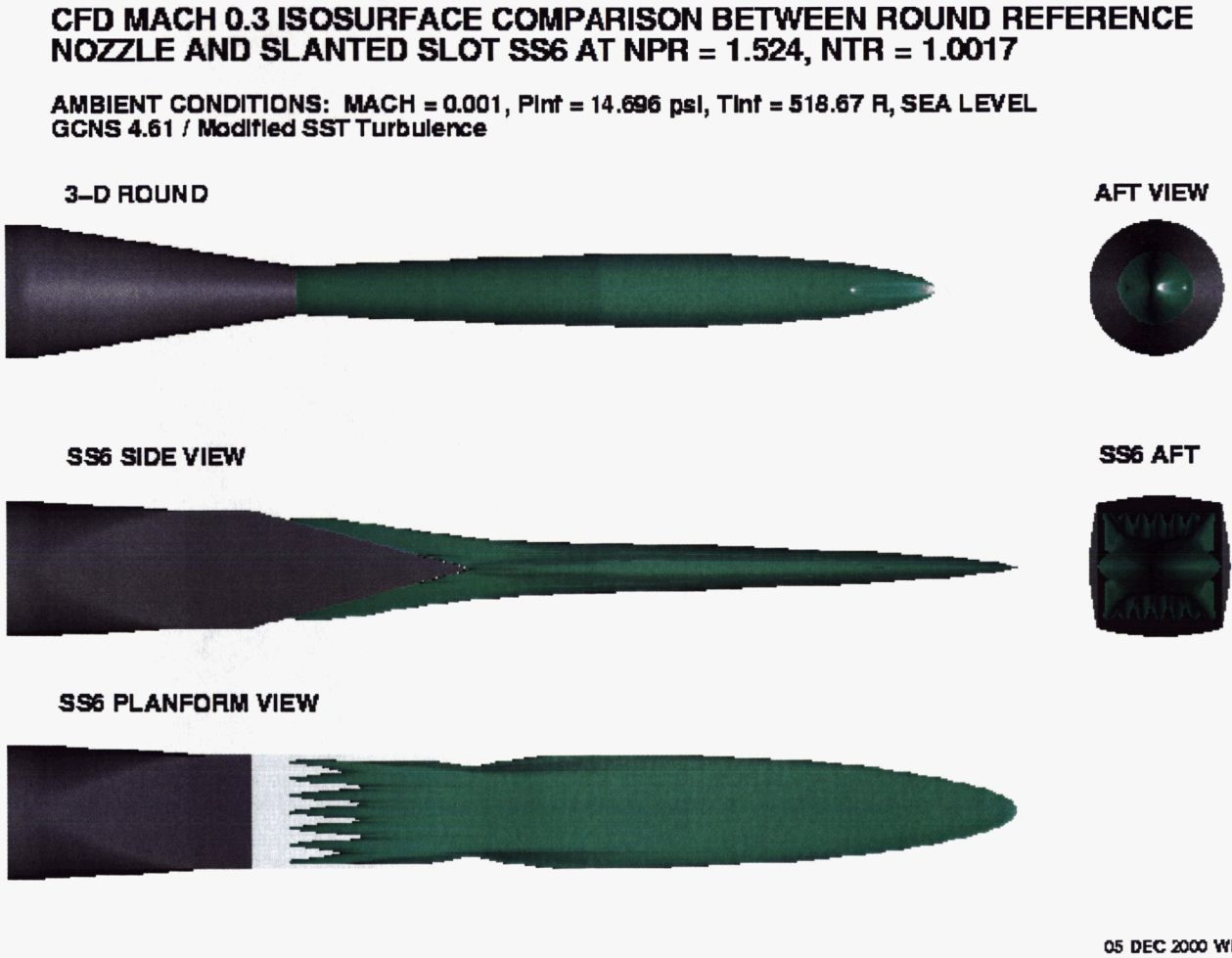

Figure A.2 Isosurface of M=0.3 of DE SS6 nozzle with comparison to round nozzle [NPR=1.52; NTR=1.00]

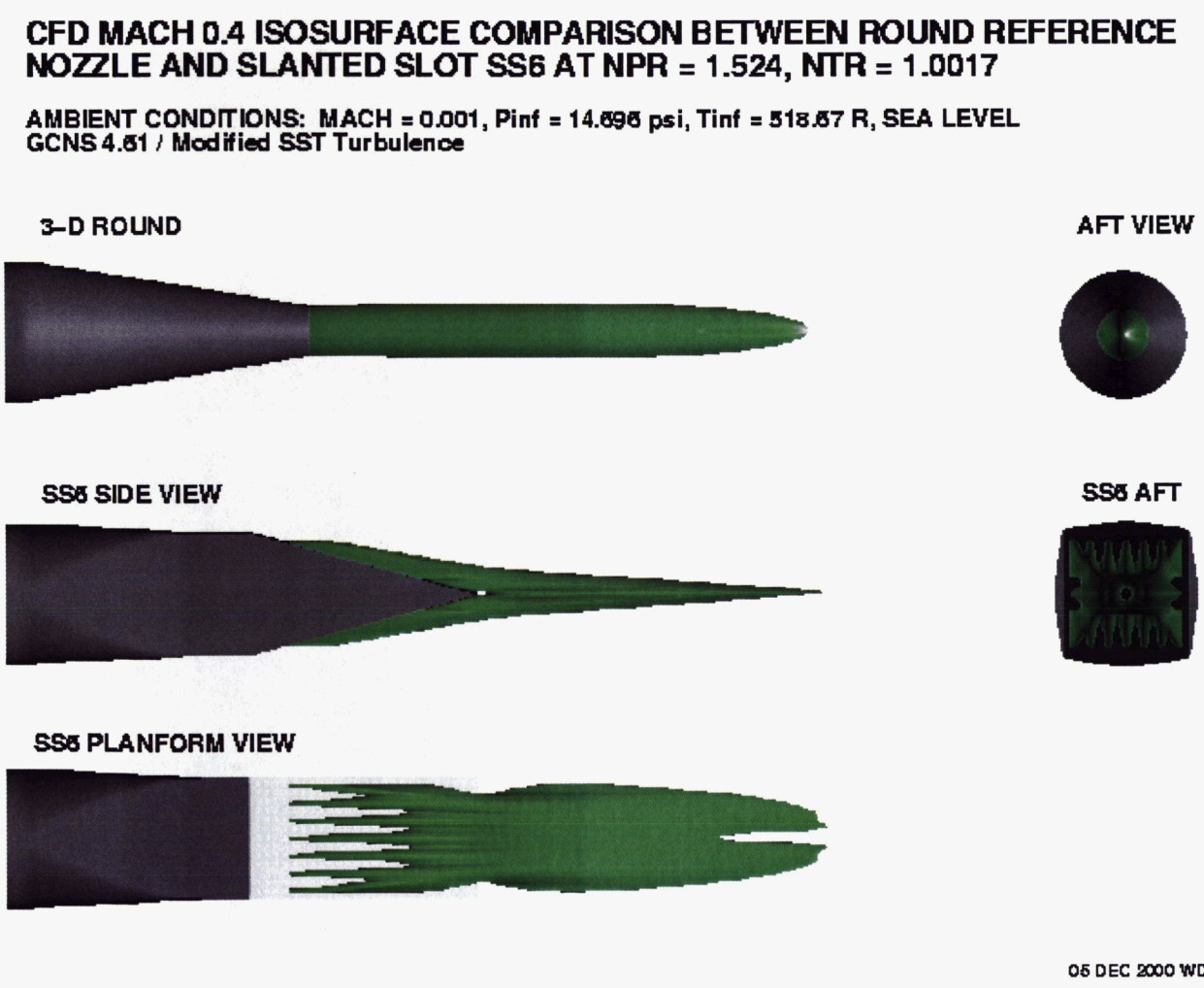

Figure A.3 Isosurface of M=0.4 of DE SS6 nozzle with comparison to round nozzle [NPR=1.52; NTR=1.00]

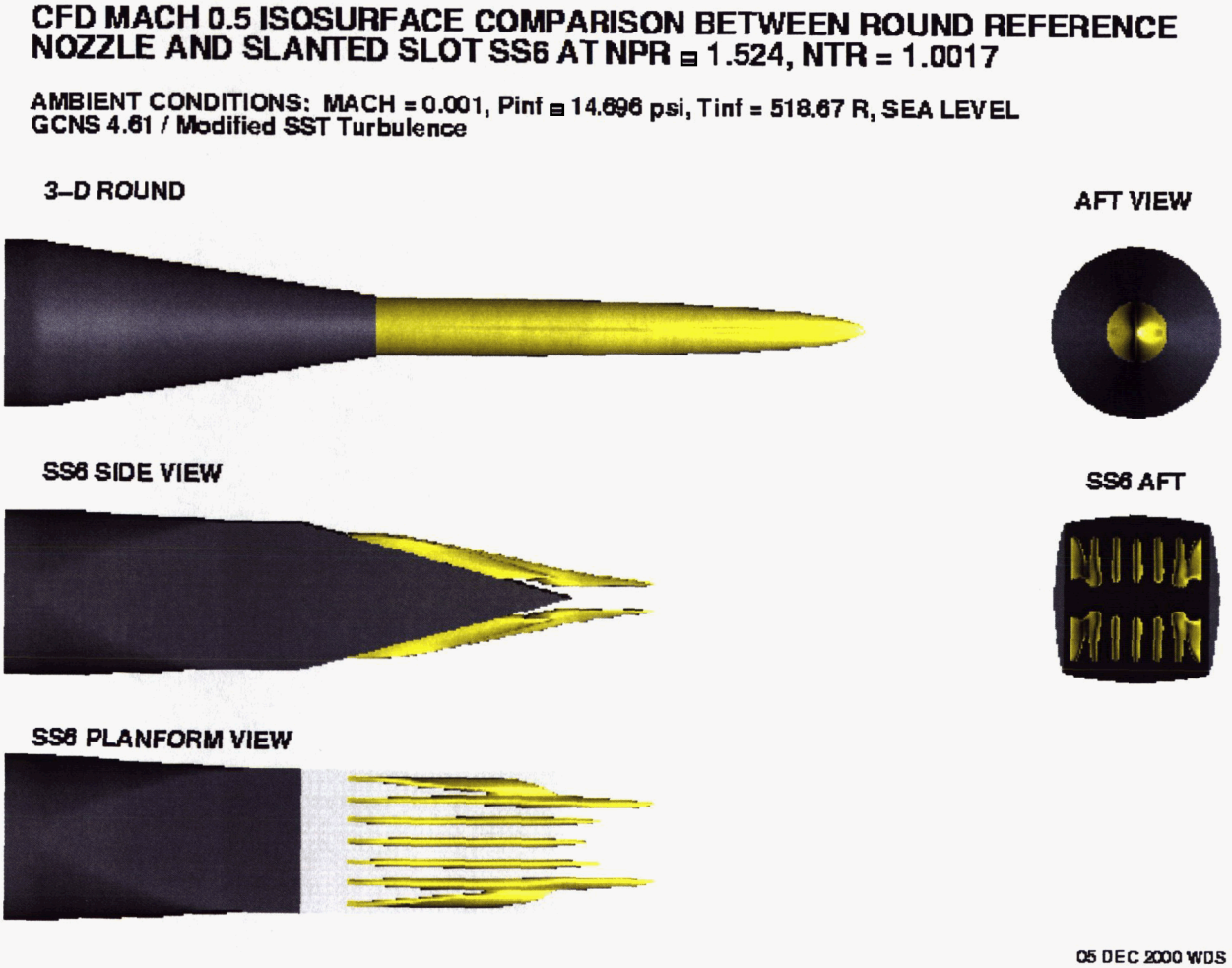

Figure A.4 Isosurface of M=0.5 of DE SS6 nozzle with comparison to round nozzle [NPR=1.52; NTR=1.00]

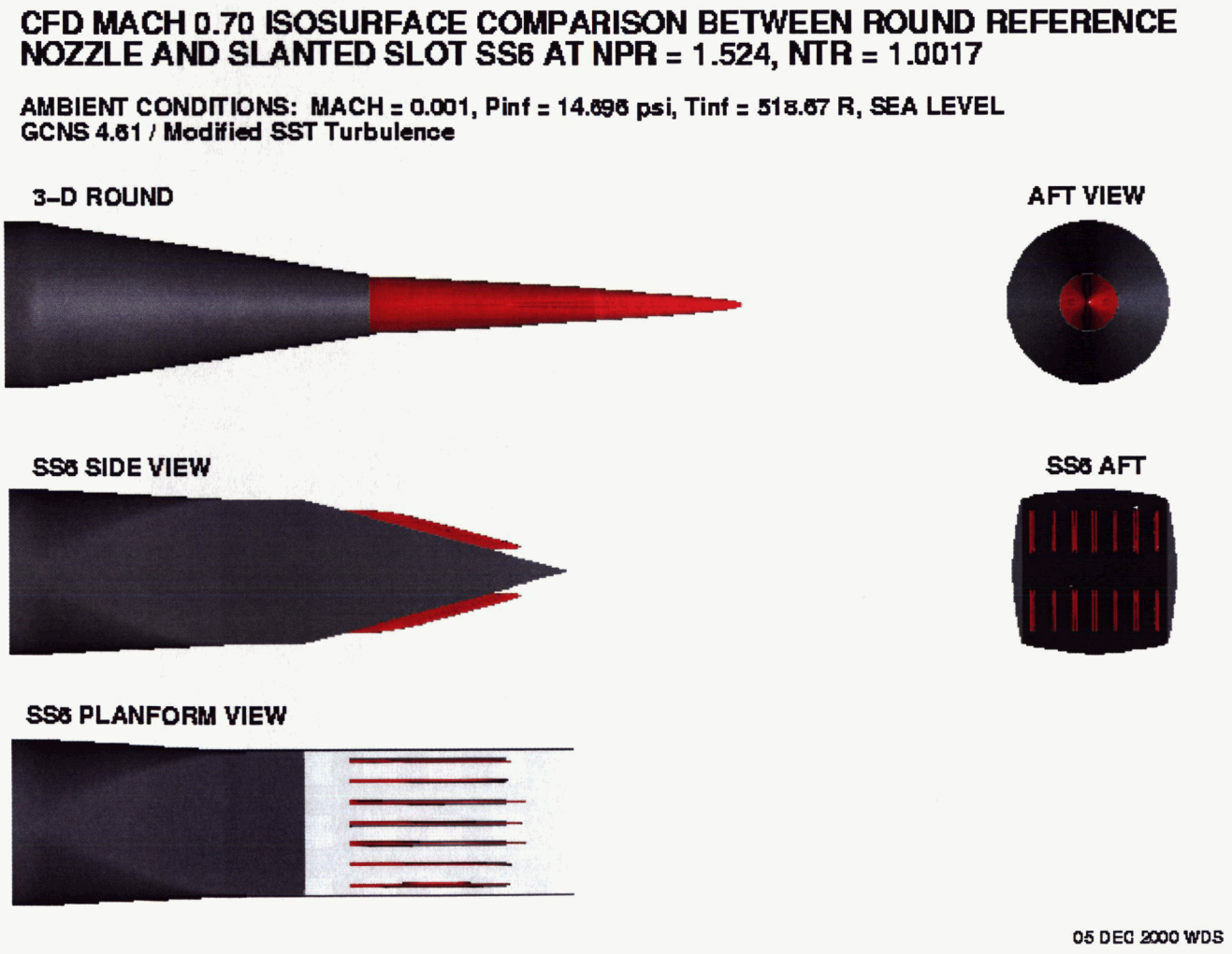

Figure A.5 Isosurface of M=0.7 of DE SS6 nozzle with comparison to round nozzle [NPR=1.52; NTR=1.00]

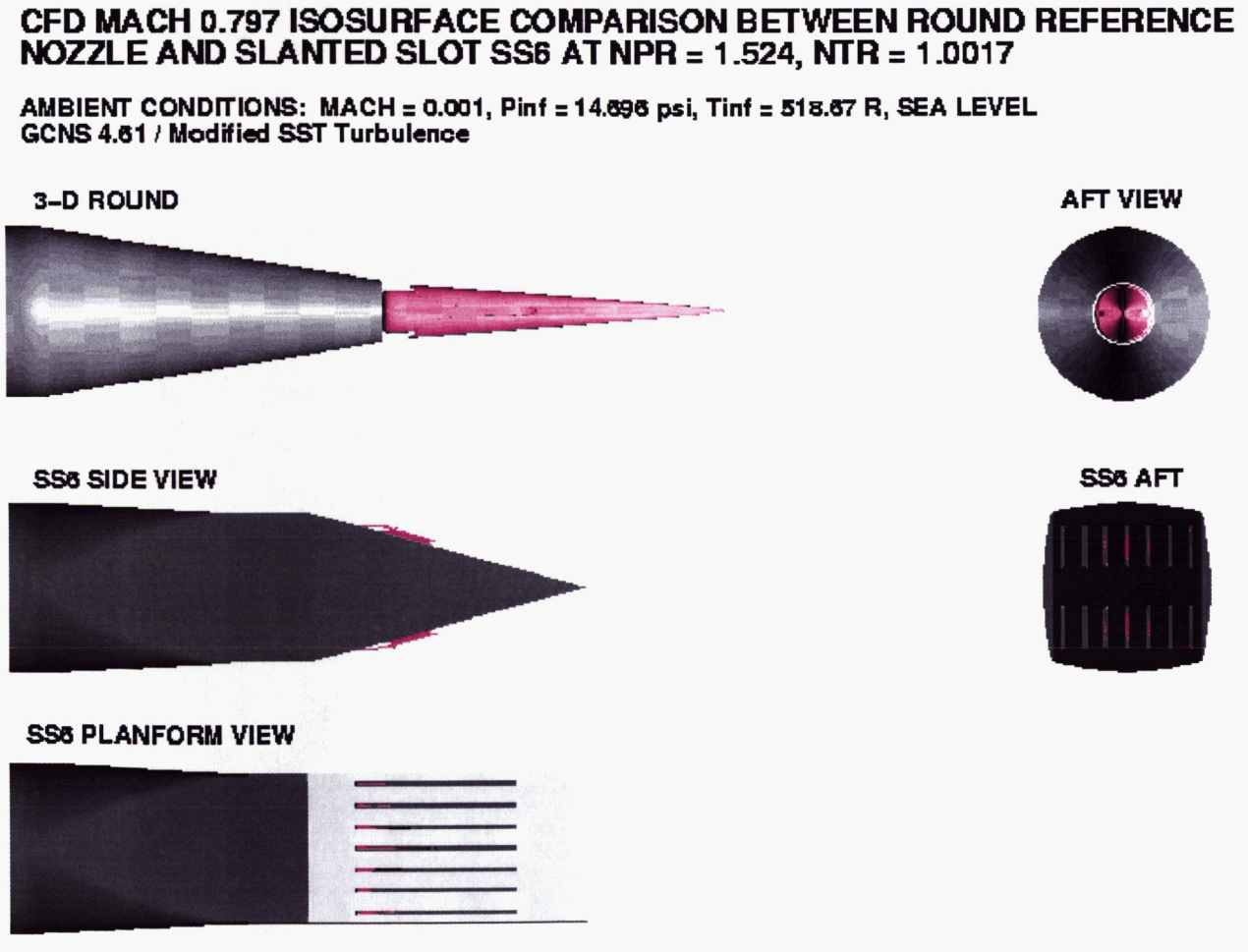

Figure A.6 Isosurface of M=0.8 of DE SS6 nozzle with comparison to round nozzle [NPR=1.52; NTR=1.00]

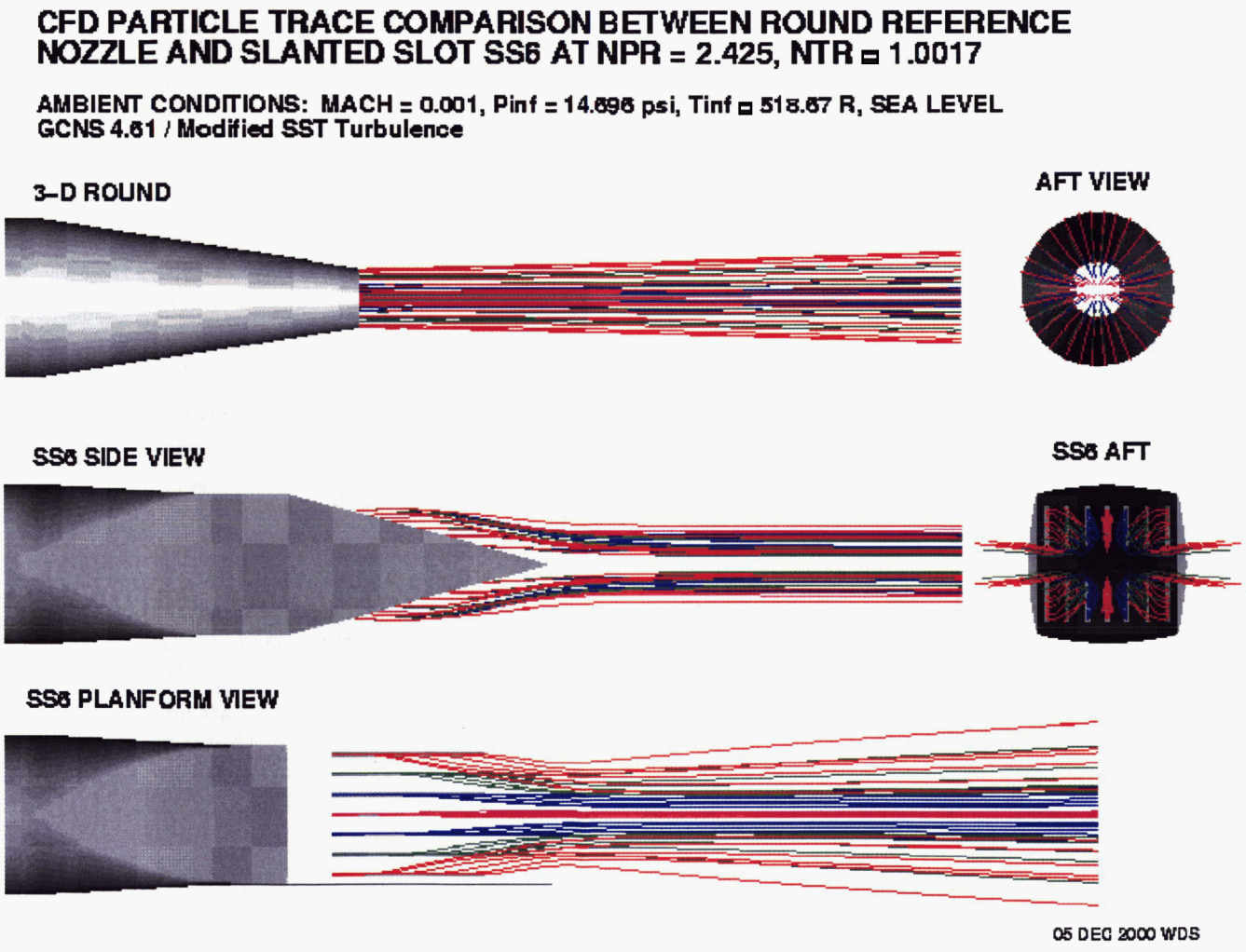

Figure A.7 Particle traces of DE SS6 nozzle with comparison to round nozzle [NPR=2.43; NTR=1.00]

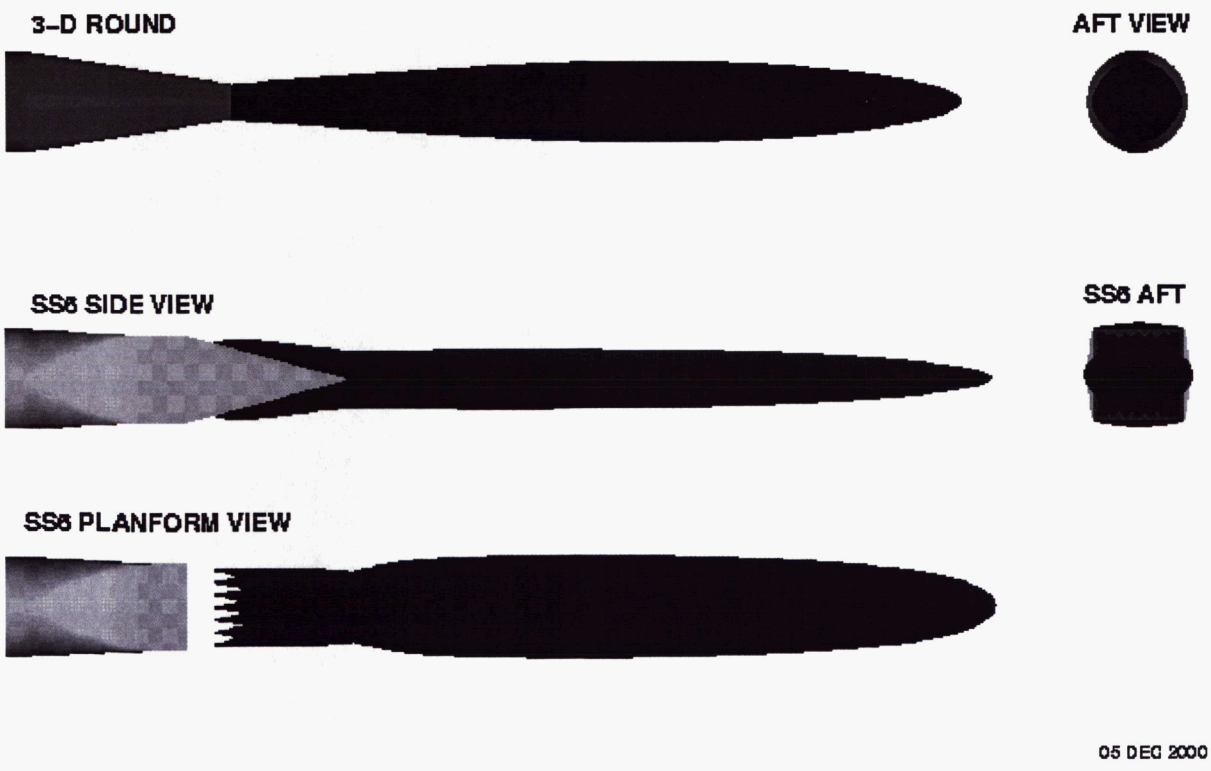

Figure A.8 Isosurface of M=0.3 of DE SS6 nozzle with comparison to round nozzle [NPR=2.43; NTR=1.00]

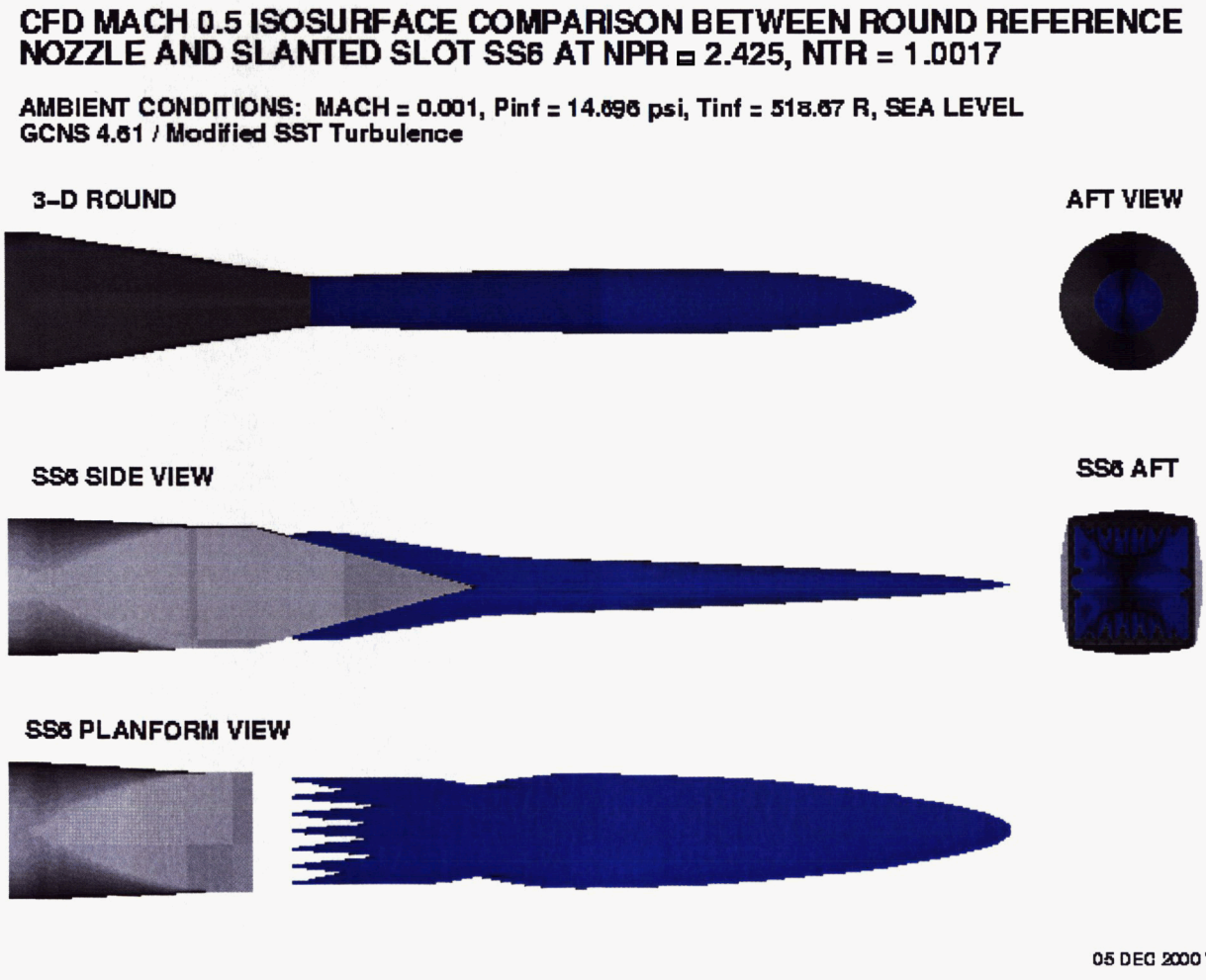

Figure A.9 Isosurface of M=0.5 of DE SS6 nozzle with comparison to round nozzle [NPR=2.43; NTR=1.00]

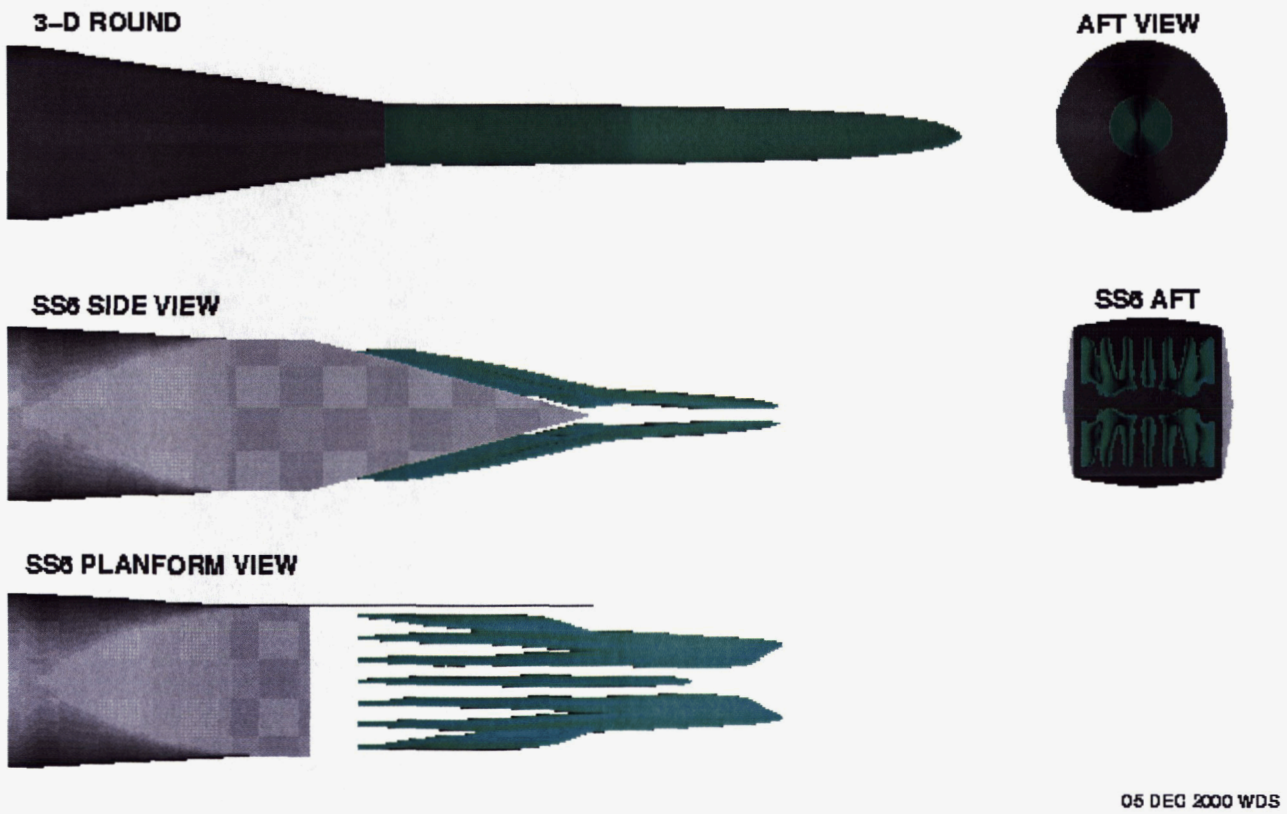

Figure A.10 Isosurface of M=0.7 of DE SS6 nozzle with comparison to round nozzle [NPR=2.43; NTR=1.00]

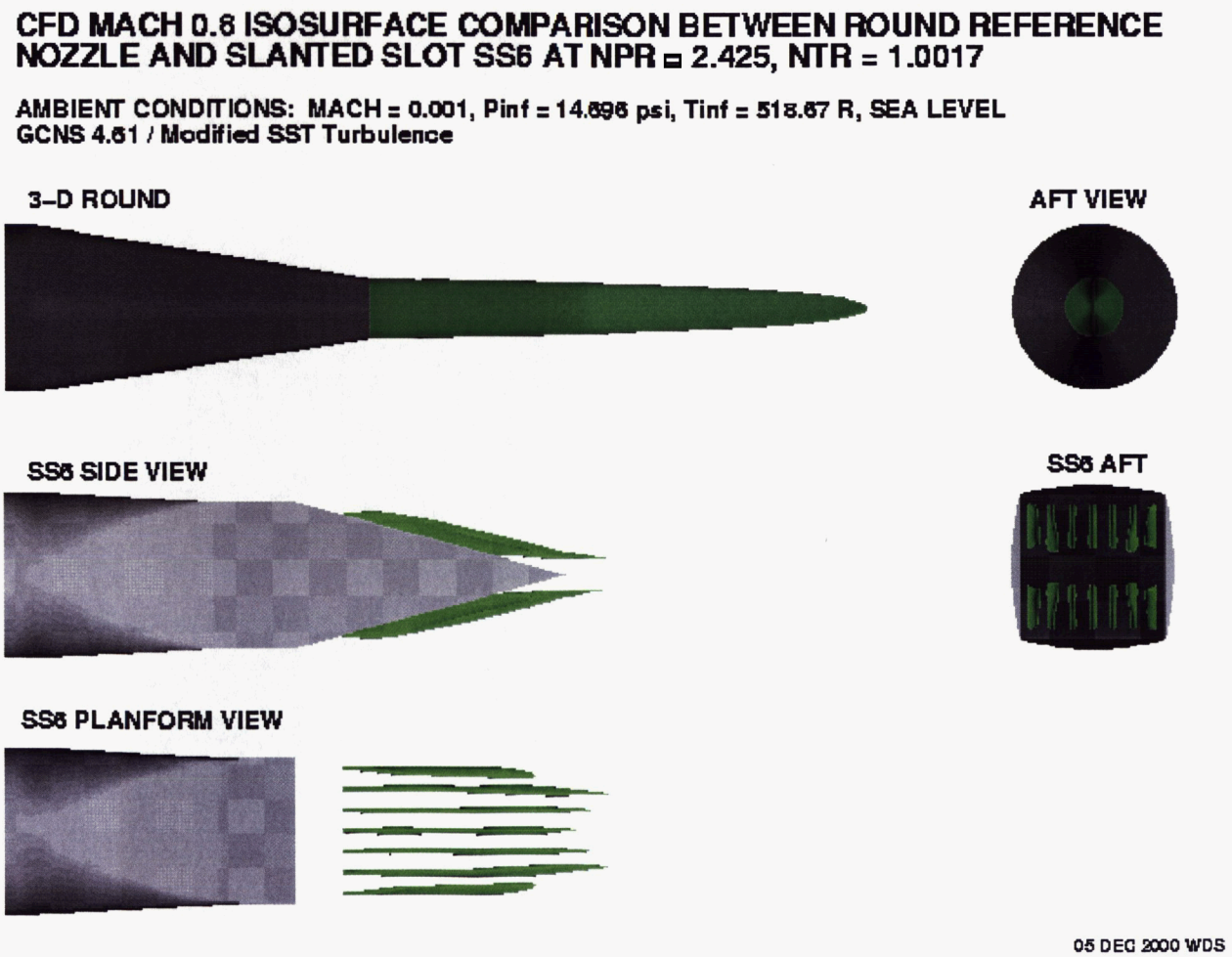

Figure A.11 Isosurface of M=0.8 of DE SS6 nozzle with comparison to round nozzle [NPR=2.43; NTR=1.00]

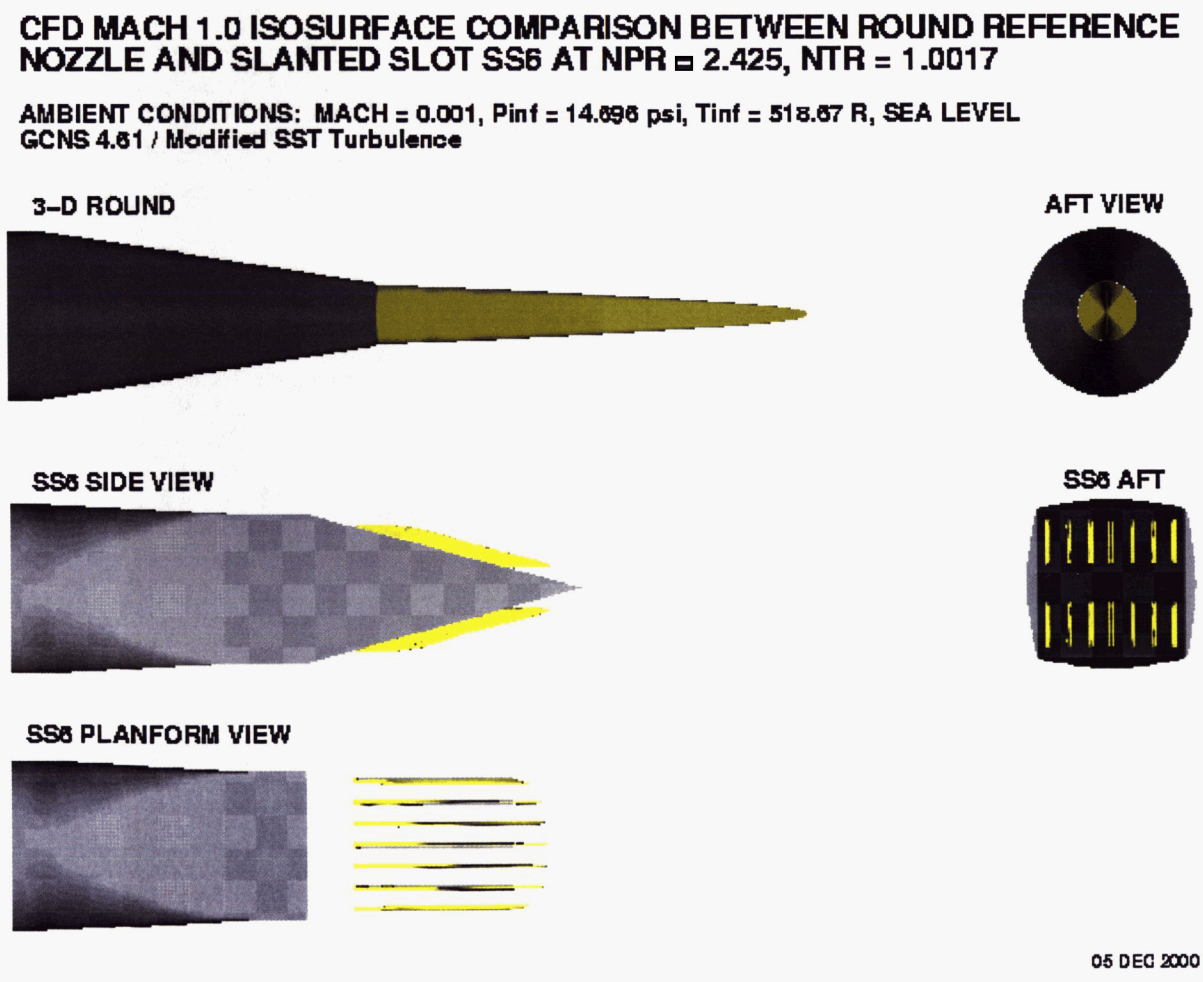

Figure A.12 Isosurface of M=1.0 of DE SS6 nozzle with comparison to round nozzle [NPR=2.43; NTR=1.00]

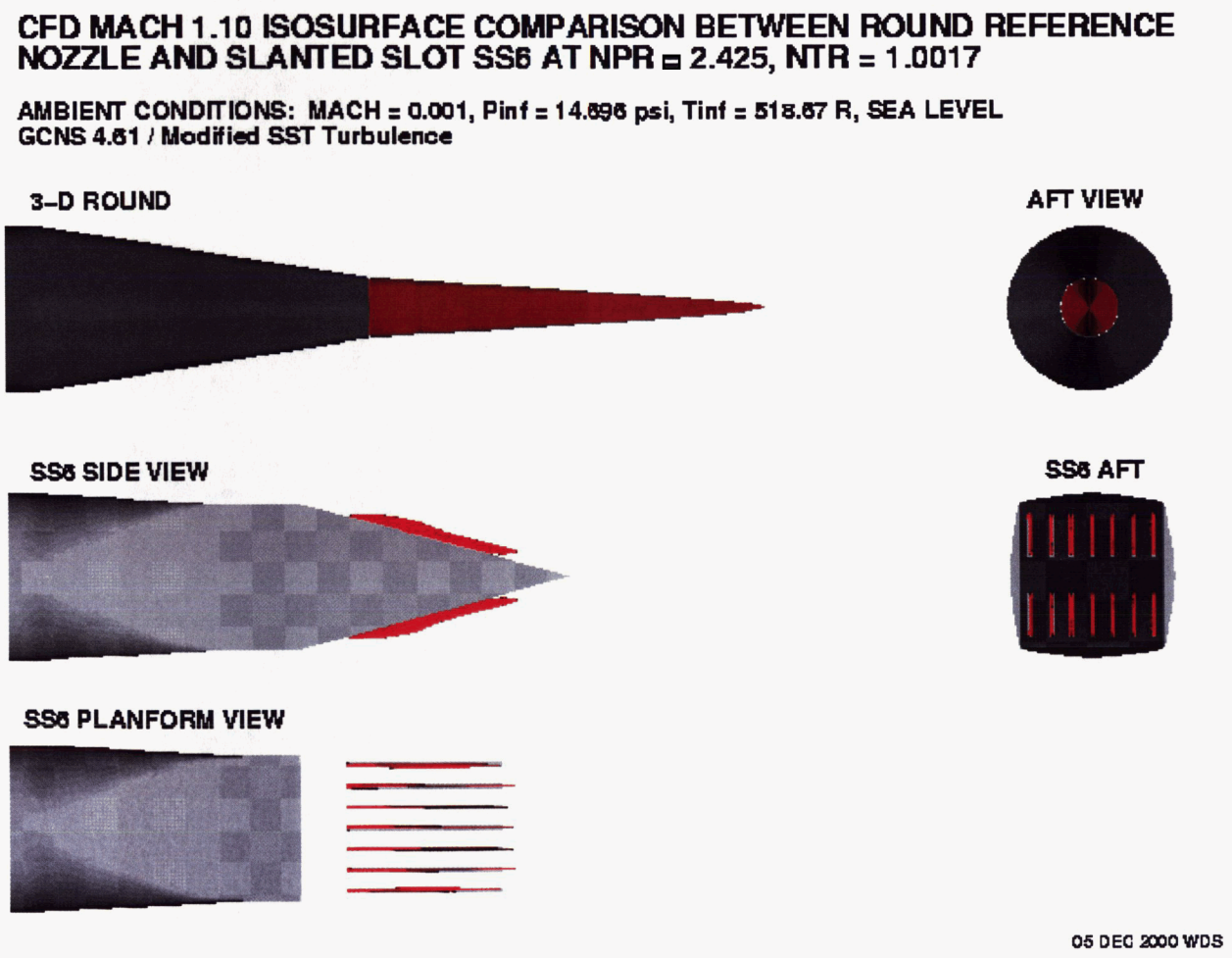

Figure A.13 Isosurface of M=1.1 of DE SS6 nozzle with comparison to round nozzle [NPR=2.43; NTR=1.00]

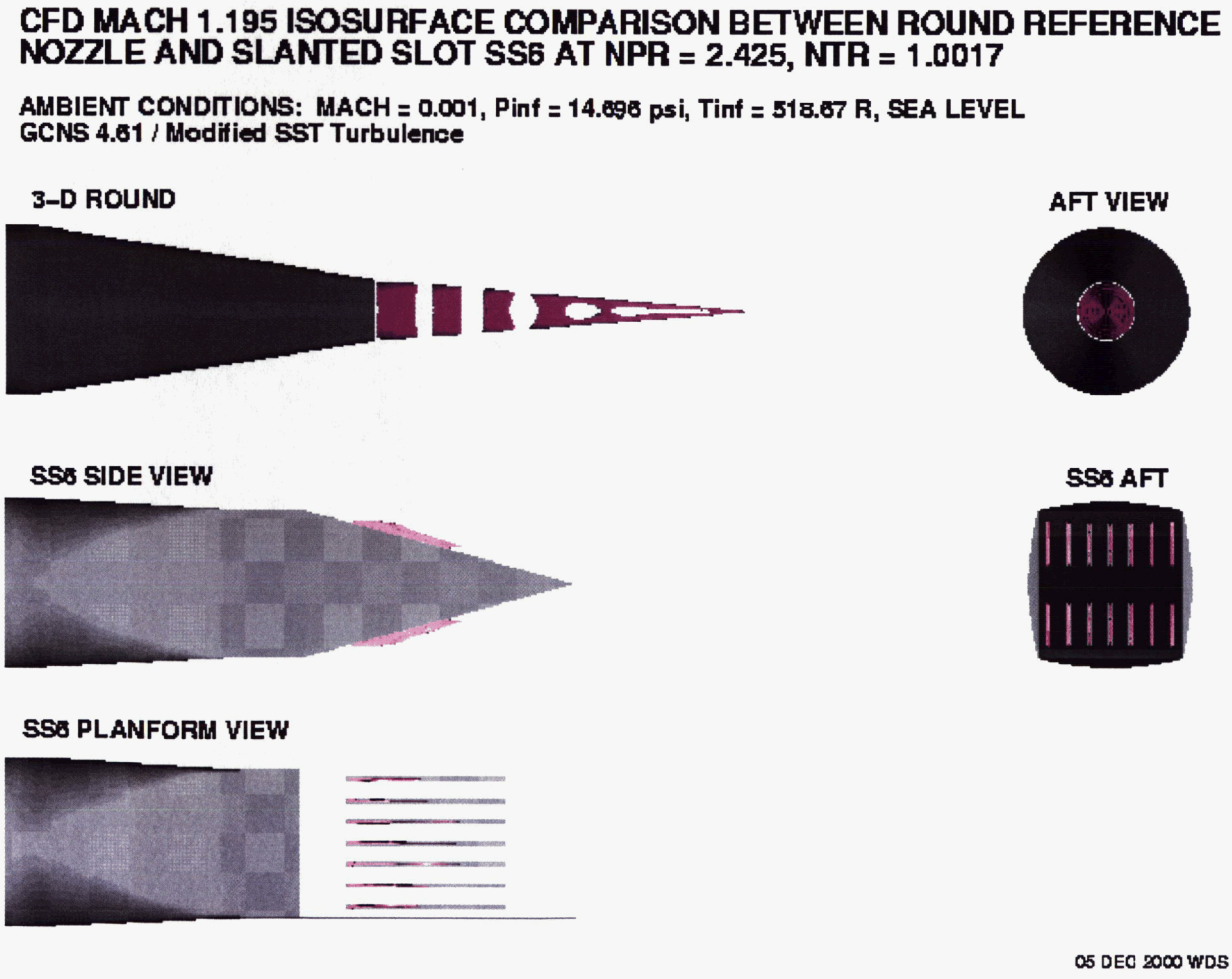

Figure A.14 Isosurface of M=1.2 of DE SS6 nozzle with comparison to round nozzle [NPR=2.43; NTR=1.00]

Appendix B: Microphone Correction Methodology

Introduction

There are several corrections applied to the acoustic data. Some of these corrections are due to the microphone system such as the frequency response correction, while the other corrections are more specific to the particular test and test conditions, such as the atmospheric absorption correction. In either case, the corrections were applied for two main reasons. First, these corrections removed any difference between tests that could influence the data, such as high humidity on one day and low humidity on another. The second reason for applying these corrections was to be able to present the data in a form that could be readily compared with other jet noise data on a standard level.

There were five corrections applied to the raw acoustic data. These included corrections for amplifier setting, the free-field and microphone grid, the individual frequency response of each microphone, distance (R^2 law), and atmospheric absorption. The reasoning for applying the correction and the method in which each correction was applied will be described in the following sections.

Amplifier Setting Correction

In addition to signal conditioning, the microphone power supplies have an amplifier built in that can be set to different levels. Thus, a wide range signal levels can be recorded over the same voltage range for the A/D input. This allows the user to take full advantage of the resolution of the A/D converter by keeping the voltage range small even for tests that span a large noise amplitude range for different test conditions. The amplitude of the microphone signals was calibrated typically at a middle range of the amplifier. Then, depending on the test conditions, the amplifier could be adjusted up or down to keep the voltage range the same for all tests points. This was easily done because the analyzer software displayed an 'overload' indicator when a signal was saturating the A/D converter. In order to make sure the signal was not too small, or not effectively using the voltage range of the A/D converter, the signal was viewed in an oscilloscope mode on the analyzer. The amplifier was then adjusted until the signal seemed to fill most of the voltage range.

The B & K power supplies used in the experiments had this capability built into the power supply unit. The user can adjust each microphone channel independently in 10 dB steps. However, when processing the data, the user must then reverse this process by adding the appropriate adjustment for each test point.

This was accomplished by keeping track of the amplifier setting at calibration and for each test point for each microphone. The difference between the settings was simply subtracted from the raw data.

$$SPL_{amp\_adjusted} = SPL - (Amp_{setting} - Amp_{cal}) \quad \text{(B.1)}$$

where SPL in this case is the entire SPL spectrum for a particular microphone at a particular test point. The $Amp_{setting}$ is also specific for each microphone and each test point. The calibration Amp signal was generally the same for all the microphones, however the post-processing code does allow for individual calibration amplifier settings.

This is a relatively simple correction and can be done anytime during the post-processing since it is a constant correction for all frequencies. Some of the other corrections are frequency and thus bandwidth dependent, however this is only a simple addition to the entire spectrum.

Microphone Free-Field and Grid Correction

There are several corrections provided by the manufacturer that need to be used to obtain the actual acoustic signal that would present at the microphone location if the microphone were not there. One of the major adjustments is the change in the spectrum simply due to the microphone surface being present. This is the free-field correction.

B & K designs their microphones to have a flat response across the entire frequency range of interest after the free-field correction is applied. This is very handy in many cases because the user need not make any changes to the data since the frequency response of the microphone is designed to have the exact opposite correction of the free-field correction. This is illustrated in **Figure B.1**. In the following discussion parenthesis will be used to denote the B & K terminology for the curves presented in the figure. This will prevent confusion for someone

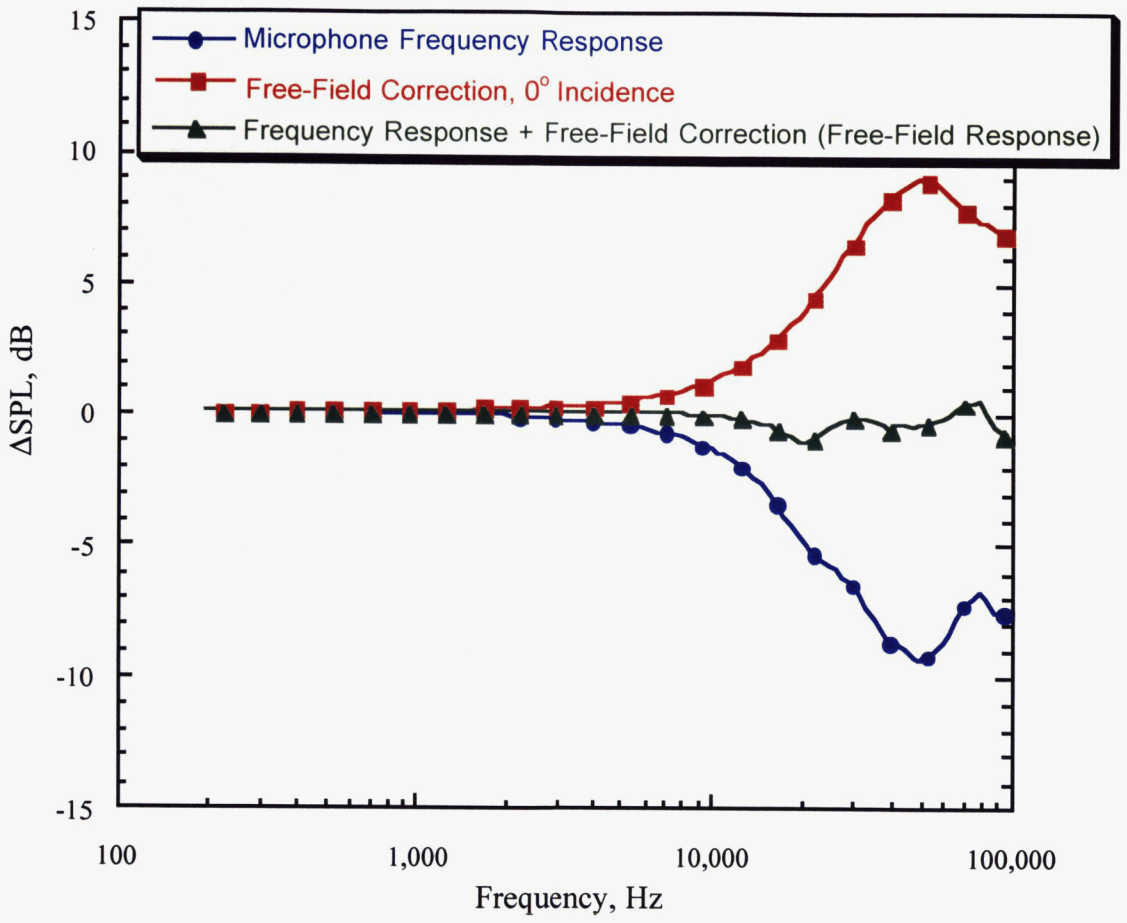

Figure B.1 Manufacturer specified corrections for microphone response.
(B & K Specifications sheet for 4939 type microphones)

interested in referring to B & K literature. Notice that when the frequency response (electrostatic actuator pressure response) and the free-field correction (free-field correction, 0^{o} incidence, without protection grid) are added together, the correction applied to the data is less than 1 dB over most of the frequency range (the final correction is referred to as the free-field response, 0^{o} incidence, without protection grid).

B & K does not provide an actual grid correction, but curves for the combined frequency response and free-field correction (free-field response, with and without protection grid) are provided. These curves are shown in Figure B.2. Note that the grid changes the response appreciably at high frequencies. This is the curve used to correct the data for the current experiments. Technically, there is an individual curve for each microphone. However, upon investigation it was found that these curves varied only minutely from microphone to microphone. Also, since another correction was applied to correct older microphones to a 'true' microphone signal there was little need to apply the individual corrections to the data. The differences are automatically taken into account when this correction is applied.

There is an important point that should be noted. These curves are provided from B & K in 1/12 octave bands. According to B & K this is not an issue since the curve was developed using tones, which have amplitudes independent of bandwidth. Although this is true, when applying the curve to data in a different bandwidth, the most common practice is to simply curve fit the B & K data and apply the fit at the frequencies in the data of interest. There is technically not a problem with this method. The problem arises when the data is converted to a different bandwidth. The final result can be different depending on whether the correction is applied before or after the bandwidth conversion. If the correction is constant over the different bandwidths the correction is not affected by the conversion. However, if the correction varies over the bandwidth, the correction will produce different results when applied before or after the conversion. For example, if 4 small bands are being converted into 1 large band, the correction must be constant over the entire frequency range of the large band. Otherwise the correction will not produce a band-independent result. Admittedly, these differences are minor in this case since the variation of the correction is smooth and not large, and actually in most cases the difference would be much less than other uncertainties. Even in

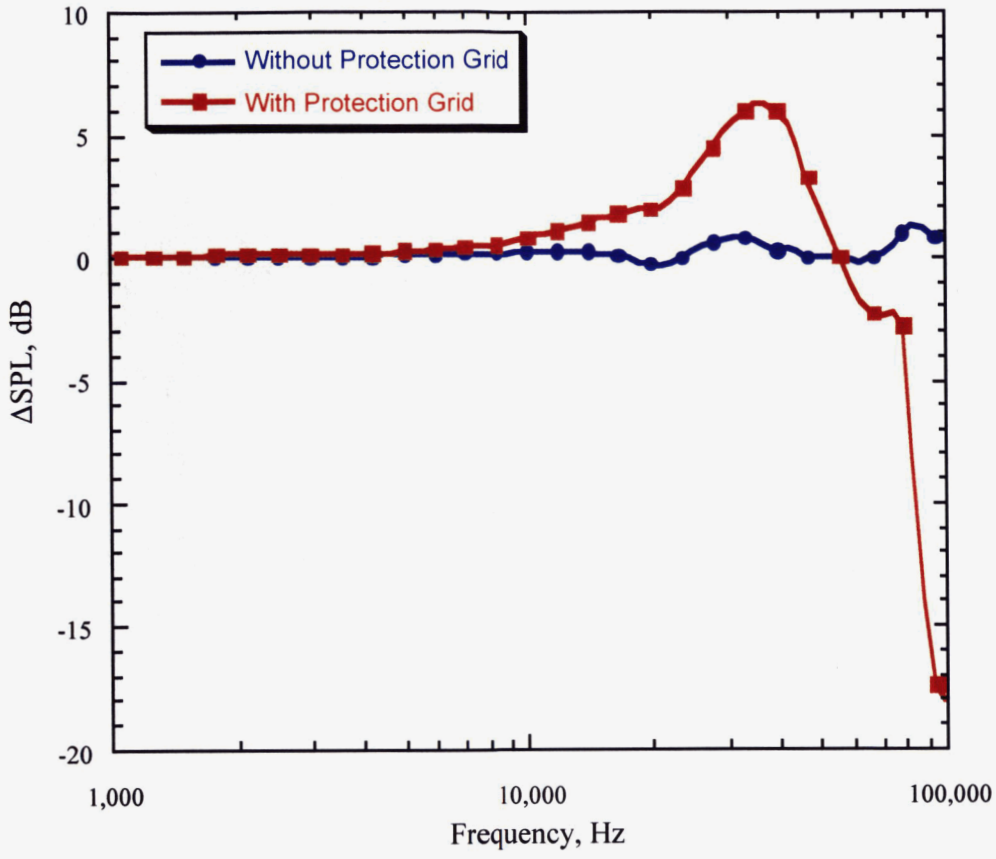

Figure B2 Manufacturer specified corrections for microphone response with and without protection grid (B & K Specifications sheet for 4939 type microphones).

this case where the grid correction has about a 5 dB change, the differences are only minor and at high frequencies and occur only where the slope of the correction is large. However, there are other corrections that are not as minor as in the case of the random incidence response. This curve has larger corrections and higher slopes.

Thus, even though the difference was minor in this case, the power spectral density (PSD) was deemed the most appropriate bandwidth for applying the correction. All data was converted to the 1 Hz bandwidth of the PSD before applying the correction. This was used as a standard for applying all the corrections that were frequency dependent. The only exception to this was the individual 'true' frequency response. The reasoning behind this will be discussed in the following section where that correction is described.

As mentioned the data was converted from the bandwidth in which it was acquired to the PSD. Since the data was acquired with a constant bandwidth it was a simple change based on the bandwidth. Each SPL value was adjusted and this amplitude was assigned to all the 1 Hz frequency points inside the band associated with the SPL value. Thus,

$$SPL_{psd}(f=i) = SPL_{psd}(f=i+1) = \ldots = SPL_{psd}(f=n) = SPL(f=k) - 10Log\left[\frac{\Delta f}{1}\right] \qquad \text{(B.2)}$$

where i is the lower limit and n is the upper limit of the k^{th} band in the data. For example, converting data with a 32 Hz bandwidth and looking at the band centered at 64 Hz. In the equation above i = 48, n = 80 and k = 64. Normally this would not be an appropriate conversion since mostly like the Df of the data is larger than 1 Hz. However it is appropriate here since the data is converted back to its original bandwidth. Thus, the correction is applied at a standard bandwidth, yet it is never implied that the data has the same resolution and is converted back to its appropriate resolution. The correction provided by B & K is fit to a 1 Hz bandwidth, which is appropriate because the curve was produced using tones which does make the curve itself independent of bandwidth. This correction is then added to the PSD data as follows:

$$SPL_{B\&K} = SPL_{psd} + C_{free\_field+grid} \qquad \text{(B.3)}$$

noting that all three terms in the equations are functions of frequency and the addition is similar to array addition where the correction value for each frequency is added to the SPL for the same frequency. Once the correction is applied, the data is converted back to its original bandwidth.

Correction for Microphone Location.

Another simple correction that had to be made was the correction for distance between the jet exit and microphone location (R). Typically this can be done by using the R^2 law. In the far field of a point source the amplitude decays as a function of the square of the distance between the source and the measurement location. This is due to spherical spreading of the sound energy. In a jet, it is assumed that there is a distribution of incoherent point sources. In this case, the same relationship applies because the sources are incoherent and hence will superimpose without creating an interference pattern of constructive and destructive interference. Thus, as long as the microphone is located in the acoustic far-field of the jet, the amplitude can be adjusted by the R^2 law to account for different R between configurations. All data in this report were corrected to a 12 ft. radius as shown in equation (B.4)

$$SPL_R = SPL \; -20Log\left[\frac{R}{12}\right] \qquad \text{(B.4)}$$

Correction Due to Atmospheric Absorption

As with the correction for R in the previous section, the correction due to atmospheric absorption is more for standardizing the data rather than correcting data due to microphone response. As sound travels from the source to the observation location some sound will be absorbed by the air it passes through. This is dependent on the atmospheric pressure, temperature and humidity as well as the distance traveled. There are several corrections that can be used to account for this absorption. The correction used in the current experiments is based on ANSI S1.26-1995 presents a standard method for calculating the absorption of sound by the atmosphere. Equations for a correction as a function of frequency, pressure, temperature, and humidity are given in the documentation. The correction is based on a 1000 m distance between the observer and the source, however the variation with distance is linear. Figure B.3 shows sample corrections for 3 different humidity values at P = 14.7 and T = 90 °F. The equations were programmed into the post-processing code for the data. Since this is also a correction where the results could be

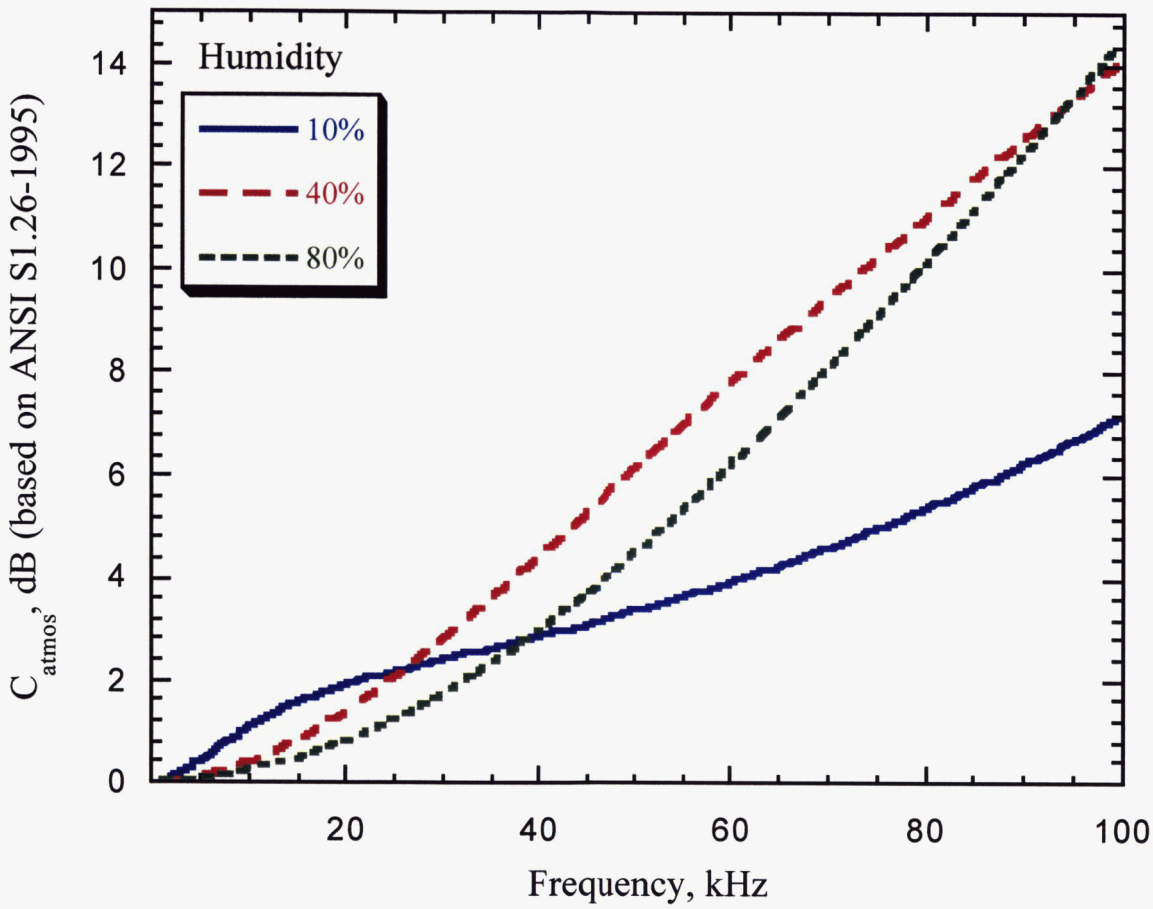

Figure B.3 Sample atmospheric absorption correction based on ANSI S1.26-1995 (P = 14.7 psia, T = 90° F)

changed depending on the bandwidth in which it is applied, the atmospheric correction was added into the data at the PSD level. The correction was then added to the raw data signal as follows

$$SPL_{atm} = SPL_{PSD} + C_{atm}\frac{R}{1000(3.28)} \tag{B.5}$$

The correction was applied to each angle at for each test point based on the test point conditions. The 3.28 is in the equation only as a conversion factor for the distance since R is in feet and the correction is /1000m.

Summary of Corrections applied to Acoustic Data.

Several corrections were applied to the acoustic data that were obtained in the present experiments. The main goal of the corrections was to standardize the data in such a way that it could be compared with data of other experiments. Thus it is essential that all the facility- and atmospheric-specific characteristics be removed from the data. These include microphone-dependent frequency response, standard corrections for the free-field and microphone protection grid, amplifier settings, microphone distance, and varying atmospheric conditions. Some of these corrections are dependent on the bandwidth in which the correction is applied. In order to standardize the correction process, the data was reduced to a PSD level and these corrections were applied at a standard 1 Hz bandwidth. The other corrections that are not bandwidth dependent were applied at the same bandwidth as the raw data.

Appendix C: 1/3-Octave Band Spectra

This appendix includes 1/3-Octave band spectral comparisons of the noise of the DE nozzle and the round nozzle, both of the same effective exit area. All SPL's are in decibels.

Comparison of DE Nozzle to Round Nozzle

1/3-Octave Spectra

R = 12 ft

$\Phi = 90^{o}$

SPL corrected for atmospheric absorption, microphone protection grid and pressure/free-field response

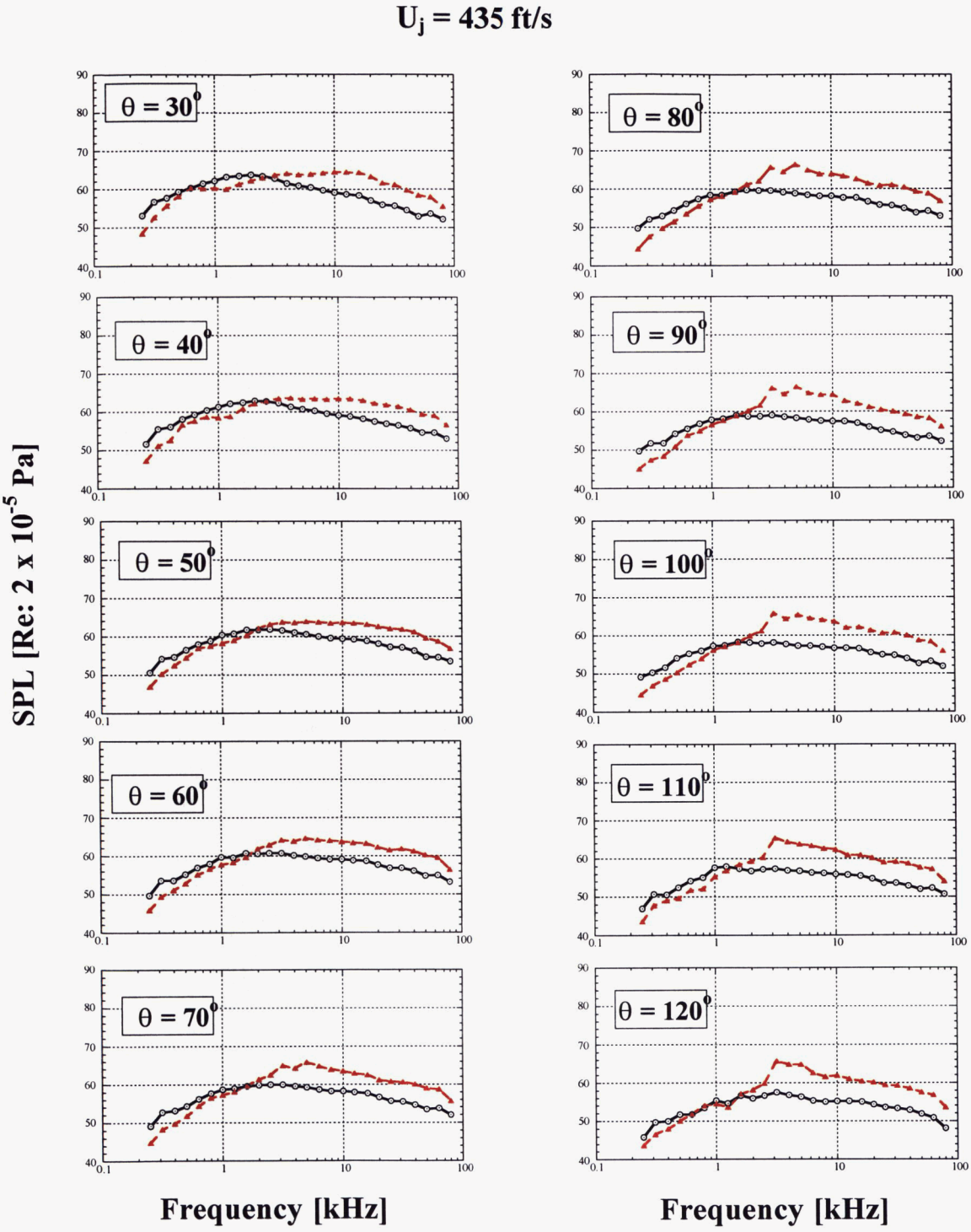

Figure C1. Comparison of $^1/_3$-octave band farfield spectra; $\phi = 90^o$; R = 12 ft; $P_{Tj}/P_{amb} = 1.116$; $U_j/a_o = 0.39$; $T_{Tj}/T_{amb} = 0.80$;

○ Baseline 1.6-inch Circular Nozzle ▲ Distributed Exhaust Nozzle

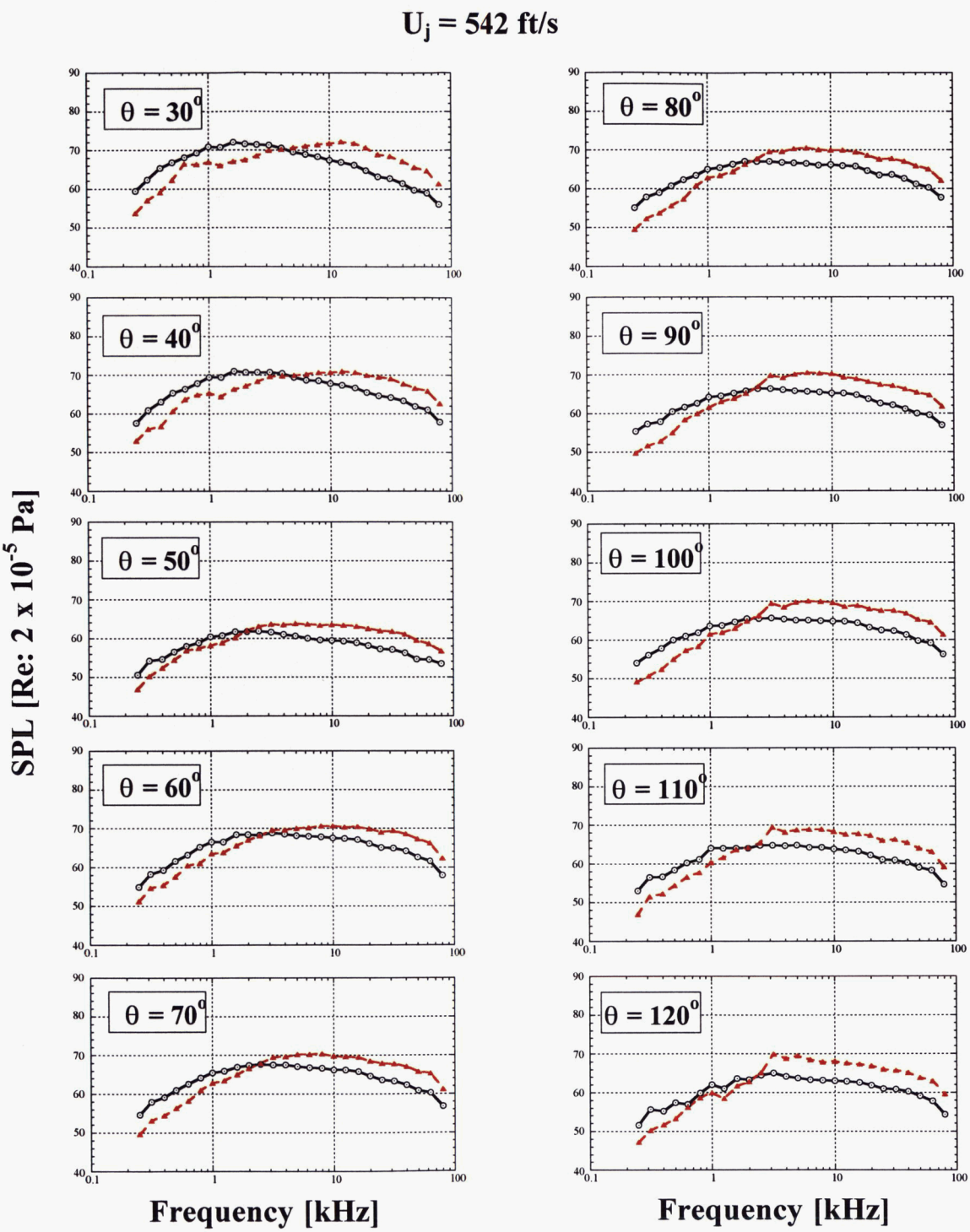

Figure C2. Comparison of $^1/_3$-octave band farfield spectra; $\phi = 90^o$; R = 12 ft;

$P_{Tj}/P_{amb} = 1.188$; $U_j/a_o = 0.49$; $T_{Tj}/T_{amb} = 0.80$;

⊙ Baseline 1.6-inch Circular Nozzle ▲ Distributed Exhaust Nozzle

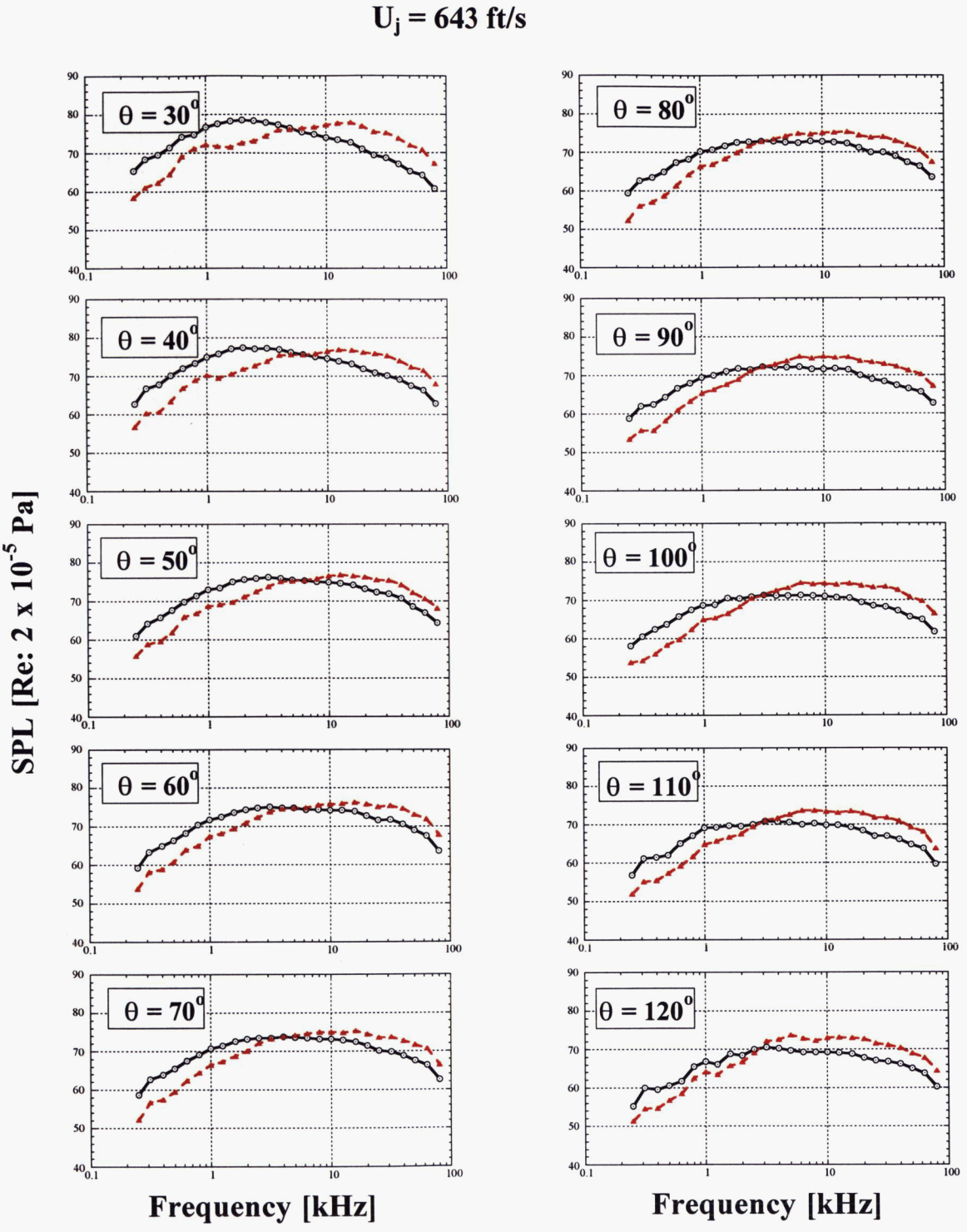

Figure C3. Comparison of $^1/_3$-octave band farfield spectra; $\phi = 90^o$; R = 12 ft; $P_{Tj}/P_{amb} = 1.278$; $U_j/a_o = 0.58$; $T_{Tj}/T_{amb} = 0.80$;

Baseline 1.6-inch Circular Nozzle Distributed Exhaust Nozzle

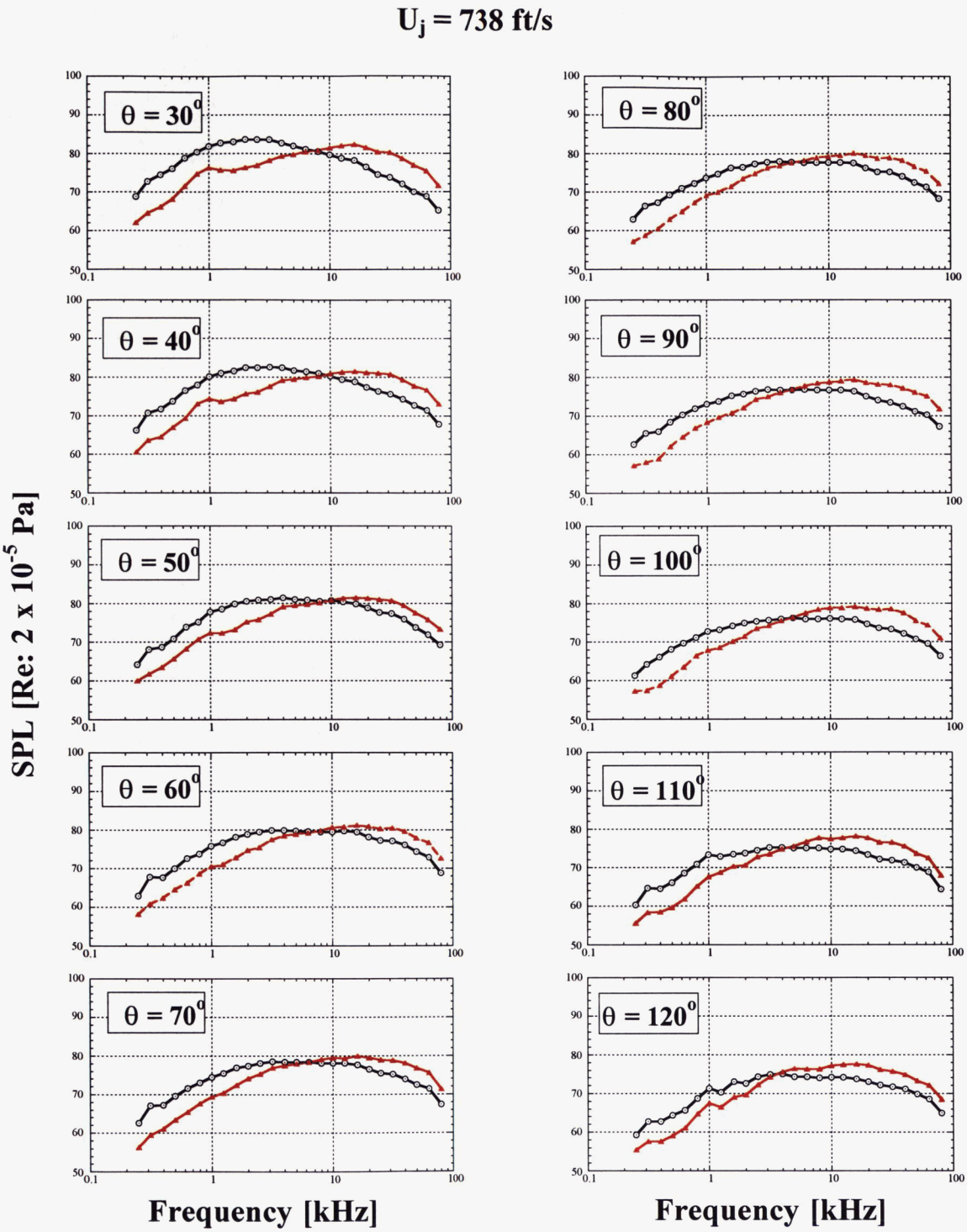

Figure C4. Comparison of $^1/_3$-octave band farfield spectra; $\phi = 90^o$; R = 12 ft; $P_{Tj}/P_{amb} = 1.388$; $U_j/a_o = 0.66$; $T_{Tj}/T_{amb} = 0.80$;

⊙ Baseline 1.6-inch Circular Nozzle ▲ Distributed Exhaust Nozzle

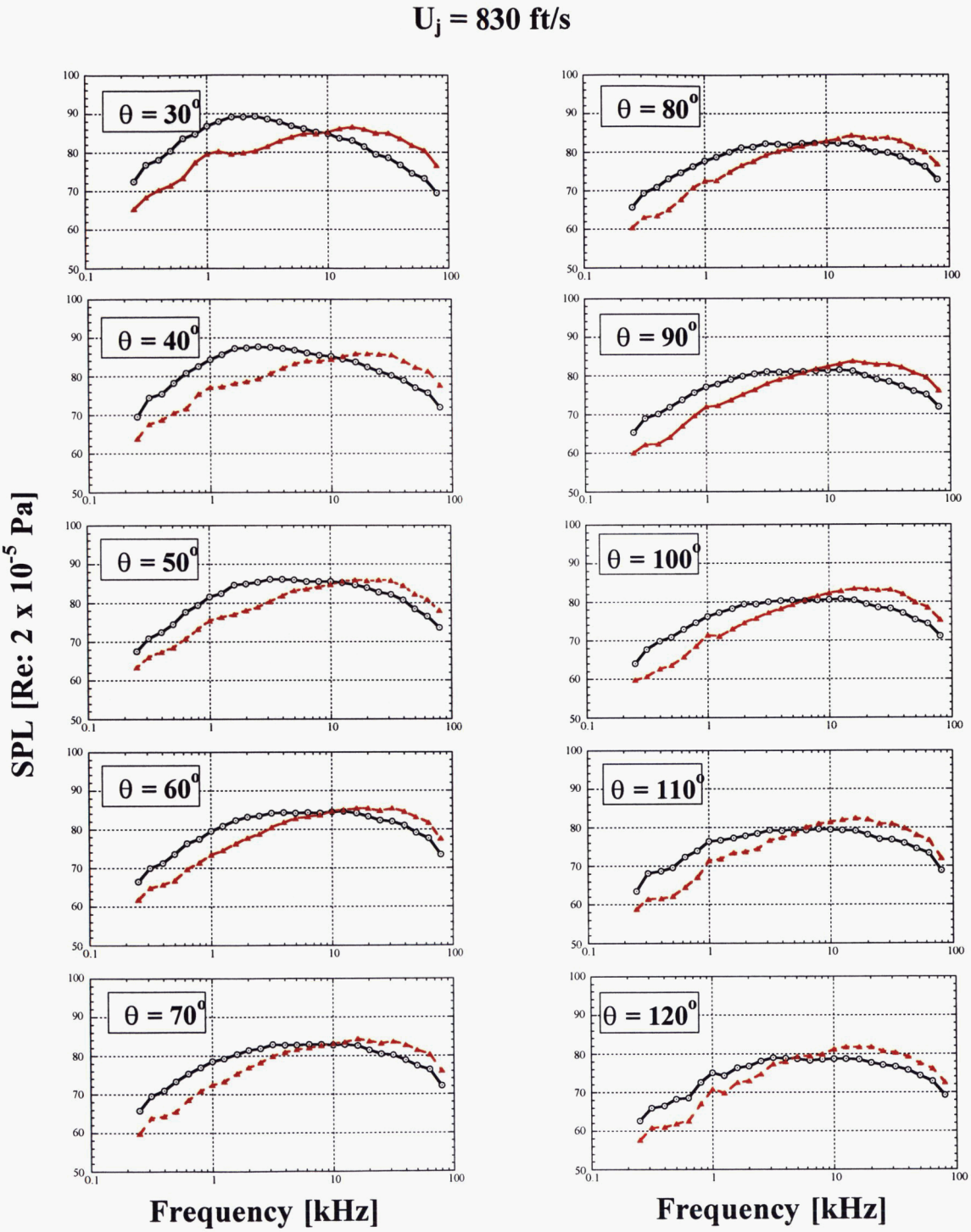

Figure C5. Comparison of $^1/_3$-octave band farfield spectra; $\phi = 90^o$; R = 12 ft; $P_{Tj}/P_{amb} = 1.523$; $U_j/a_o = 0.74$; $T_{Tj}/T_{amb} = 0.80$;

⊙ Baseline 1.6-inch Circular Nozzle ▲ Distributed Exhaust Nozzle

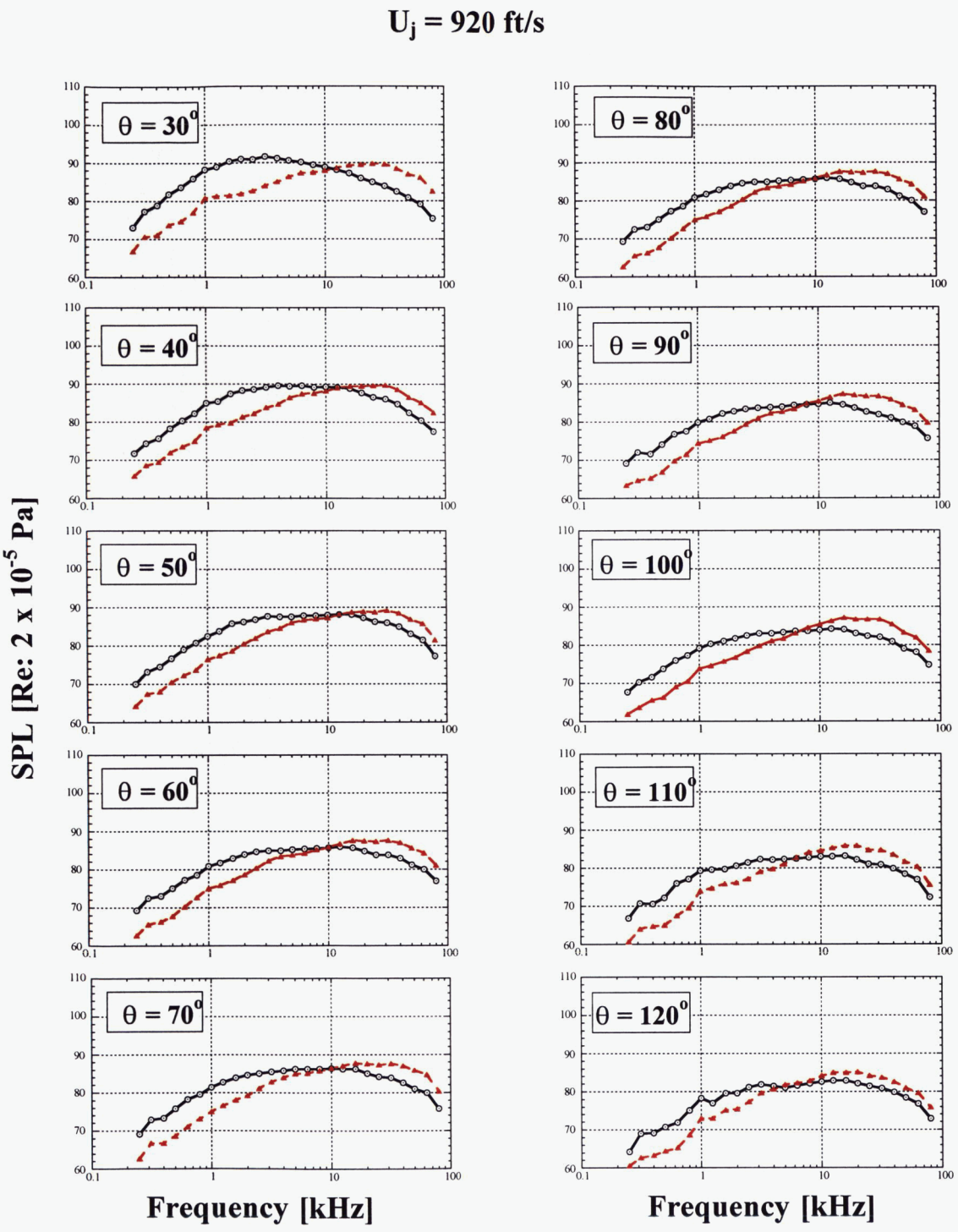

Figure C6. Comparison of $^{1}/_{3}$-octave band farfield spectra; $\phi = 90^{o}$; R = 12 ft; $P_{Tj}/P_{amb} = 1.691$; $U_j/a_o = 0.83$; $T_{Tj}/T_{amb} = 0.80$;

⊙ Baseline 1.6-inch Circular Nozzle ▲ Distributed Exhaust Nozzle

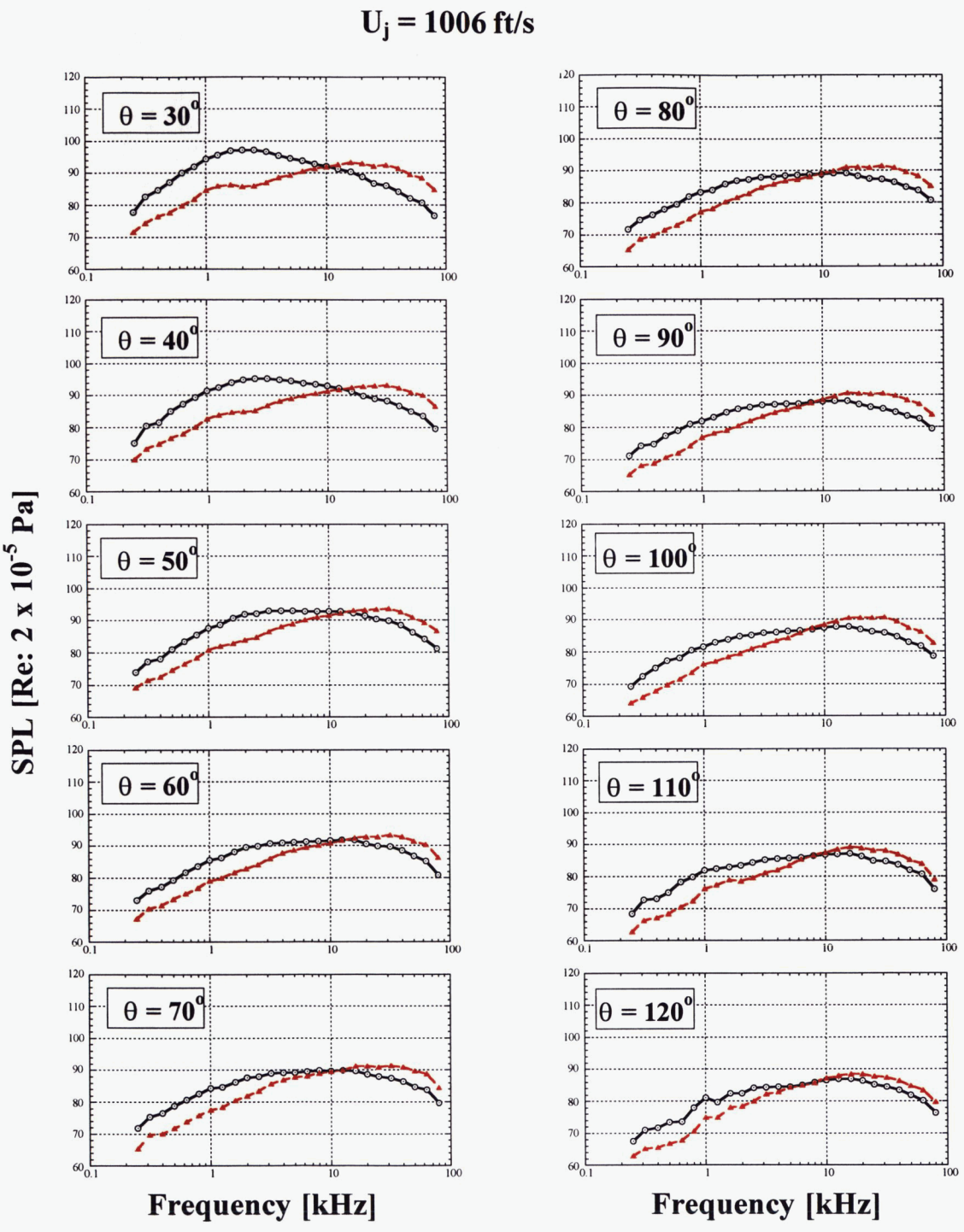

Figure C7. Comparison of $^1/_3$-octave band farfield spectra; $\phi = 90^o$; R = 12 ft;

$P_{Tj}/P_{amb} = 1.895$; $U_j/a_o = 0.90$; $T_{Tj}/T_{amb} = 0.80$;

⊙ Baseline 1.6-inch Circular Nozzle ▲ Distributed Exhaust Nozzle

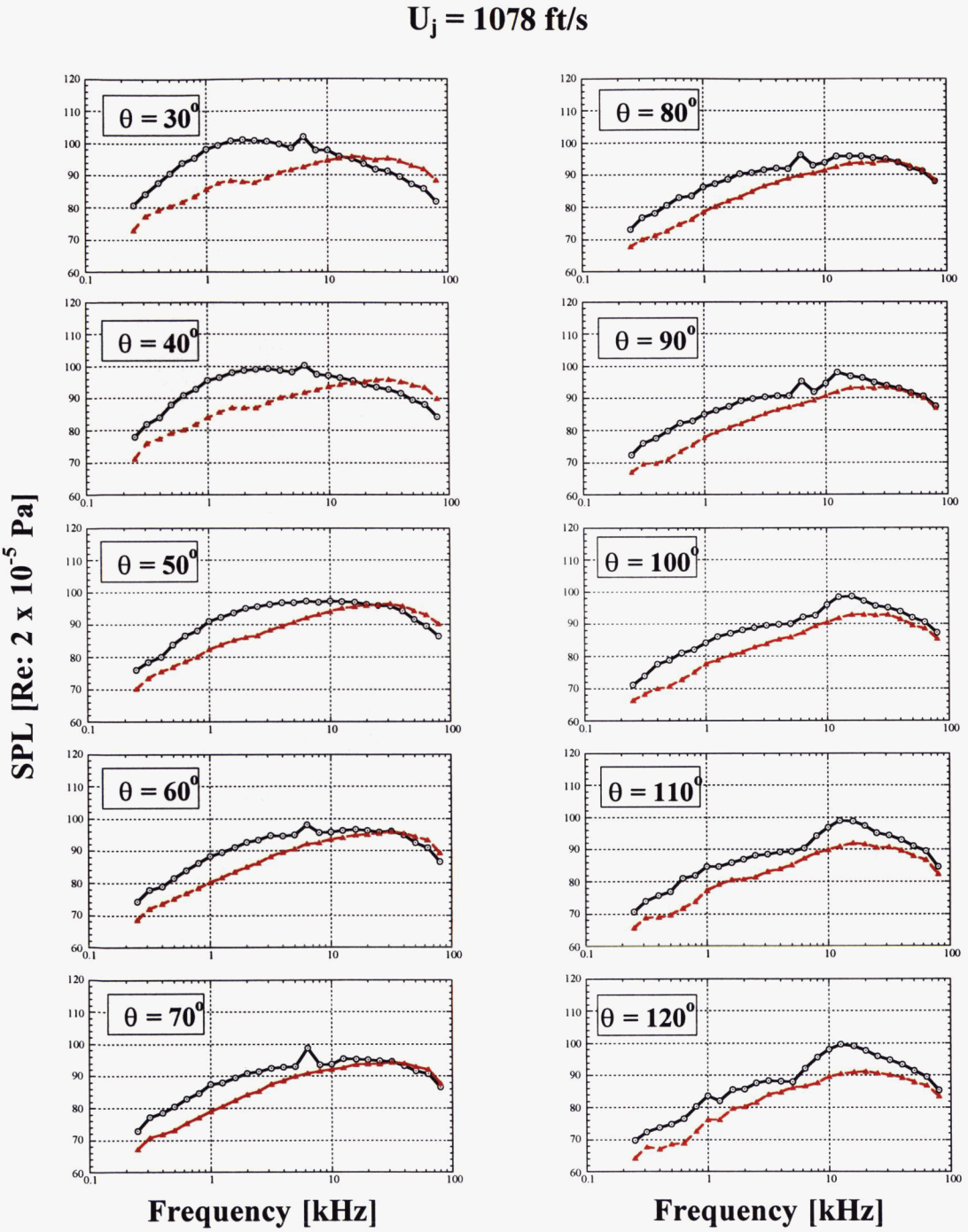

Figure C8. Comparison of $^1/_3$-octave band farfield spectra; $\phi = 90^o$; R = 12 ft; Δf = 32 Hz;

P_{Tj}/P_{amb} = 2.106; U_j/a_o = 0.97; T_{Tj}/T_{amb} = 0.80;

⊙ Baseline 1.6-inch Circular Nozzle ▲ Distributed Exhaust Nozzle

$U_j = 1159$ ft/s

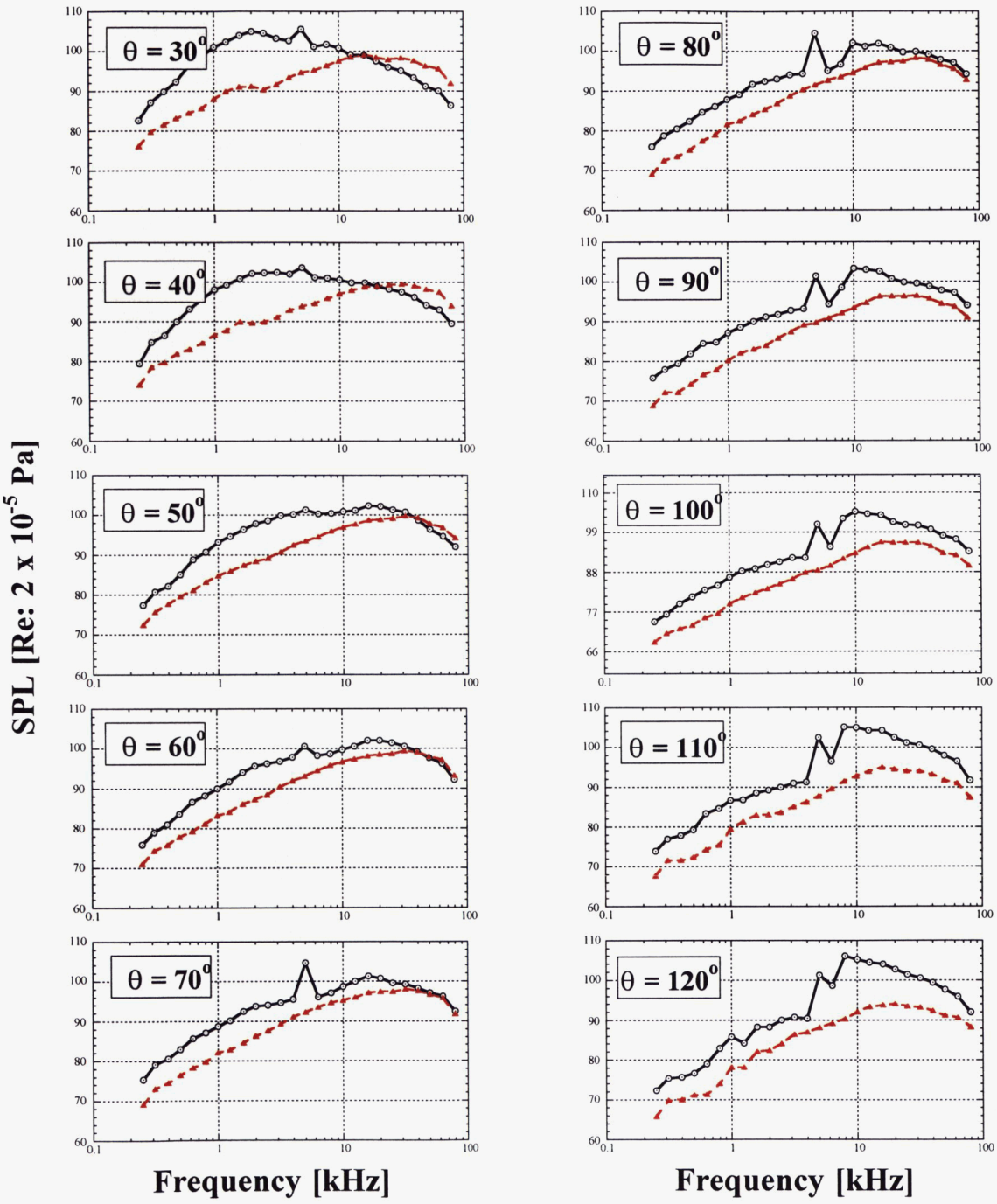

Figure C9. Comparison of $^1/_3$-octave band farfield spectra; $\phi = 90^o$; R = 12 ft;

$P_{Tj}/P_{amb} = 2.402$; $U_j/a_o = 1.04$; $T_{Tj}/T_{amb} = 0.80$;

⊙ Baseline 1.6-inch Circular Nozzle ▲ Distributed Exhaust Nozzle

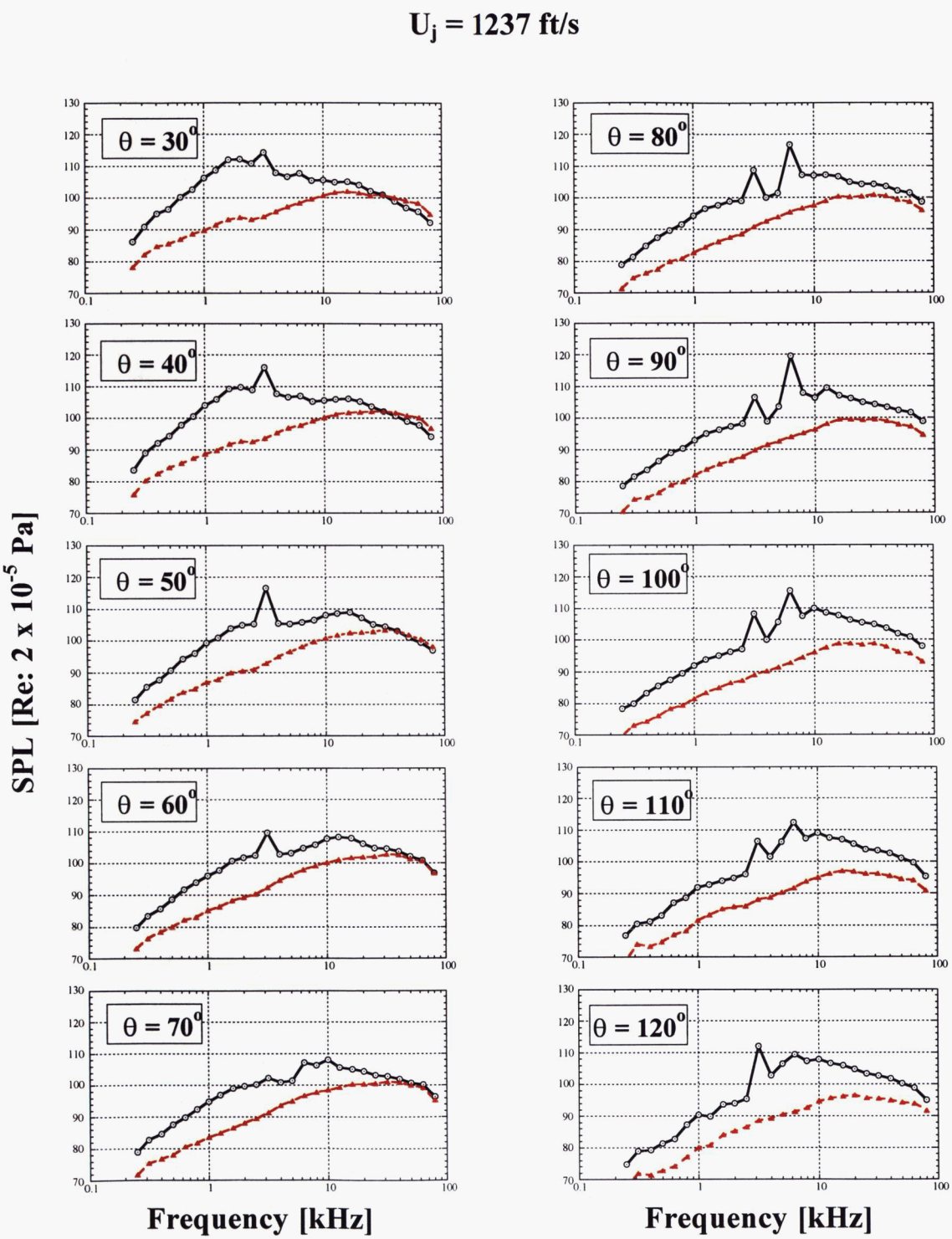

Figure C10. Comparison of $^1/_3$-octave band farfield spectra; $\phi = 90^o$; R = 12 ft; $P_{Tj}/P_{amb} = 2.767$; $U_j/a_o = 1.11$; $T_{Tj}/T_{amb} = 0.80$;

⊙ Baseline 1.6-inch Circular Nozzle ▲ Distributed Exhaust Nozzle

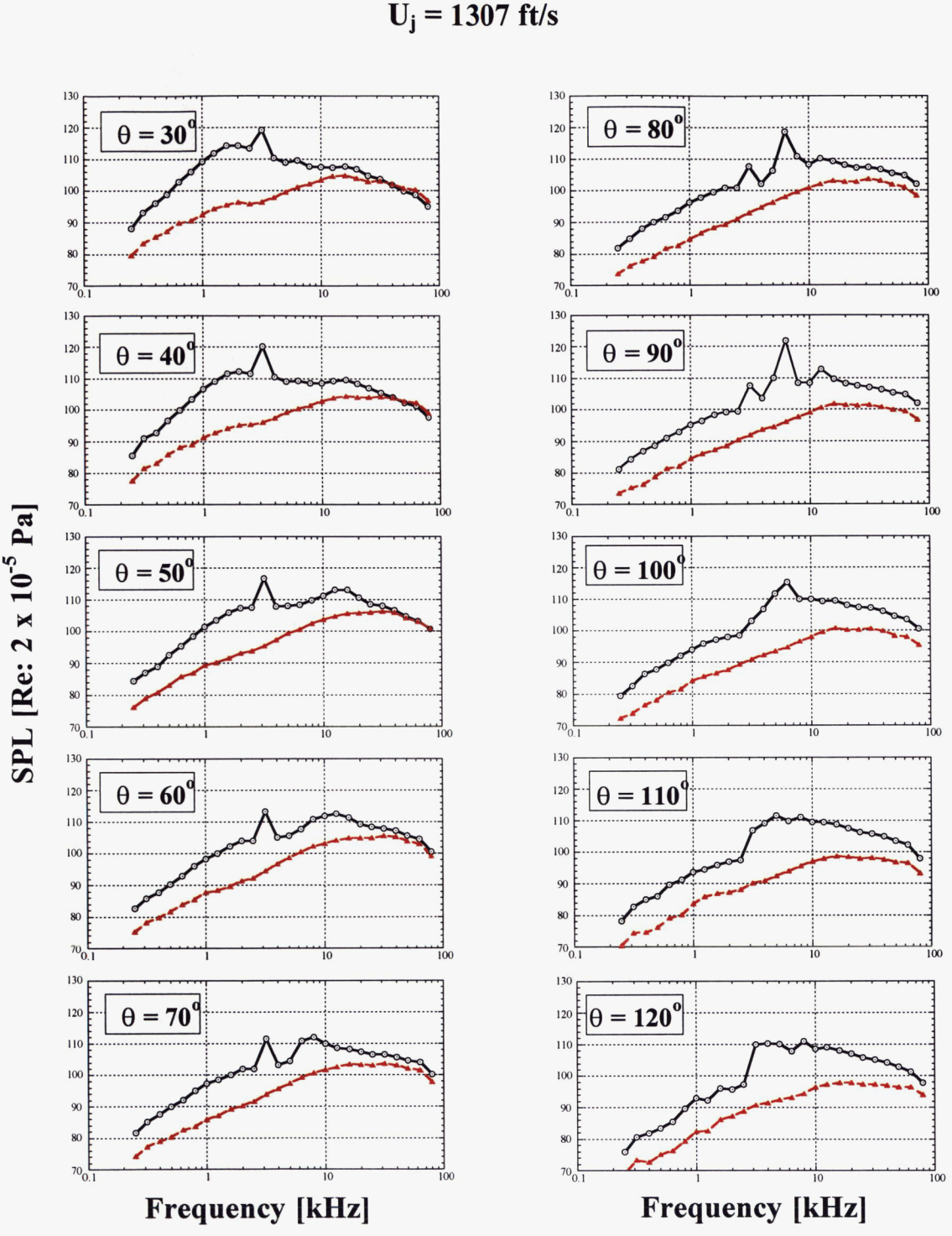

Figure C11. Comparison of $^{1}/_{3}$-octave band farfield spectra; $\phi = 90^{o}$; R = 12 ft; $P_{Tj}/P_{amb} = 3.180$; $U_j/a_o = 1.17$; $T_{Tj}/T_{amb} = 0.80$;

⊙ Baseline 1.6-inch Circular Nozzle ▲ Distributed Exhaust Nozzle

Comparison of DE Nozzle to Round Nozzle

1/3-Octave Spectra

R = 12 ft

$\Phi = 30^{o}$

SPL corrected for atmospheric absorption, microphone protection grid and pressure/free-field response

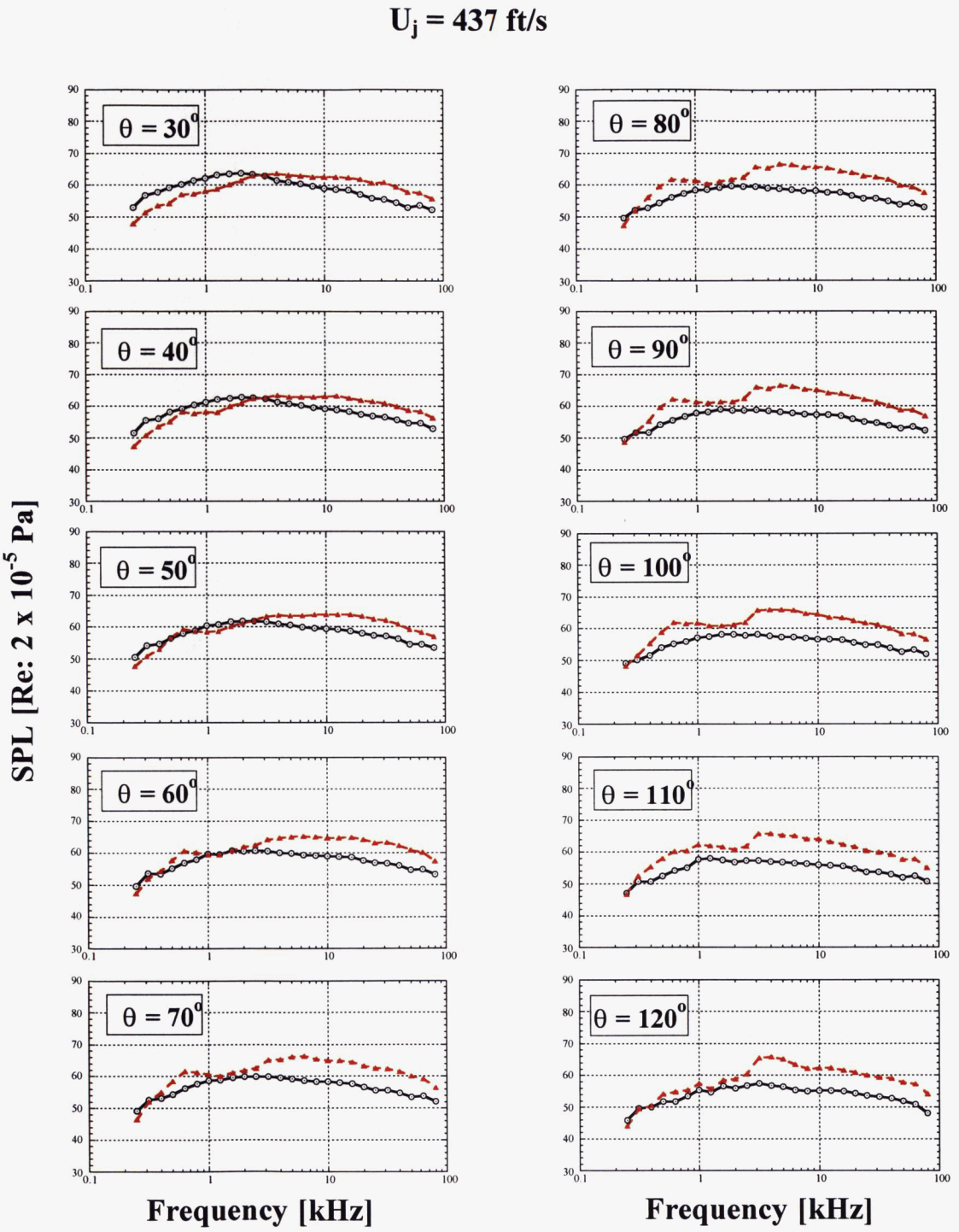

Figure C12. Comparison of $^1/_3$-octave band farfield spectra; $\phi = 30^o$; R = 12 ft; $P_{Tj}/P_{amb} = 1.115$; $U_j/a_o = 0.39$; $T_{Tj}/T_{amb} = 0.80$;

⊙ Baseline 1.6-inch Circular Nozzle ▲ Distributed Exhaust Nozzle

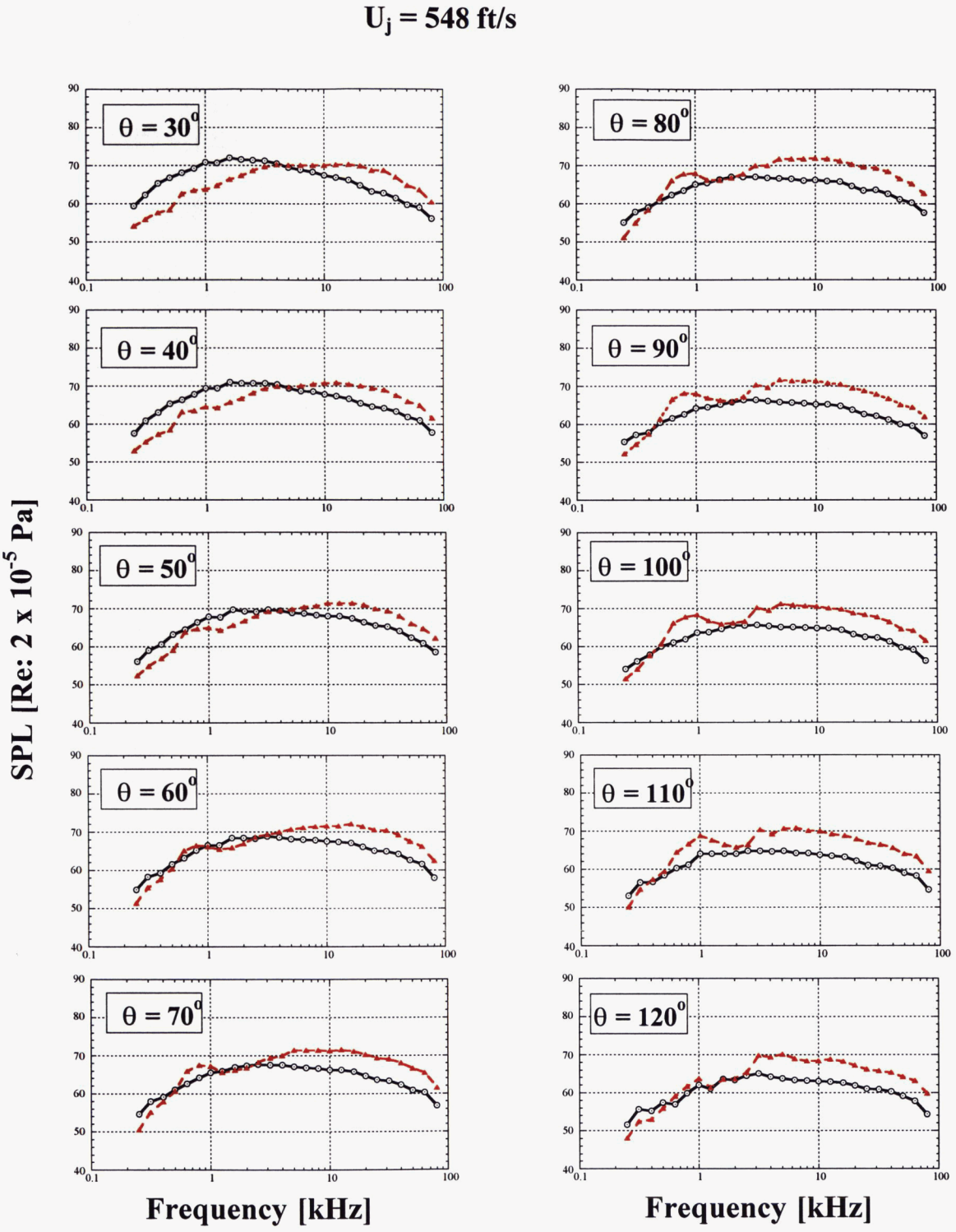

Figure C13. Comparison of $^1/_3$-octave band farfield spectra; $\phi = 30^o$; R = 12 ft; $P_{Tj}/P_{amb} = 1.187$; $U_j/a_o = 0.49$; $T_{Tj}/T_{amb} = 0.80$;

⊙ Baseline 1.6-inch Circular Nozzle ▲ Distributed Exhaust Nozzle

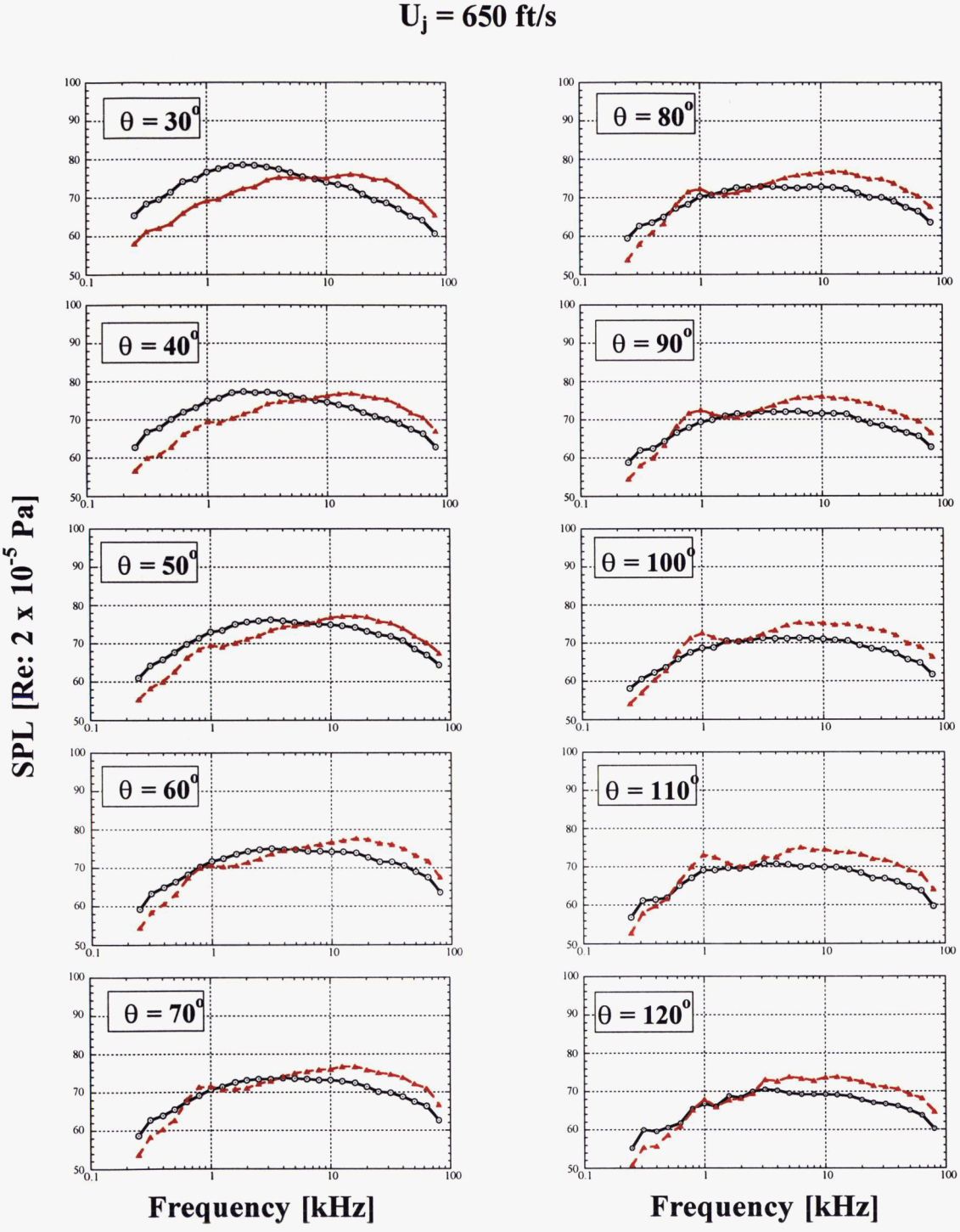

Figure C14. Comparison of $^{1}/_{3}$-octave band farfield spectra; $\phi = 30^{o}$; R = 12 ft; $P_{Tj}/P_{amb} = 1.277$; $U_j/a_o = 0.58$; $T_{Tj}/T_{amb} = 0.80$;

⊙ Baseline 1.6-inch Circular Nozzle ▲ Distributed Exhaust Nozzle

$U_j = 744$ ft/s

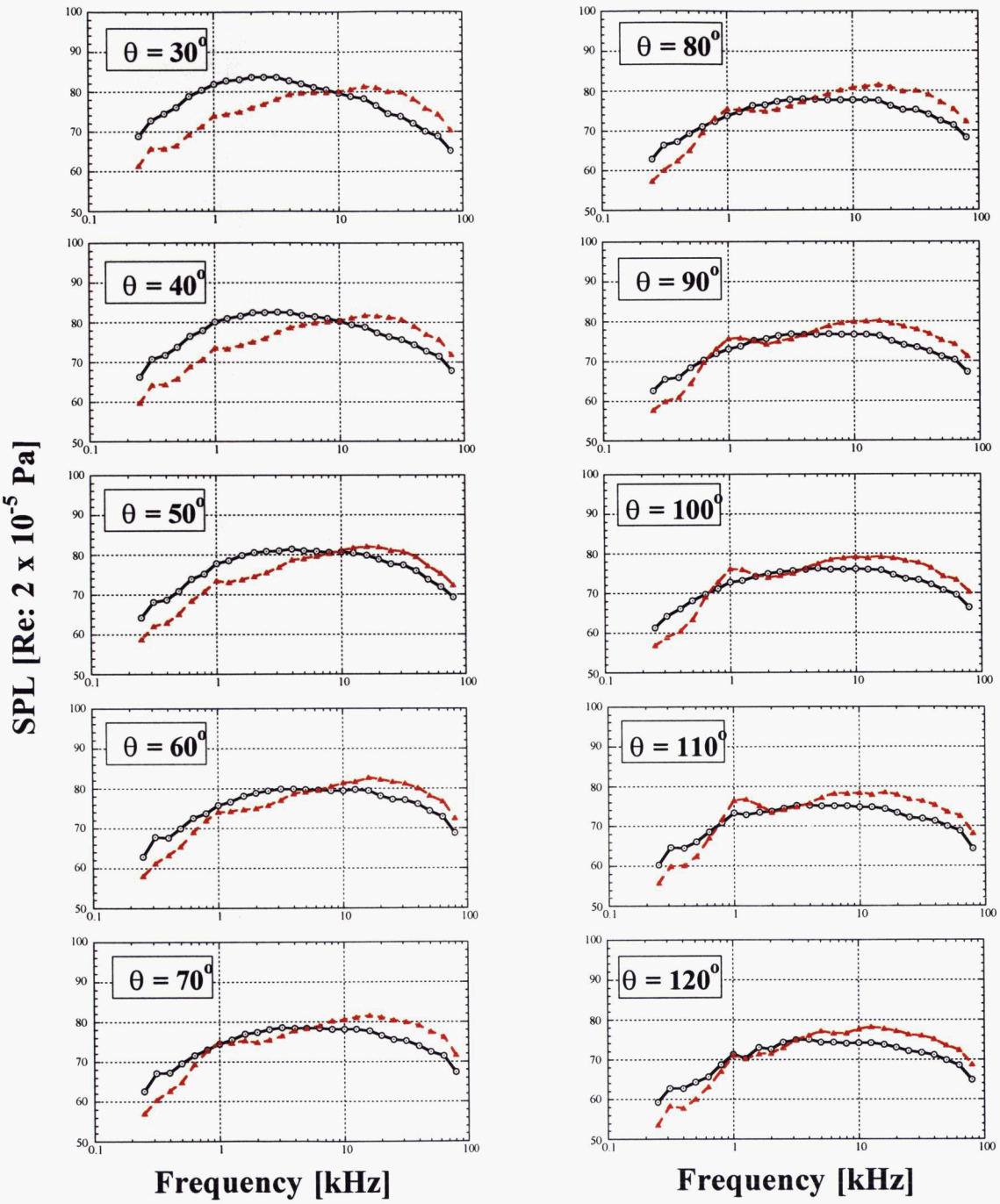

Figure C15. Comparison of $^1/_3$-octave band farfield spectra; $\phi = 30^o$; R = 12 ft; $P_{Tj}/P_{amb} = 1.387$; $U_j/a_o = 0.66$; $T_{Tj}/T_{amb} = 0.80$;

⊙ Baseline 1.6-inch Circular Nozzle ▲ Distributed Exhaust Nozzle

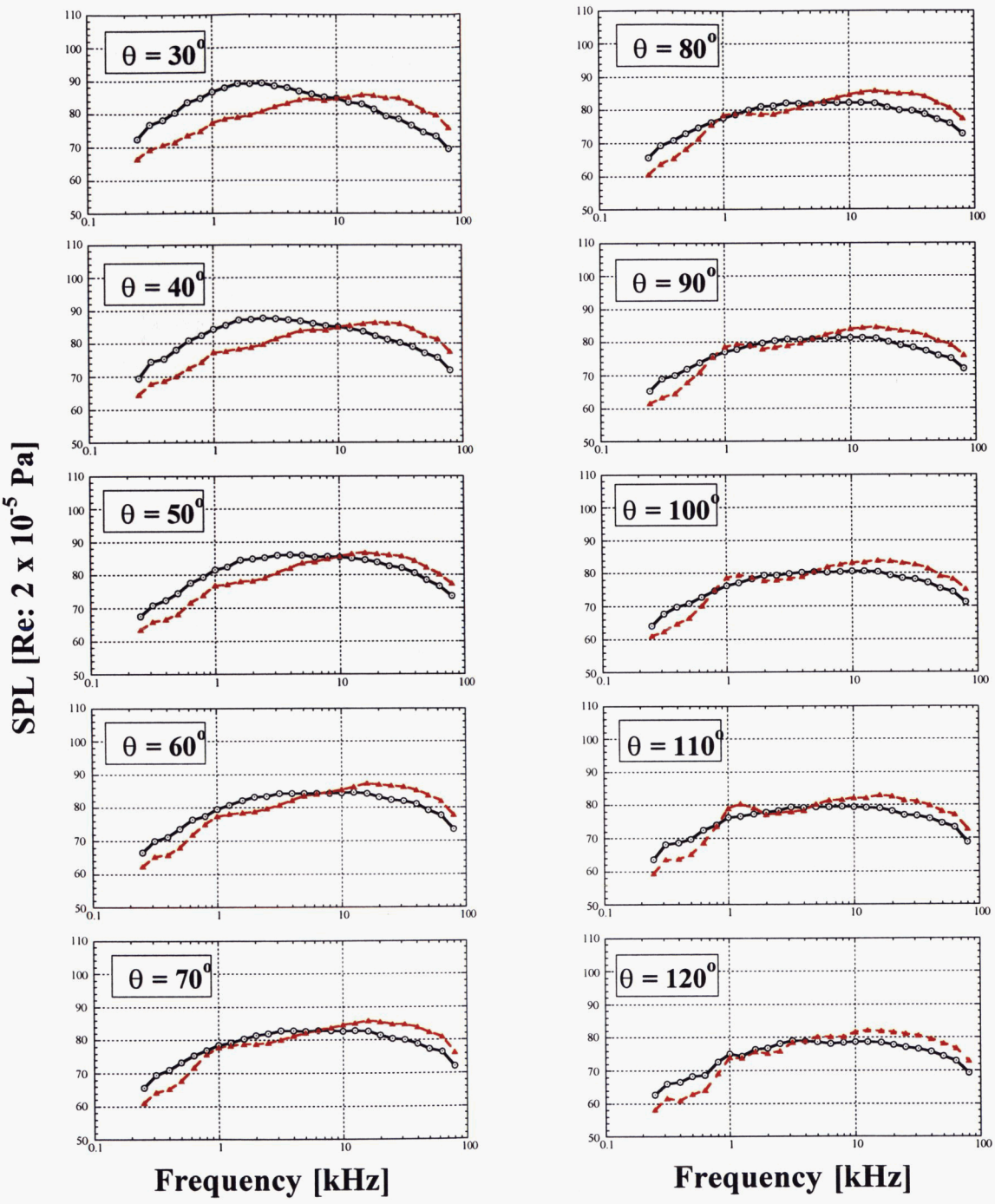

Figure C16. Comparison of $^1/_3$-octave band farfield spectra; $\phi = 30^o$; R = 12 ft; $P_{Tj}/P_{amb} = 1.544$; $U_j/a_o = 0.76$; $T_{Tj}/T_{amb} = 0.80$;

⊙ Baseline 1.6-inch Circular Nozzle ▲ Distributed Exhaust Nozzle

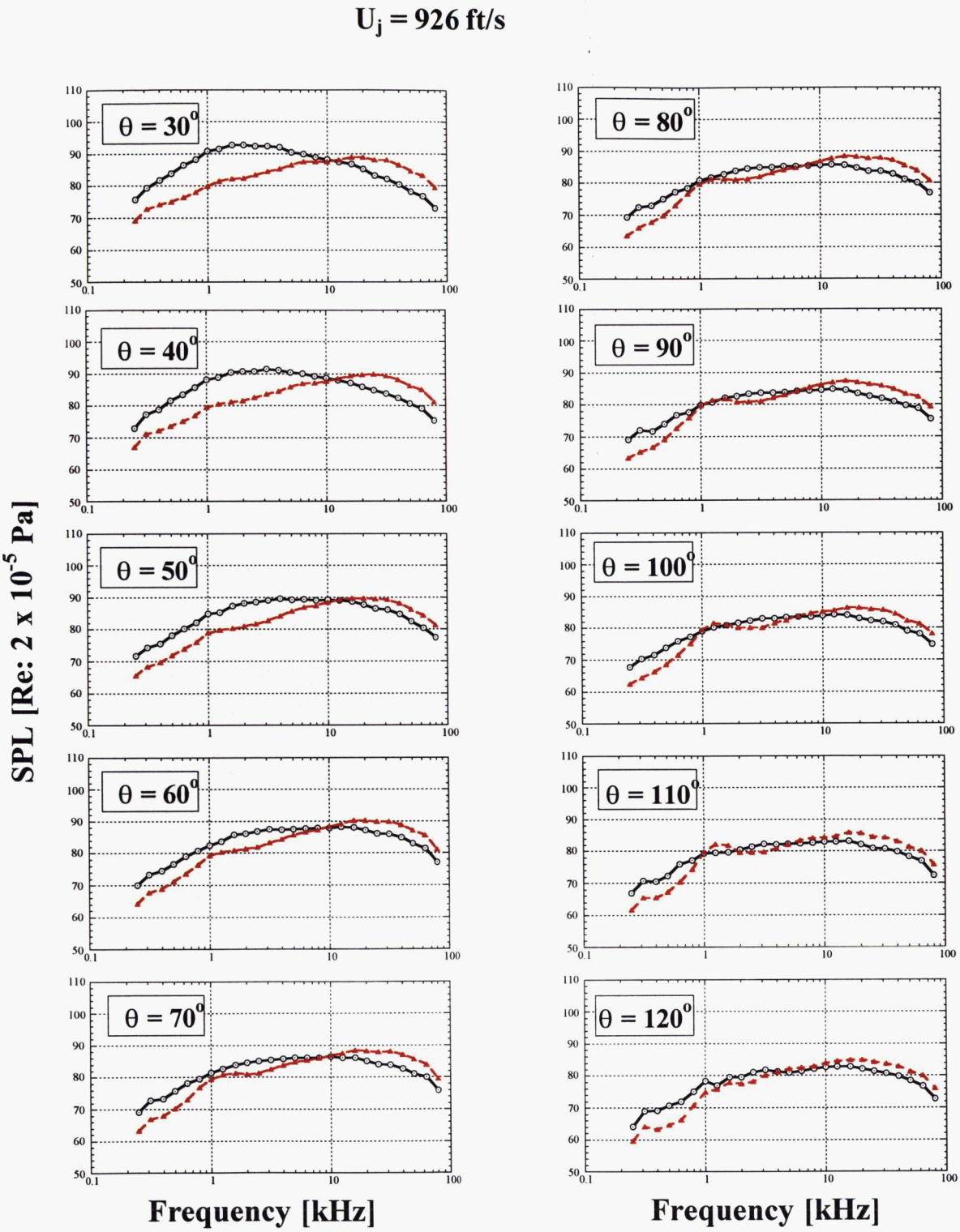

Figure C17. Comparison of $^1/_3$-octave band farfield spectra; $\phi = 30^\circ$; R = 12 ft;

$P_{Tj}/P_{amb} = 1.689$; $U_j/a_o = 0.83$; $T_{Tj}/T_{amb} = 0.80$;

⊙ Baseline 1.6-inch Circular Nozzle ▲ Distributed Exhaust Nozzle

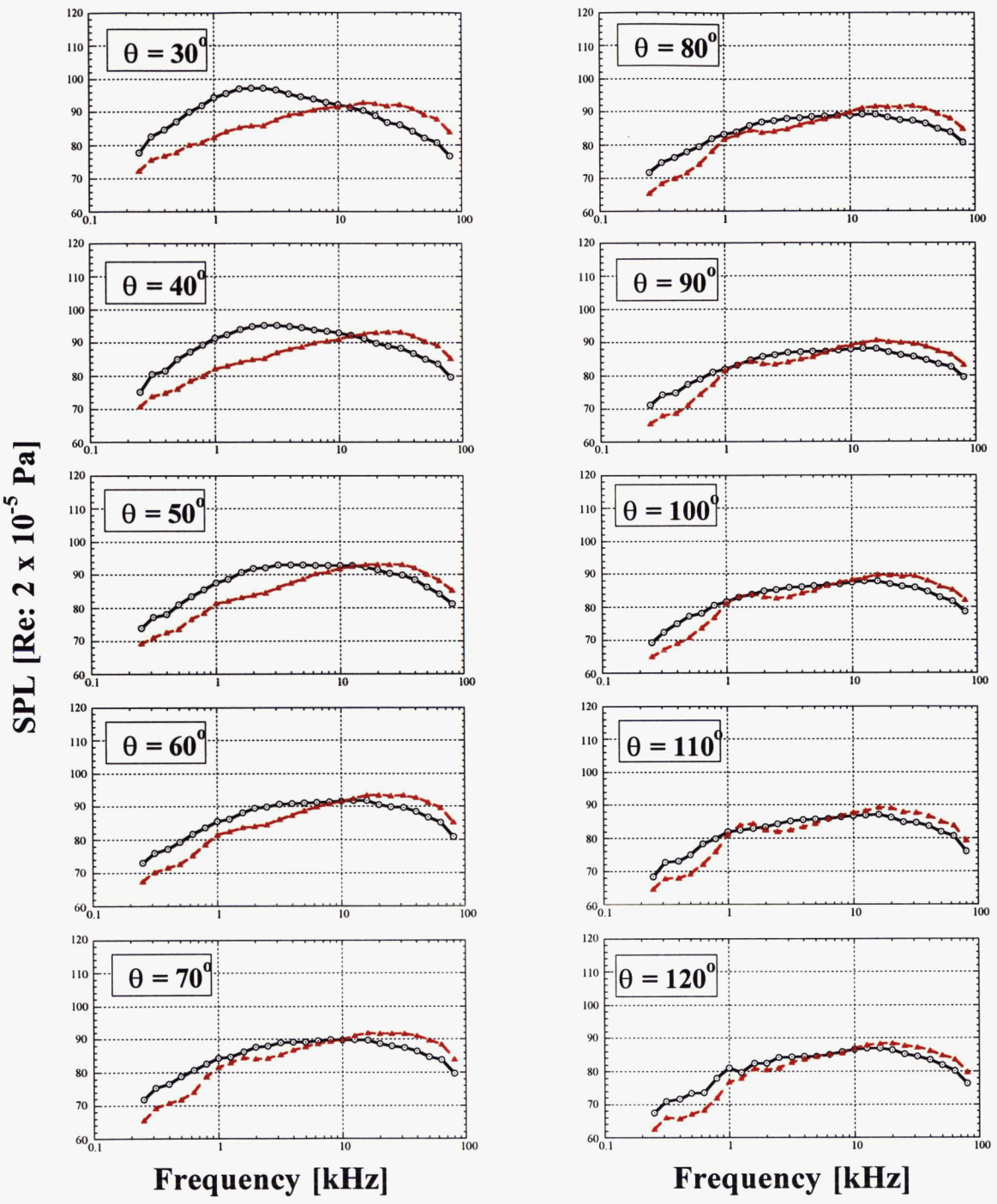

Figure C18. Comparison of $^1/_3$-octave band farfield spectra; $\phi = 30^o$; R = 12 ft; $P_{Tj}/P_{amb} = 1.895$; $U_j/a_o = 0.90$; $T_{Tj}/T_{amb} = 0.80$;

⊙ Baseline 1.6-inch Circular Nozzle ▲ Distributed Exhaust Nozzle

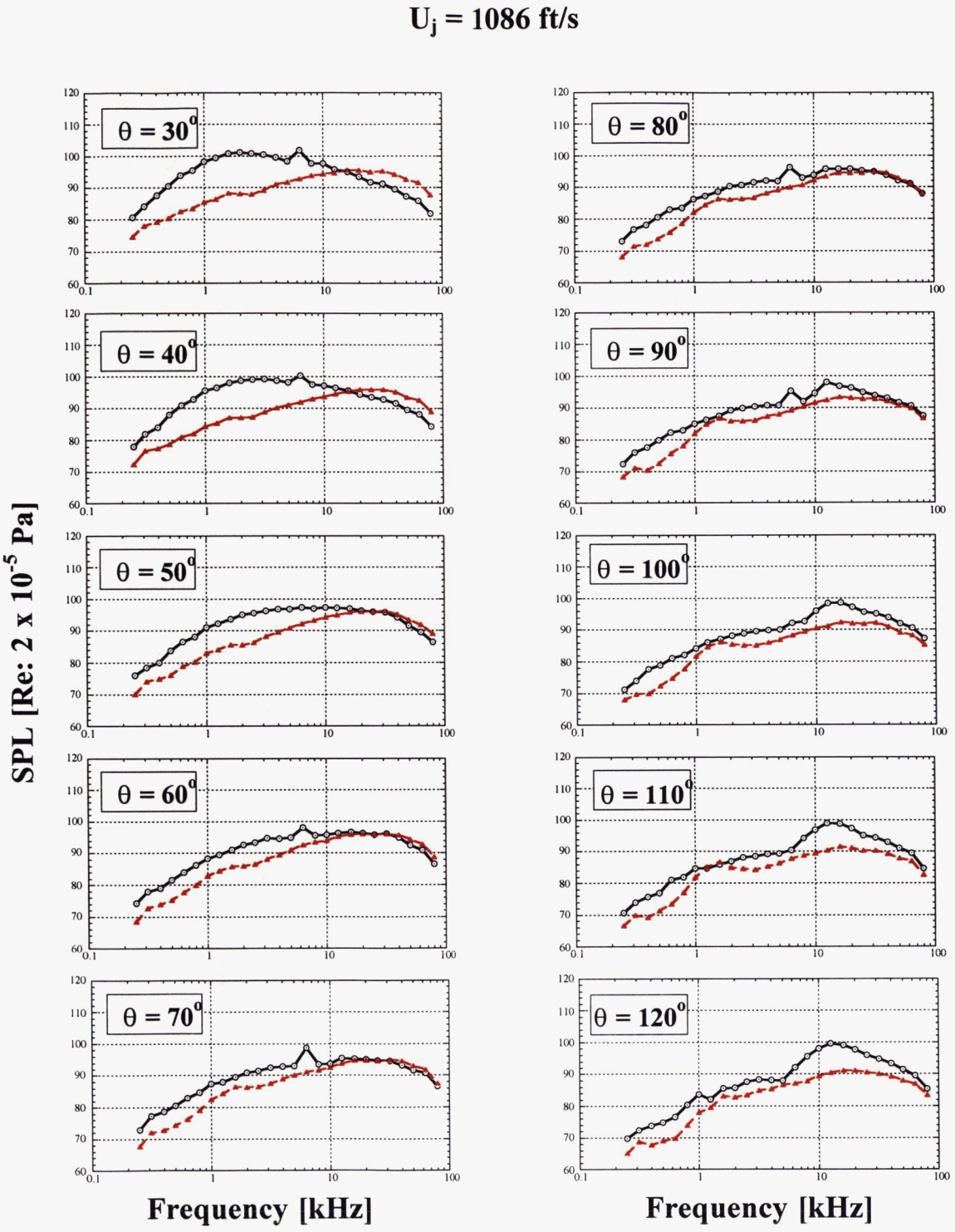

Figure C19. Comparison of $^1/_3$-octave band farfield spectra; $\phi = 30^o$; R = 12 ft; $P_{Tj}/P_{amb} = 2.109$; $U_j/a_o = 0.97$; $T_{Tj}/T_{amb} = 0.80$;

⊙ Baseline 1.6-inch Circular Nozzle ▲ Distributed Exhaust Nozzle

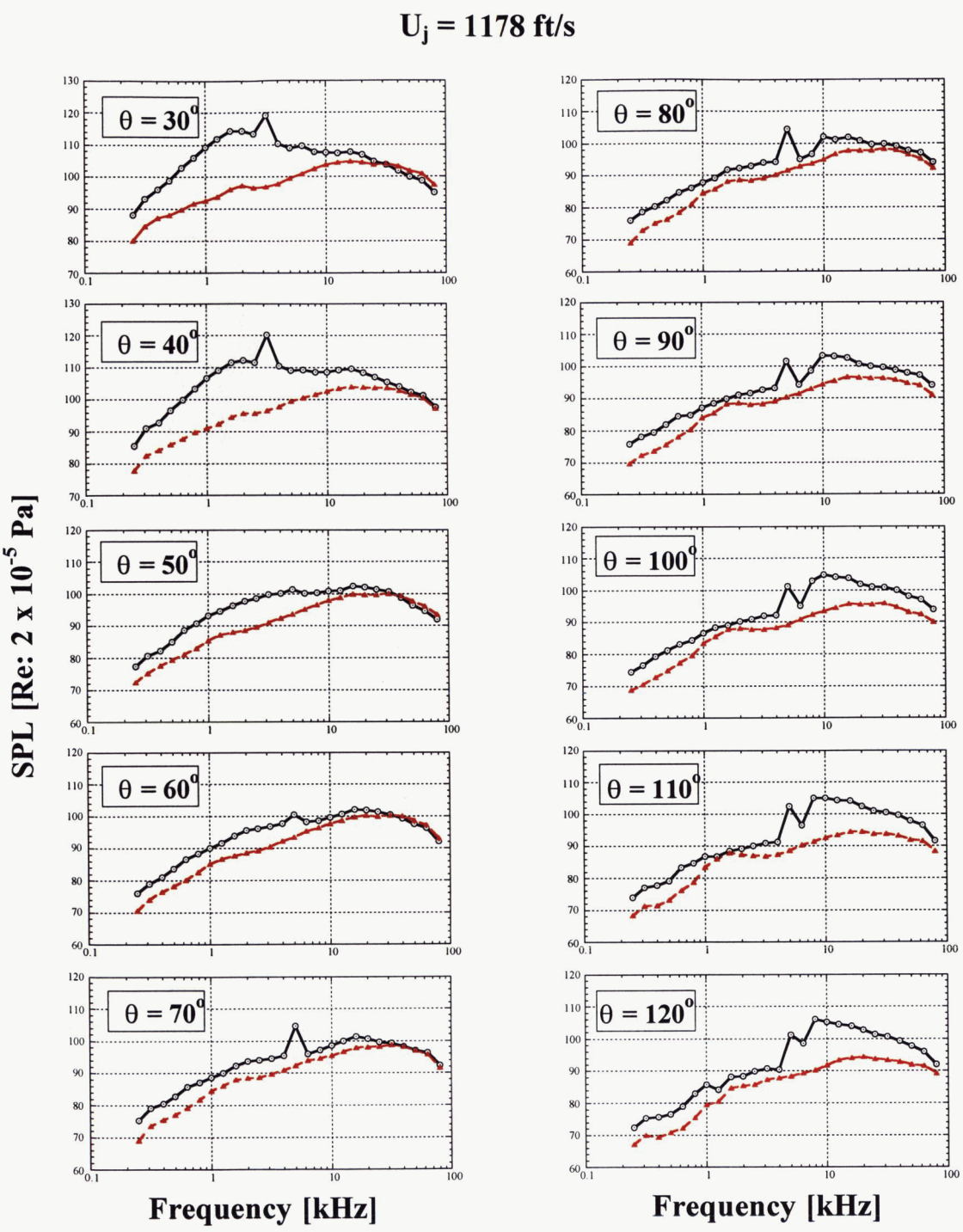

Figure C20. Comparison of $^1/_3$-octave band farfield spectra; $\phi = 30^o$; R = 12 ft;

$P_{Tj}/P_{amb} = 2.451$; $U_j/a_o = 1.05$; $T_{Tj}/T_{amb} = 0.80$;

⊙ Baseline 1.6-inch Circular Nozzle ▲ Distributed Exhaust Nozzle

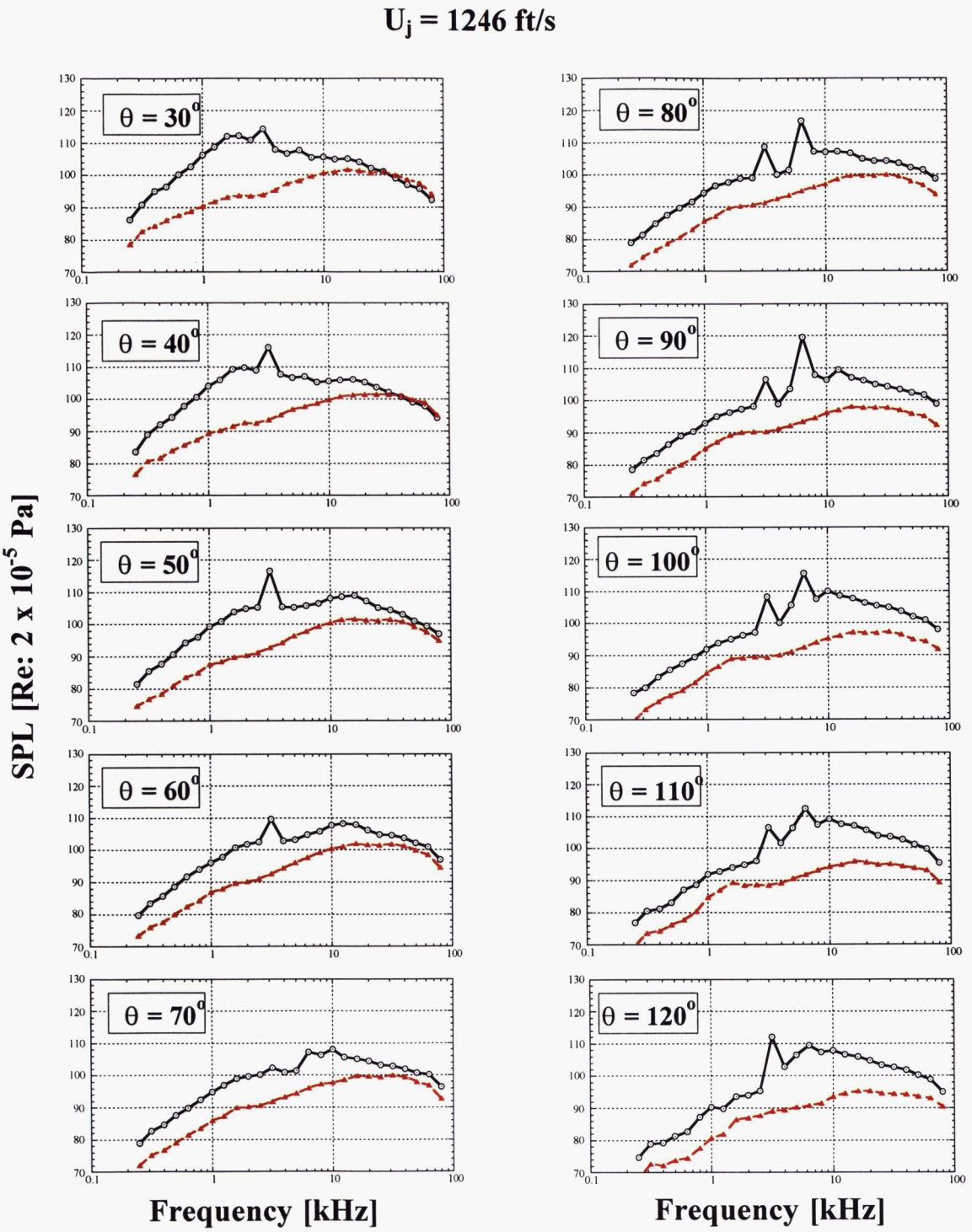

Figure C21. Comparison of $^1/_3$-octave band farfield spectra; $\phi = 30^o$; R = 12 ft; $P_{Tj}/P_{amb} = 2.770$; $U_j/a_o = 1.11$; $T_{Tj}/T_{amb} = 0.80$;

⊙ Baseline 1.6-inch Circular Nozzle ▲ Distributed Exhaust Nozzle

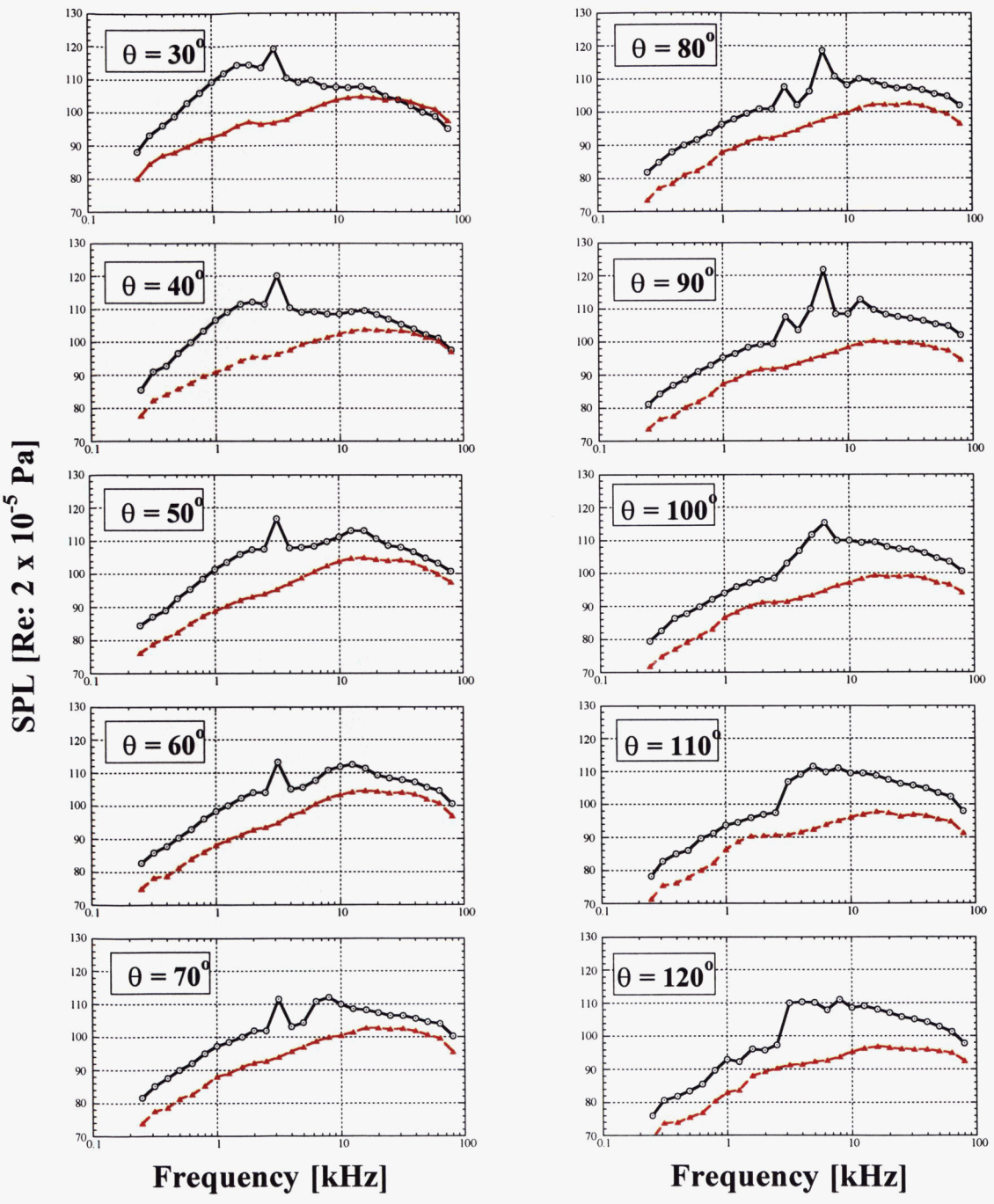

Figure C22. Comparison of $^1/_3$-octave band farfield spectra; $\phi = 30^o$; R = 12 ft; $P_{Tj}/P_{amb} = 3.197$; $U_j/a_o = 1.18$; $T_{Tj}/T_{amb} = 0.80$;

⊙ Baseline 1.6-inch Circular Nozzle ▲ Distributed Exhaust Nozzle

Comparison of DE Nozzle to Round Nozzle

1/3-Octave Spectra

R = 12 ft

$\Phi = 0^o$

SPL corrected for atmospheric absorption, microphone protection grid and pressure/free-field response

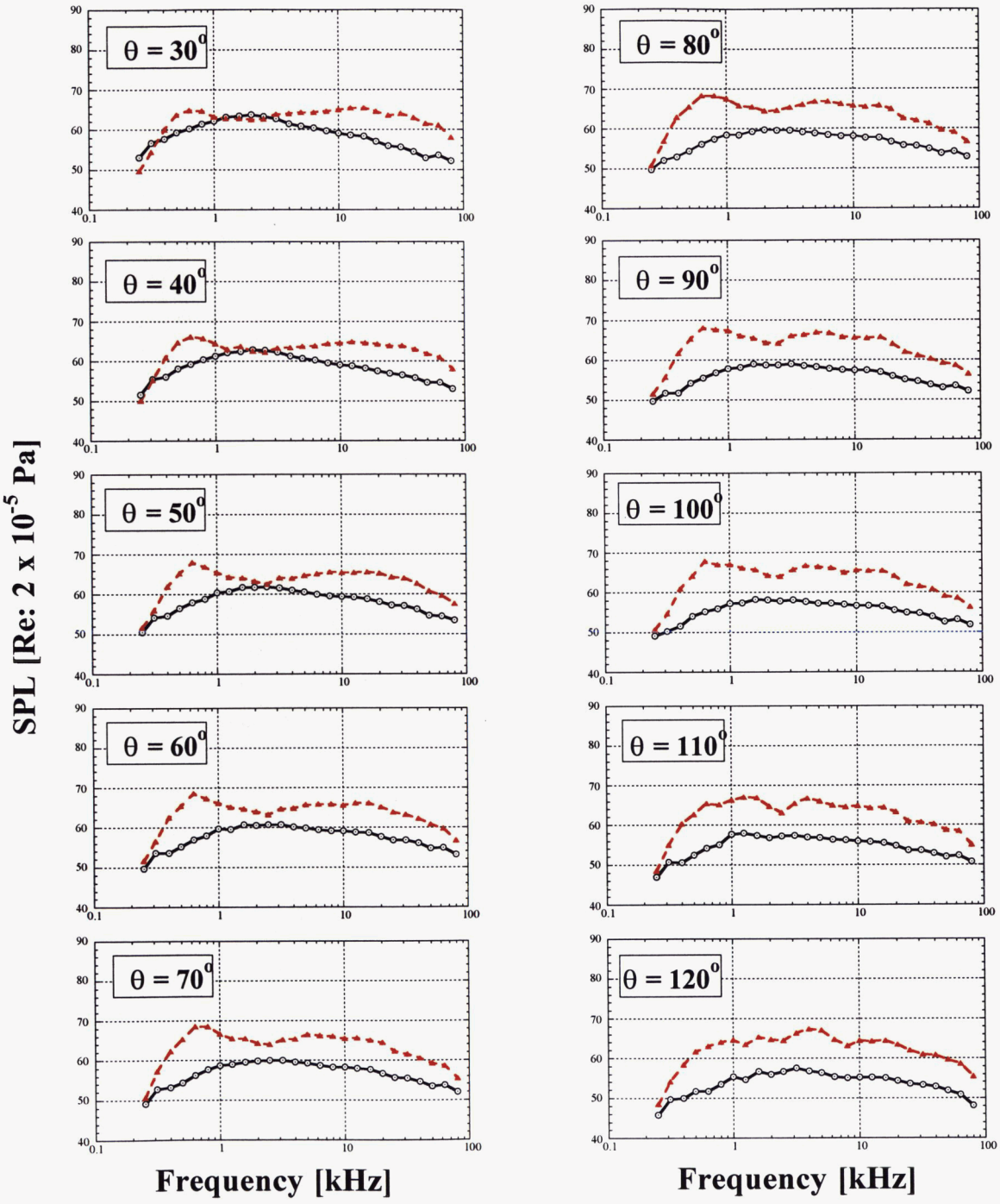

Figure C23. Comparison of $^1/_3$-octave band farfield spectra; $\phi = 0^o$; R = 12 ft;

$P_{Tj}/P_{amb} = 1.117$; $U_j/a_o = 0.39$; $T_{Tj}/T_{amb} = 0.80$;

⊙ Baseline 1.6-inch Circular Nozzle ▲ Distributed Exhaust Nozzle

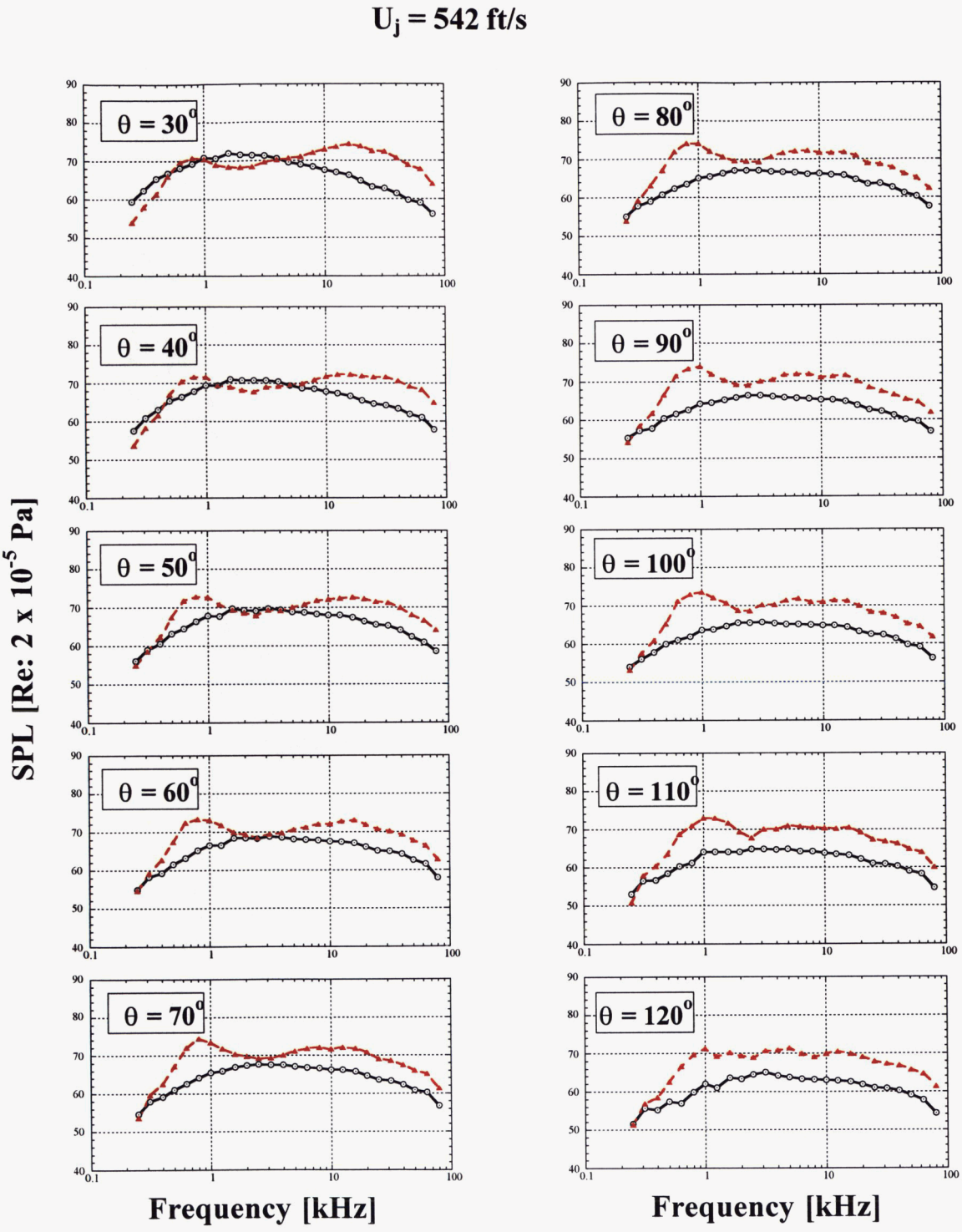

Figure C24. Comparison of $^1/_3$-octave band farfield spectra; $\phi = 0^o$; R = 12 ft; $P_{Tj}/P_{amb} = 1.185$; $U_j/a_o = 0.48$; $T_{Tj}/T_{amb} = 0.80$;

Baseline 1.6-inch Circular Nozzle Distributed Exhaust Nozzle

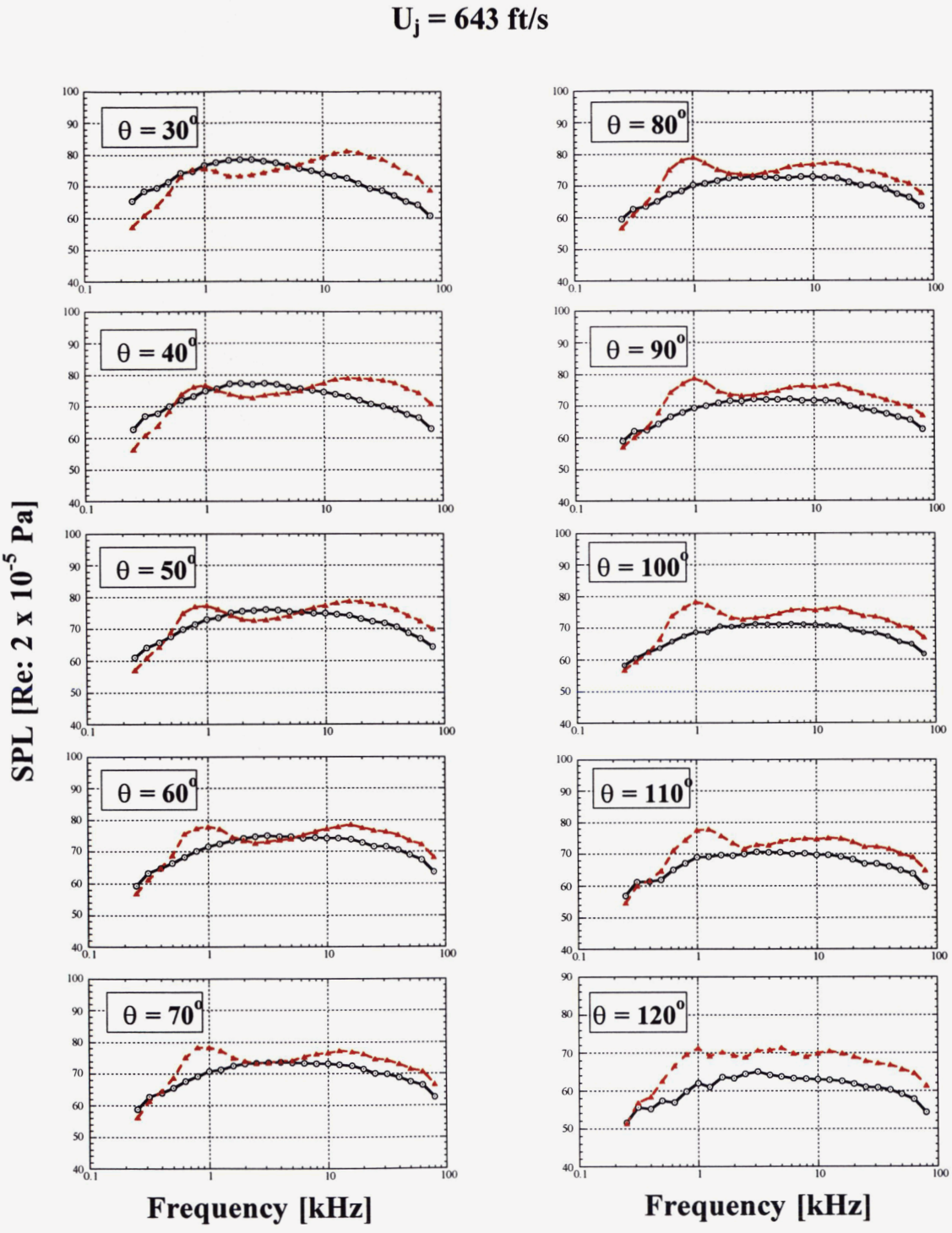

Figure C25. Comparison of $^1/_3$-octave band farfield spectra; $\phi = 0^o$; R = 12 ft;

$P_{Tj}/P_{amb} = 1.276$; $U_j/a_o = 0.58$; $T_{Tj}/T_{amb} = 0.80$;

⊙ Baseline 1.6-inch Circular Nozzle ▲ Distributed Exhaust Nozzle

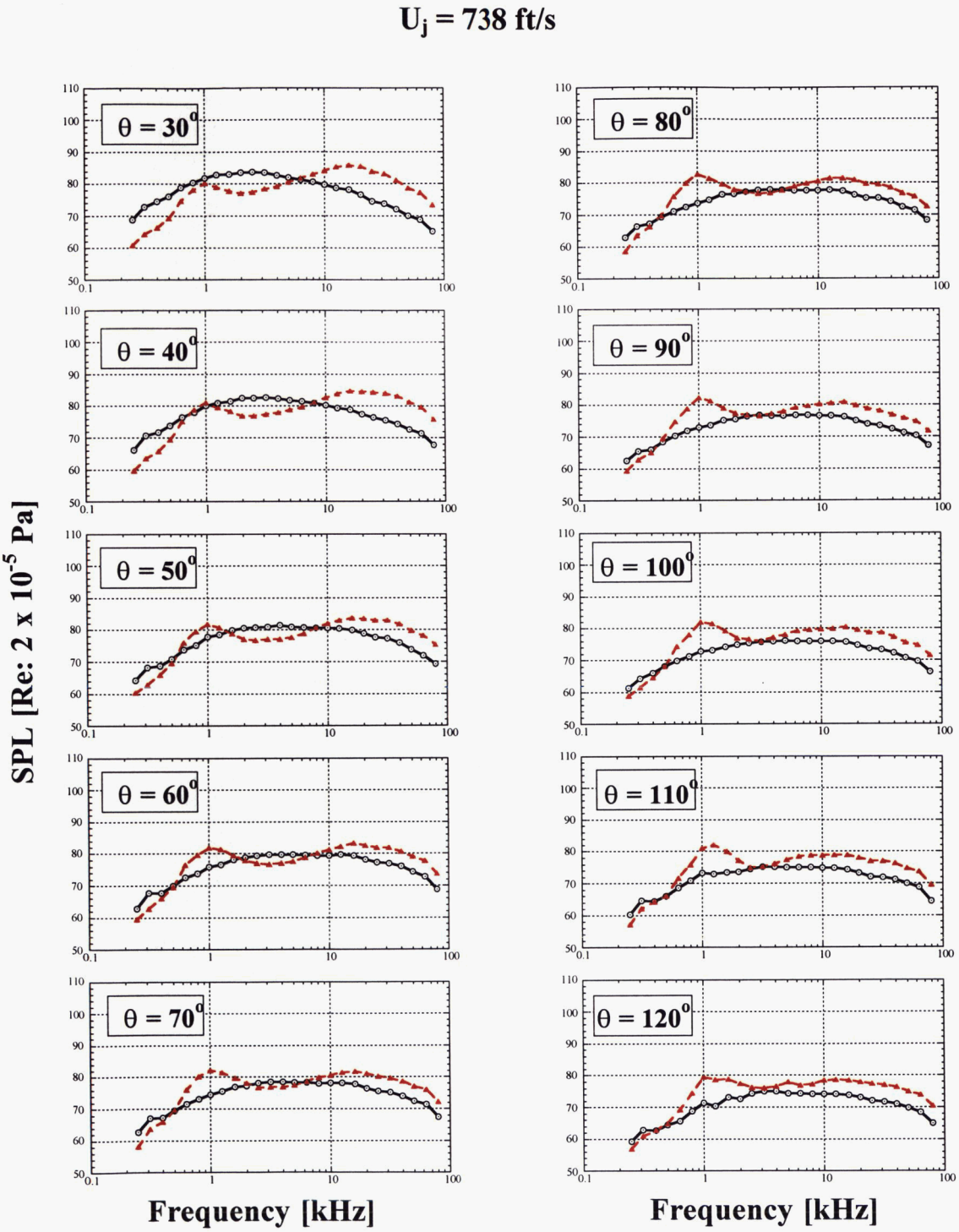

Figure C26. Comparison of $^1/_3$-octave band farfield spectra; $\phi = 30^o$; R = 12 ft;

$P_{Tj}/P_{amb} = 1.387$; $U_j/a_o = 0.66$; $T_{Tj}/T_{amb} = 0.80$;

Baseline 1.6-inch Circular Nozzle Distributed Exhaust Nozzle

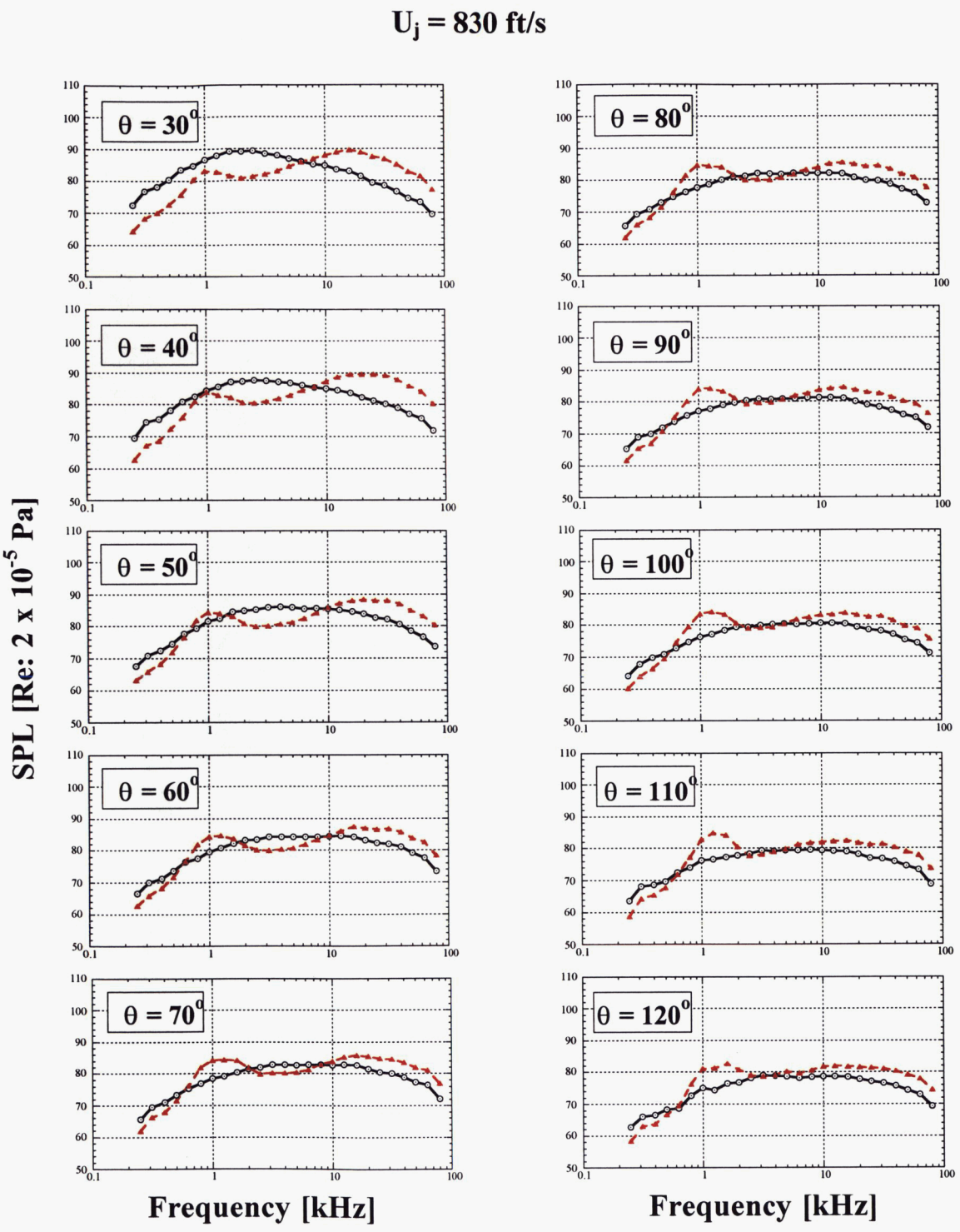

Figure C27. Comparison of $^1/_3$-octave band farfield spectra; $\phi = 0^o$; R = 12 ft; $P_{Tj}/P_{amb} = 1.524$; $U_j/a_o = 0.75$; $T_{Tj}/T_{amb} = 0.80$;

⊙ Baseline 1.6-inch Circular Nozzle ▲ Distributed Exhaust Nozzle

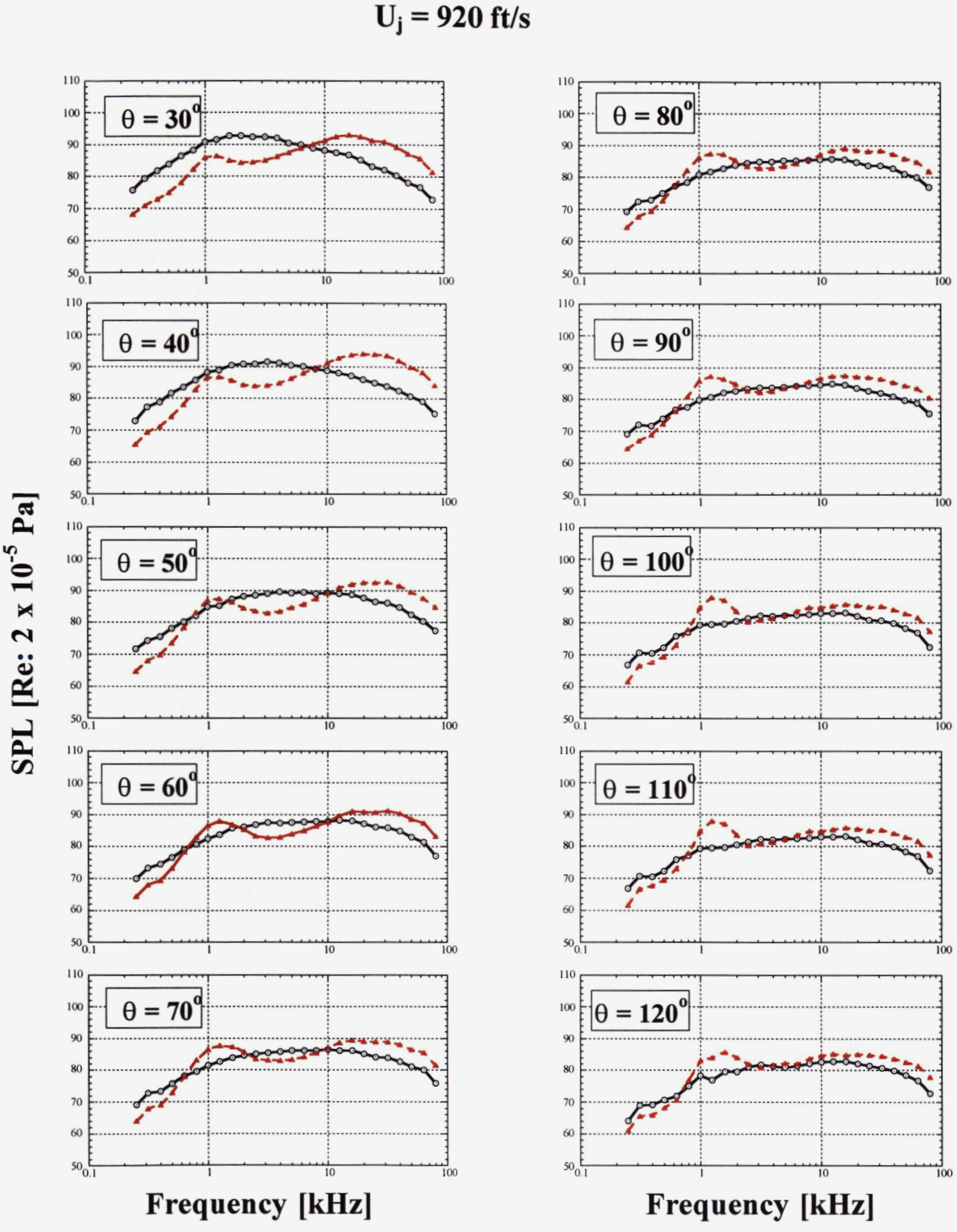

Figure C28. Comparison of $^1/_3$-octave band farfield spectra; $\phi = 0^o$; R = 12 ft;

$P_{Tj}/P_{amb} = 1.695$; $U_j/a_o = 0.83$; $T_{Tj}/T_{amb} = 0.80$;

⊙ Baseline 1.6-inch Circular Nozzle ▲ Distributed Exhaust Nozzle

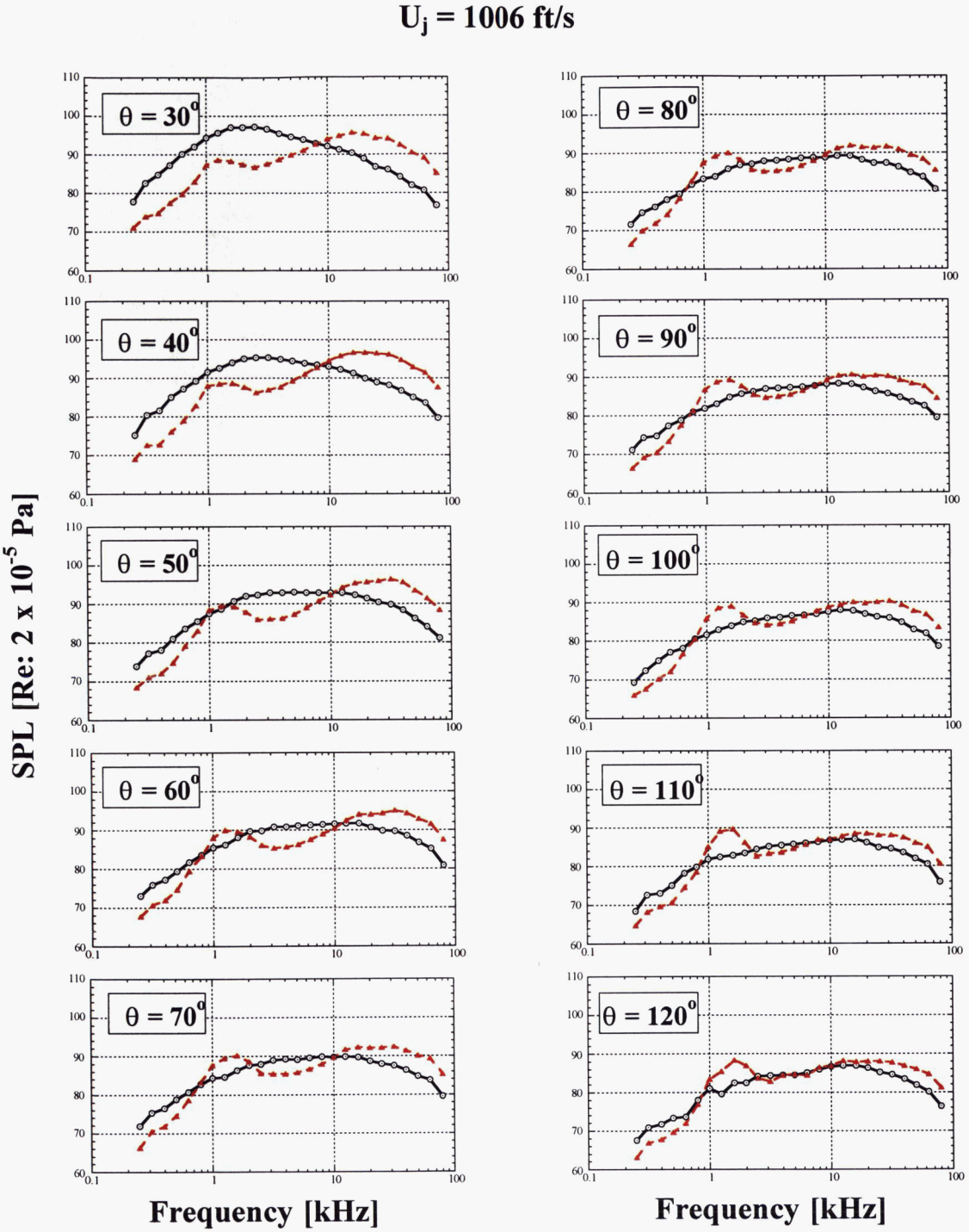

Figure C29. Comparison of $^1/_3$-octave band farfield spectra; $\phi = 0^o$; R = 12 ft;

$P_{Tj}/P_{amb} = 1.894$; $U_j/a_o = 0.90$; $T_{Tj}/T_{amb} = 0.80$;

⊙ Baseline 1.6-inch Circular Nozzle ▲ Distributed Exhaust Nozzle

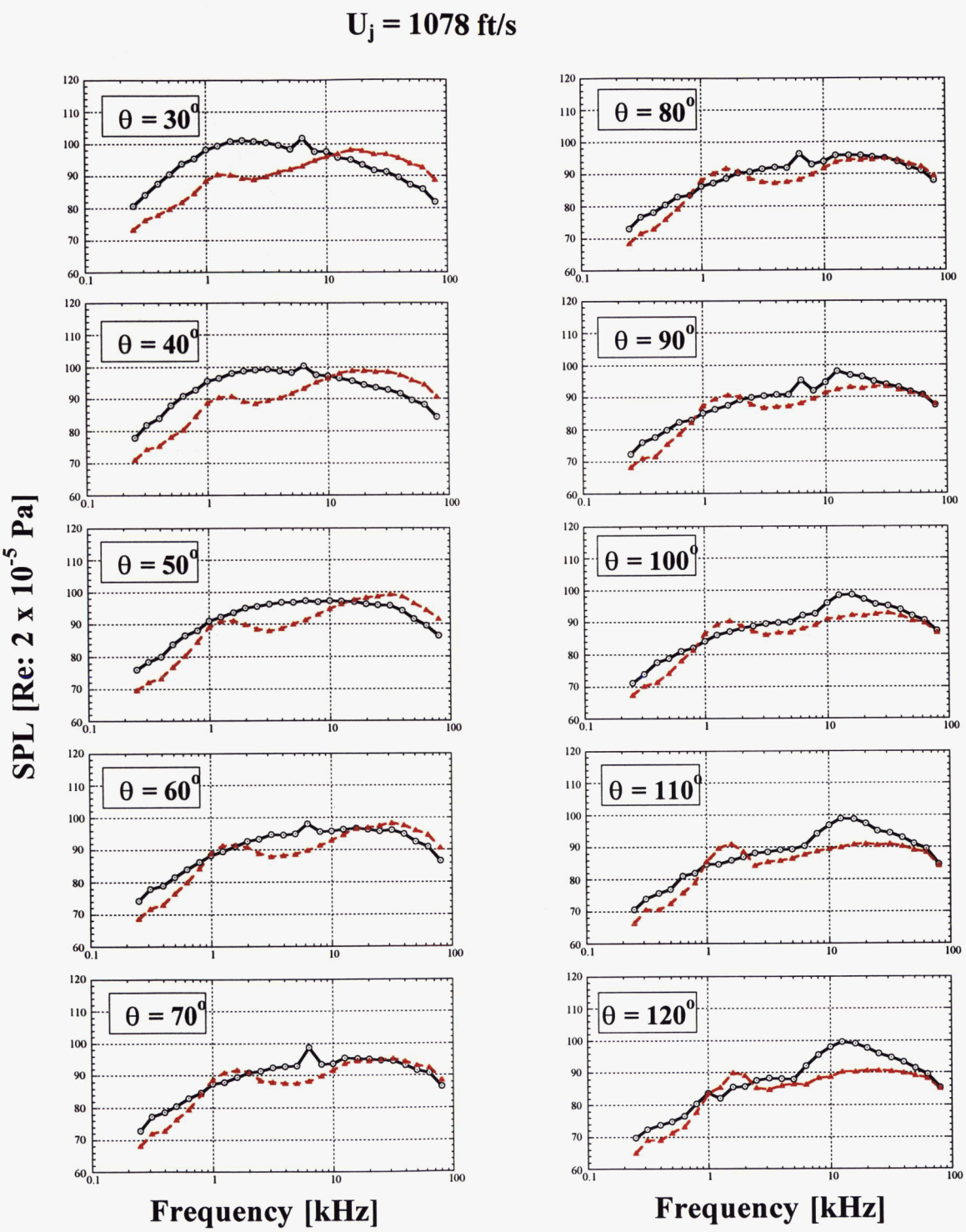

Figure C30. Comparison of $^1/_3$-octave band farfield spectra; $\phi = 0^o$; R = 12 ft;

$P_{Tj}/P_{amb} = 2.104$; $U_j/a_o = 0.97$; $T_{Tj}/T_{amb} = 0.80$;

⊙ Baseline 1.6-inch Circular Nozzle ▲ Distributed Exhaust Nozzle

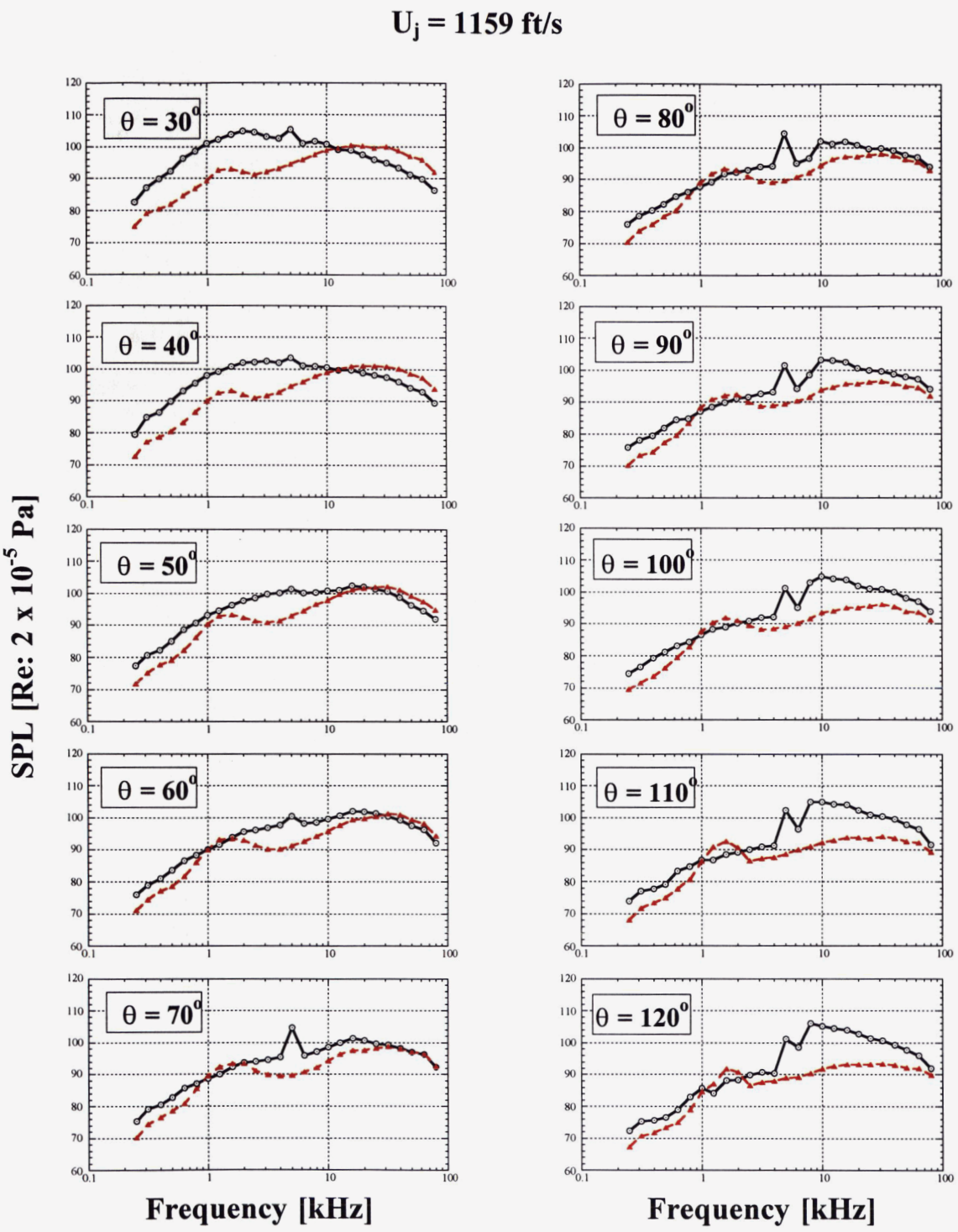

Figure C31. Comparison of $^1/_3$-octave band farfield spectra; $\phi = 0^o$; R = 12 ft;

$P_{Tj}/P_{amb} = 2.395$; $U_j/a_o = 1.04$; $T_{Tj}/T_{amb} = 0.80$;

⊙ Baseline 1.6-inch Circular Nozzle ▲ Distributed Exhaust Nozzle

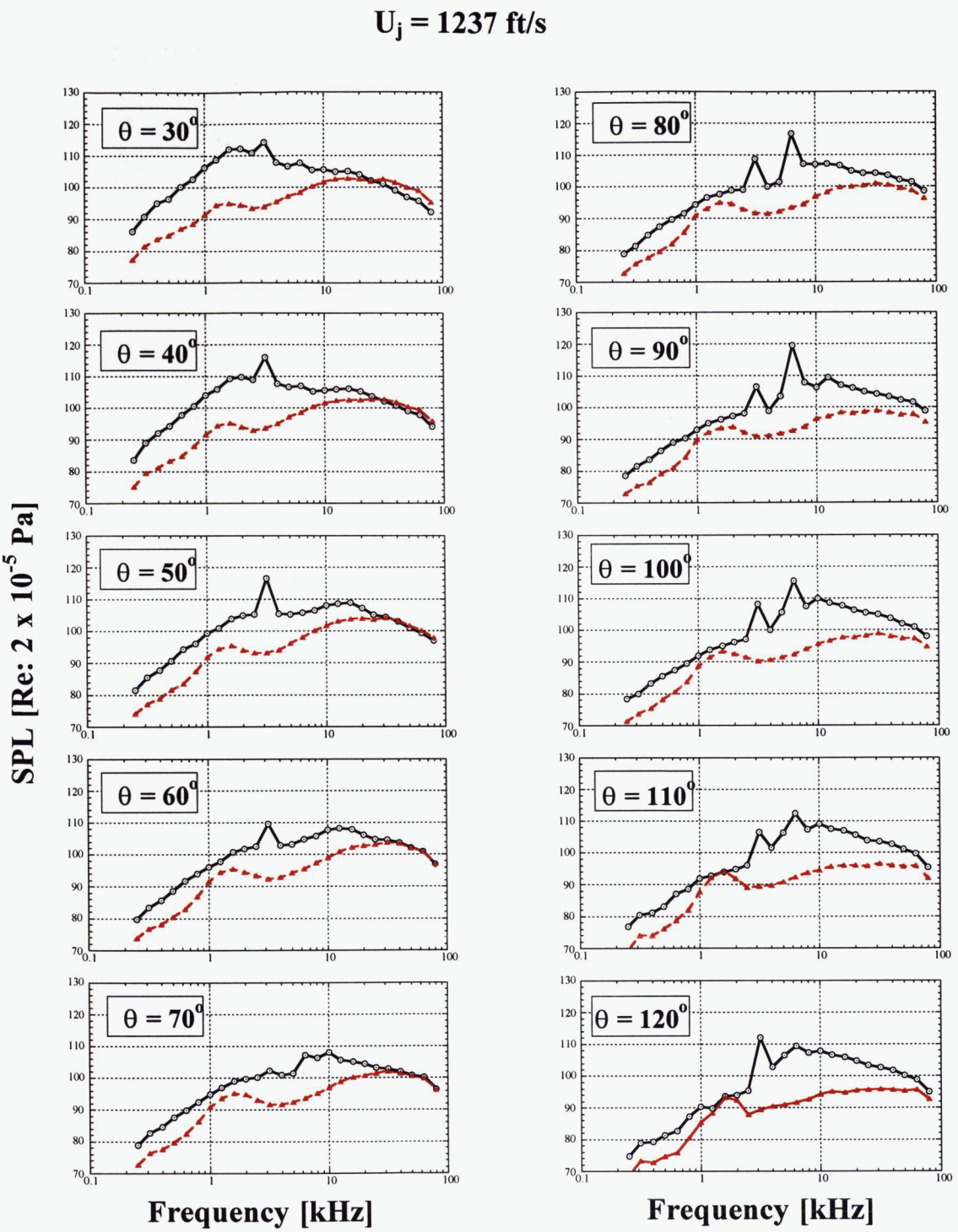

Figure C32. Comparison of $^1/_3$-octave band farfield spectra; $\phi = 0^o$; R = 12 ft;

$P_{Tj}/P_{amb} = 2.756$; $U_j/a_o = 1.11$; $T_{Tj}/T_{amb} = 0.80$;

⊙ Baseline 1.6-inch Circular Nozzle ▲ Distributed Exhaust Nozzle

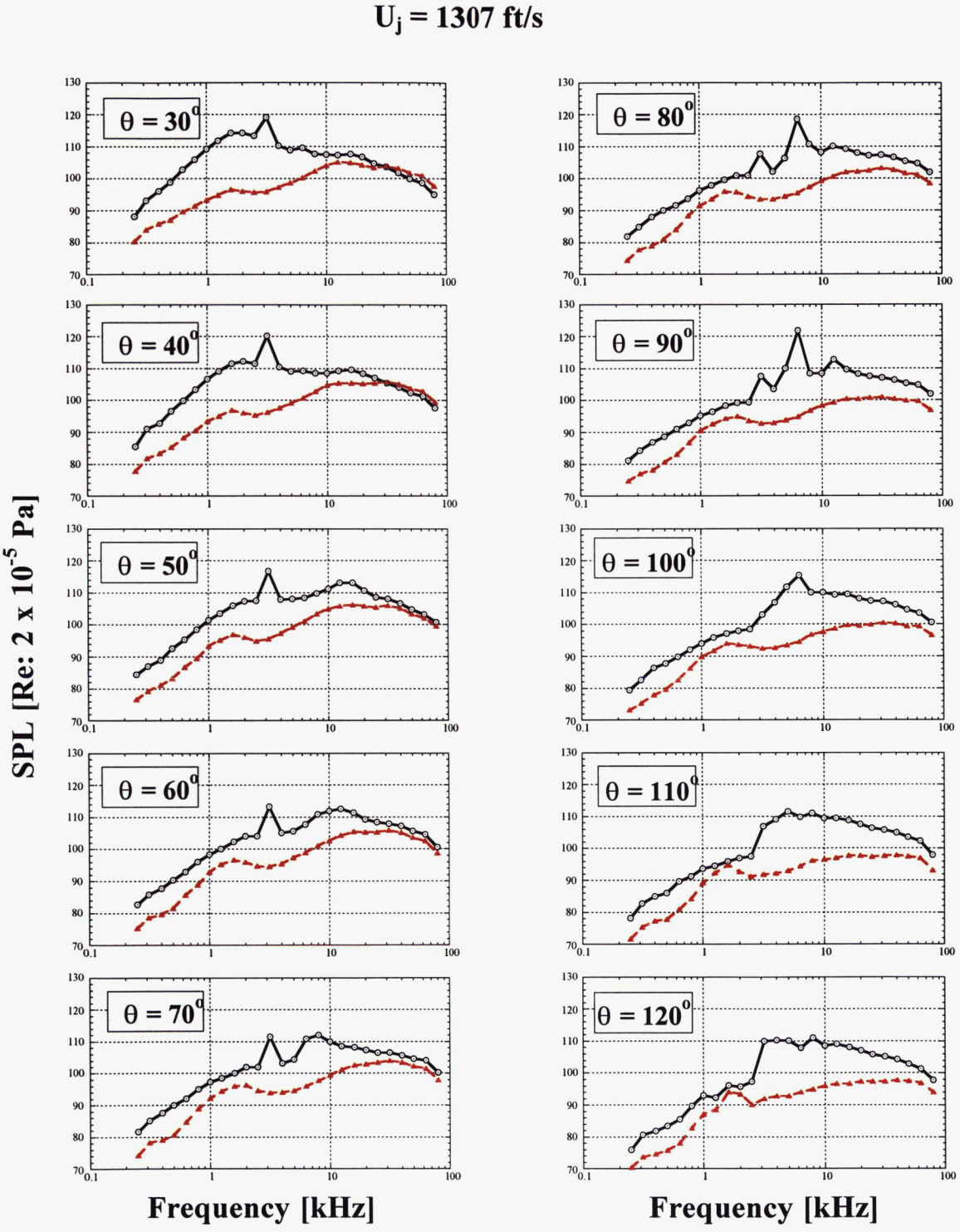

Figure C33. Comparison of $^1/_3$-octave band farfield spectra; $\phi = 0^o$; R = 12 ft;

$P_{Tj}/P_{amb} = 3.178$; $U_j/a_o = 1.17$; $T_{Tj}/T_{amb} = 0.80$;

⊙ Baseline 1.6-inch Circular Nozzle ▲ Distributed Exhaust Nozzle